Modulating Optical and Photocatalytic Properties of Transparent Metal Oxide Nanostructures *via* Defect Engineering

by

Vahid Ghodsi

A thesis

presented to the University of Waterloo

in fulfillment of the

thesis requirement for the degree of

Doctor of Philosophy

in

Chemistry (Nanoscience)

Waterloo, Ontario, Canada, 2018

Examining Committee Membership

The following served on the Examining Committee for this thesis. The decision of the Examining Committee is by majority vote.

External Examiner	NAME: Kalaichelvi Saravanamuttu Title: Associate Professor
Supervisor	NAME: Pavle Radovanovic Title: Professor
Internal Member	NAME: Eric Prouzet Title: Associate Professor
Internal Member	NAME: Germán Sciaini Title: Associate Professor
Internal-external Member	NAME: Hany Aziz Title: Professor

AUTHOR'S DECLARATION

I hereby declare that I am the sole author of this thesis. This is a true copy of the thesis, including any required final revisions, as accepted by my examiners.

I understand that my thesis may be made electronically available to the public.

Abstract

The chemistry of nanostructure has increasingly drawn attention as a compelling branch of semiconductor research. Billions of dollars are annually spent to intentionally incorporate dopants into nanomaterials to enhance their functional properties for specific technological applications. Understanding the role of native defects and their interaction with the extrinsic defects are the key to controlling the behavior of the nanoscale substance.

Deliberate incorporation of impurities into wide band gap metal oxides and their structural transformation provide numerous opportunities to manipulate their optical and electrical properties. The first part of this thesis explores the effect of europium dopant on optical and phase transformation in In_2O_3. The coexistence of multiple luminescent centers (Eu^{2+} and Eu^{3+}) in corundum and bixbyite-type colloidal In_2O_3 nanocrystals, achieved by adjusting the nanocrystal synthesis conditions, is demonstrated. The different electronic structure of these polymorphs enables the control of the optical and electrical properties *via* structural transformation. The luminescent impurities show dramatically different emission properties in the two nanocrystal phases since they are influenced by the interaction with native defects. Concentration of oxygen vacancies in In_2O_3 nanocrystals are controlled by europium dopant oxidation state and concentration, and the nanocrystal size and structure.

The hydrothermal synthesis of ternary gallium tin oxide nanocrystals throughout the full composition range is illustrated in the next part. Their photoluminescence tunability through the visible region is achieved by adjusting Ga:Sn ratio. Substitutional incorporation of Ga^{3+} in SnO_2 enhances the photoluminescence intensity of SnO_2 nanocrystals by approximately three orders of magnitude, reaching photoluminescence quantum yield of > 40%. The enhanced quantum yield is attributed to the formation of donor-acceptor pairs. Band gap widening and stronger Coulomb interaction between charged defect sites explain the increase in emission energy. Time-resolved and steady-state photoluminescence spectroscopies reveal that the nature of the dopant ion controls the interaction of extrinsic and native defects. Nanocrystals with optimized scotopic to photopic ratio and high quantum yield (~ 34%) were synthesized by adjusting various reaction conditions. This demonstrates the potential of these nanoparticles as light sources for general lighting applications.

Heterogeneous photocatalysis has emerged as an efficient and sustainable method for wastewater treatment and other environmental remediation, and forms the basis for water splitting and solar-to-

fuel conversion. Nanocrystalline metal oxides are of particular interest due to their efficiency, stability, and benign nature. The influence of the crystal structure and defects on the photocatalytic activity of these polymorphic materials remains unclear. The third part of the thesis investigates the impact of structure on the photocatalytic activity of Ga_2O_3 nanocrystals. High photocatalytic activity of metastable cubic-phase γ-Ga_2O_3 significantly reduces upon thermally-induced transformation to monoclinic β-Ga_2O_3. Steady-state and time-resolved photoluminescence measurements reveal that the reduction in photocatalytic activity upon annealing originates from a decrease in oxygen vacancy concentration. Long-lived excited states in γ-Ga_2O_3 nanocrystals leads to a decreased rate of charge recombination and hence, enhanced interfacial charge transfer. The role of $OH^{\bullet}$ and $O_2^{\bullet -}$ in photocatalytic degradation of organic dyes by Ga_2O_3 is revealed by using various scavengers. The results of this work illustrate how manipulation of the location and electronic structure of defect sites in nanostructures can effectively trap charge carriers in defect-induced states and stimulate high photocatalytic activity, without decreasing surface-to-volume ratio.

Finally, the synthesis of gallium tin oxide ternary (GTO) photocatalyst by coprecipitation method is reported and the role of dopant in altering the electronic structure of the catalysts is investigated. Higher photocatalytic performance of GTO nanocrystals for photodegradation of an organic dye was observed, compared to commercial catalyst, P25. Structural and spectroscopic analyses are performed to show that an increase in the surface area is not the sole reason for the high activity of GTO catalysts. The incorporation of Ga^{3+} in SnO_2 crystal structure widens the band gap absorption, resulting in photoactivity of conduction band electrons. The suppression of charge recombination, high surface area, and suitable band alignment for redox reactions are responsible for the high efficiency of the GTO photocatalysts. Generation of electrons, holes, hydroxyl and superoxide radicals during the degradation process is confirmed by using different scavengers.

A thorough understanding of the role of defect chemistry is required to alter the electronic structure of nanoscale transparent metal oxides for specific applications. The results of this work demonstrate how extrinsic defects can induce luminescent centers in nanocrystals, leading to the design of efficient light sources with optimized characteristics. In addition, systematic control of the concentration of intrinsic and extrinsic defects enables manipulation of charge recombination kinetics for environmental remediation purposes. This work targets a deeper understanding of the concept of rational modification of electronic structure of nanomaterials to pave the way for the architecture of diverse multifunctional materials.

Acknowledgements

First, I would like to thank my supervisor Dr. Pavle Radovanovic for his insightful comments throughout this project. His passion towards science and guidance assisted me to develop essential skills, such as time management and independent thinking, for becoming a better researcher. I also thank my advisory committee members, Dr. Eric Prouzet, Dr. Germán Sciaini, and Dr. Daniel Thomas for their time and valuable feedback on my research.

This thesis would not have been possible without the assistance of many talented and patient people. I am grateful to Dr. Jalil Assoud and Dr. Howard Siu for their time and genuine willingness to have useful discussions on several occasions during my PhD. I also acknowledge the help of Dr. Michael Collins, Dr. Carmen Andrei and Andrew Kacheff for their aid in DRS, TEM image and BET data collection. I had the opportunity to work closely with postdoctoral colleagues in the group. I am grateful to Dr. Arunasish Layek, Dr. Baran Yildirim and Dr. Joshua Byers for sharing their invaluable experience and knowledge. Their professional advice was constructive to overcome research related difficulties during the program.

I express my sincere gratitude to all of the current and past group members for their assistance and contribution in the group. The help received from Ting, Lisa, Tahereh and Vadim at the early stages of my work was extremely valuable. I have particularly had the pleasure of working with Manu, Paul, Natalie, Terry and Hanbing on a variety of projects and tasks. I am truly appreciative of their tremendous support and enthusiasm. Very special thanks goes to Natalie and Nathaniel for their help in editing some sections of the thesis. I am also thankful to our previous fourth year student, Yi, and Susi as they were highly enthusiastic in the development of the photocatalysis project during the earliest stages. The teamwork skills demonstrated by Yunyan, Enas, Shuoyuan, Yi, and Johnathan ensured things run smoothly in the lab.

I also thank my friends to make my stay at Waterloo more delightful. And last but not least, I am extremely grateful to my parents and my siblings, without whom I could not have come this far, for their wholehearted continuous support.

Table of Contents

List of Figures

List of Tables

List of Abbreviations

bcc	Body-centered cubic
CB	Conduction band
CBM	Conduction band minimum
DAP	Donor-acceptor pair
DDA	Dodecylamine
Eq.	Equation
FWHM	Full width at half maximum
GTO	Gallium tin oxide
HRTEM	High resolution transmission electron microscopy
IRF	Instrument response function
ITO	Indium tin oxide
Ln	Lanthanide
MB	Methylene blue
NC	Nanocrystal
NIR	Near infrared
NP	Nanoparticle
OA	Oleic acid
OAm	Oleylamine
PL	Photoluminescence
PLQY	Photoluminescence quantum yield
QBS	Quinine bisulfate

rh	Rhombohedral
Rh-590	Rhodamine 590
STEM	Scanning transmission electron microscopy
TCO	Transparent conducting oxide
TEM	Transmission electron microscopy
TOPO	Tri-n-octylphosphine oxide
TMO	Transparent metal oxide
UV	Ultraviolet
VB	Valence band
VBM	Valence band maximum
Vis	Visible
XRD	X-ray diffraction

Chapter 1
Introduction[1]

1.1 Transparent Metal Oxides

A vast variety of electronic and chemical properties of transparent metal oxides (TMOs) makes them scientifically compelling and technologically fascinating materials. They are chemically stable, and often show comparatively high conductivity as well as being transparent to visible light owing to a wide band gap.[1] The great diversity of binary oxides; such as SnO_2, In_2O_3, Ga_2O_3, ZnO and TiO_2 span a wide range of electrical and photonic properties and applications from sensors, catalysts to optical window coatings and solar cells.[2–6] An interesting characteristic of transparent conducting oxides (TCOs) is combining transparency in visible range and high reflectivity in infrared, resulting in their application in architectural windows which allow for visible light transmission into the buildings while reflecting heat. Polymorphic TCOs have drawn a fair amount of research interest as they exhibit structure dependent properties, motivating scientists to conduct studies on phase transformation mechanisms, to further expand their functionality.[7–10]

A high degree of control over the properties of nanomaterials is always desired to enhance their functional properties. Native crystallographic defects have been substantially investigated, giving rise to modulation of electronic structure and enhancement of intrinsic properties.[11] Doped systems play a key role in exploring new avenues by extrinsically improving specific properties of nanostructures. The intentional incorporation of impurities into the host lattice leads to alteration of the physical properties. The stabilization of an otherwise unstable host lattice crystal phase can be achieved by incorporation of a dopant.[12] In addition, the effect of doping on optical, electronic, and magnetic properties is a potential motivation for expanding the application of the TCO nanostructures.

The basis of a transparent conductor is a band gap which absorbs insignificantly over most or all the visible range. Most TCOs (thickness of 0.1-1.0 μm) demonstrate a high average transparency (≥ 80%) in the visible spectrum, originating from a band gap of 3 eV or larger, and possess high carrier

[1] This thesis has components which were previously published in the following two papers:

concentration (10^{18}- 10^{21} cm^{-3}).[13] Generally, the low formation energy of cation interstitials or oxygen vacancies leads to n-type conductivity in TCOs. The enhancement of electrical conductivity is possible by incorporation of dopants. However, some dopants, such as transition metals may lead to optical absorption in the visible spectrum. High mobility carriers must be seriously considered at the starting point of designing a good transparent conductor. Even a small number of highly mobile carriers deliver significant conductivity while minimizing the optical absorption. Conduction bands (CB) composed of s orbitals give rise to carriers with high mobility, contrary to d bands. 4s, 5s, or 6s orbitals often form the CB in oxides which introduce them as suitable TCO candidates. Given that the band gap is typically small when CB is comprised of 6s orbitals, high transparency in the visible region is not usually achievable. Both PbO_2 and Tl_2O_3 are reported to be black compounds. In contrast, Ga_2O_3 and SnO_2 which CB is made of 4s and 5s bands, respectively, exhibit good TCO behavior.[14]

On the other hand, the development of p-type TCO materials with conductivities as high as their n-type counterparts is a significant research challenge. Oxygen 2p orbitals predominantly compose the valence band (VB) of most oxides. Only limited success was achieved in producing p-type TCO due to low hole mobility in p bands. Contrary to high carrier mobilities in n-type TCOs, which occasionally exceed 50 $cm^2V^{-1}s^{-1}$, p-type mobilities higher than 5 $cm^2V^{-1}s^{-1}$ are not frequently reported.[14,15]

In_2O_3, Ga_2O_3 and SnO_2 are among the most technologically used TCOs that are specifically studied in this thesis. Their structural and optical properties are briefly discussed in the following sections.

1.2 Structural and Optical Properties of Oxides

1.2.1 Indium Oxide

Indium oxide is one of the most fascinating TCOs due to its functionality, and various applications in optoelectronic devices such as flat panel displays, sensors, and photovoltaic cells.[16,17] The interest in In_2O_3 partially originates from its high carrier mobility (10-75 $cm^2V^{-1}s^{-1}$) and high carrier density (~ 10^{19}-10^{20} cm^{-3}).[8,13,18] It has a high transparency in the visible region due to its relatively large band gap (~ 3.75 eV) and exhibits n-type conductivity, stemming from oxygen vacancies.[17,19] It crystalizes in two distinct phases, the thermodynamically stable cubic phase (*bcc*-In_2O_3; Figure 1.1a) having bixbyite crystal structure and the metastable rhombohedral phase (*rh*-In_2O_3; Figure 1.1b) having

corundum crystal structure. The phase transformation mechanism and the structural relations of the two polymorphs have been extensively studied, leading to deeper understanding and development of functional properties.[7,8,19]

The cubic bixbyite In_2O_3 crystal structure can be obtained from the fluorite structure by eliminating a quarter of the anions as well as slightly offsetting the remaining anion sites. Consequently, there are two discrete sites for In^{3+} in *bcc*-In_2O_3, known as b- and d-sites. A quarter of In^{3+} cations are located in b-sites, adopting C_{3i} (or S_6) point group symmetry (trigonally compressed octahedral coordination). Three quarters of In^{3+} nest in highly distorted octahedral d-sites. In contrast, oxygen ions compose hexagonal close packed structure in the metastable *rh*-In_2O_3, while the cations fill up two-thirds of the six-coordinate C_2 sites.[12,16]

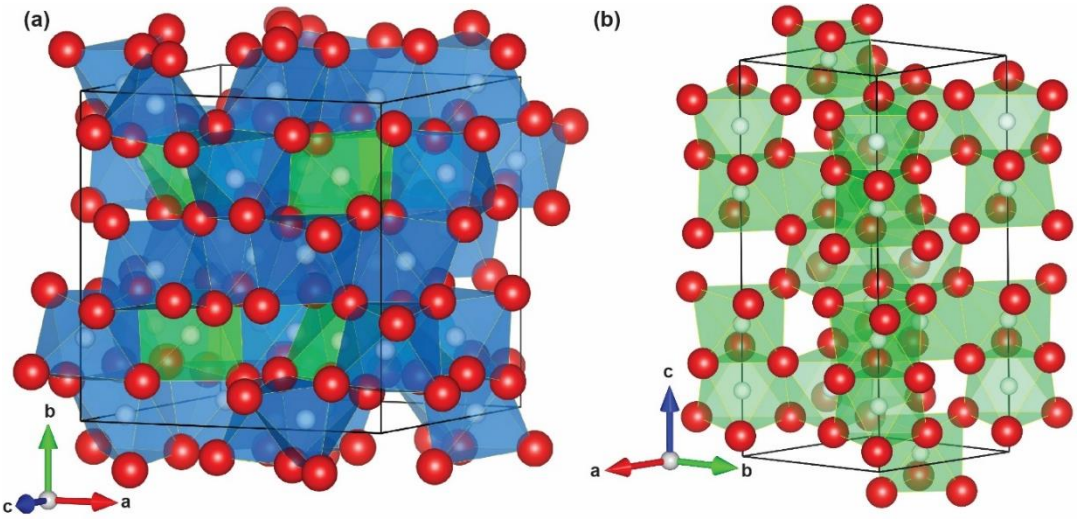

Figure 1.1. Crystal structure of (a) stable cubic In_2O_3 and (b) metastable rhombohedral In_2O_3. The white and red spheres indicate In^{3+} and O^{2-} ions, respectively. The green and blue octahedra illustrate b-site and d-site in *bcc*-In_2O_3, respectively.

Since the synthesis of metastable *rh*-In_2O_3 from bixbyite phase by employing high temperature (1250 ˚C) and high pressure (6.5 GPa) by Shannon in 1966,[20] many other synthetic methods have been established to stabilize the corundum crystal structure under ambient pressure and relatively lower temperatures.[21–23] Knowing that nanocrystal (NC) size is inversely proportional to surface stress, stabilizing a high energy phase below a critical size is achievable. The large surface to volume ratio in nanomaterials results in high surface energy and surface stress, leading to stabilization of metastable phases below the critical size. More recently, a comprehensive study on the mechanisms

and kinetics of phase transformation of colloidal indium oxide revealed the correlation between the size and structure of NCs, resulting in stabilization of small size *rh*-In_2O_3 NCs (≤ 5 nm).[7,8,12,19] The significance of control over crystal structures to broaden the functionality of materials is evident. As an example, the stronger emission in *rh*-In_2O_3, relative to *bcc*-In_2O_3, was attributed to higher density of defects in metastable *rh*-In_2O_3 NCs.[8,24,25]

Developing the proficiency in controlling, inducing and manipulating defect structure in TCOs is of paramount importance since it leads to expanding their photonic properties. In_2O_3 is a suitable model system due to the existence of its polymorphic structure and presence of two distinct sites in *bcc*-In_2O_3 (b- and d-sites). Doping In_2O_3 NCs provides an opportunity to make a direct comparison between *rh*-In_2O_3 and *bcc*-In_2O_3 NCs to understand the impact of dopants on the optical properties of In_2O_3 NCs. Such a correlation is crucial for rational preparation of TCOs with the desired size, structure, and composition, leading to manipulation of the structure-function relationship. Indium tin oxide (ITO) is the most extensively studied TCO owing to a broad range of applications in solar cells, flat-panel displays, and gas sensors. Simultaneous synthesis of *rh*-ITO and *bcc*-ITO NCs in one reaction vessel illustrated a striking difference in their optical properties. *bcc*-ITO showed a strong absorption in the near-infrared (NIR) region owing to resonant plasmon oscillation, arising from high concentration of free carriers in the CB. In contrast, *rh*-ITO did not absorb NIR light. This distinct behavior was attributed to the dissimilar electronic structure of the donor, Sn^{4+}, having appreciably higher donor activation energy in *rh*-ITO relative to *bcc*-ITO.[16] This serves as a classic example of how a minor adjustment in NCs size and phase impart a remarkably different electronic structure and optical properties in NCs.

1.2.2 Tin (IV) Oxide

Another TMO that has found various applications ranging from catalysis and sensing to solar cells and, more recently, lithium ion batteries is tin(IV) oxide, also known as stannic oxide.[26–29] The less known orthorhombic phase of SnO_2, appears at elevated temperature (800 ^oC) and pressure higher than 158 kbar, and is slightly more dense relative to tetragonal phase.[30] Rutile SnO_2 (Figure 1.2) is an oxygen-deficient n-type semiconductor, with a tetragonal unit cell, and the band gap of 3.6 eV. The unit cell accommodates 6 ions, including 4 anions and 2 cations. The MO_6 octahedra is tetragonally distorted, adapting D_{4h} point symmetry, while oxygen ions are threefold coordinated.[31,32]

The presence of oxygen vacancies is the origin of its high conductivity and orange emission.[33] Majority of the studies on this material have centered around its remarkably high carrier concentration (10^{20} cm^{-3}), while photoluminescence (PL) properties remain underexplored compared to other oxides. The emission of SnO_2 nanostructures originates from the recombination of electrons trapped in shallow donor states formed by oxygen vacancies with native surface states within the band gap.[34,35] The depth of the donor and surface states were estimated to be about 0.03-0.15 eV below the conduction band minimum (CBM) and 0.9 eV above the valence band maximum, respectively.[34,36,37] Despite having a direct band gap, the band-to-band transition in SnO_2 is dipole-forbidden which hampers its functionality in optoelectronic devices. Nevertheless, doping tin oxide nanostructures could lead to breaking of the selection rule and recovering its optical activity.[35,38]

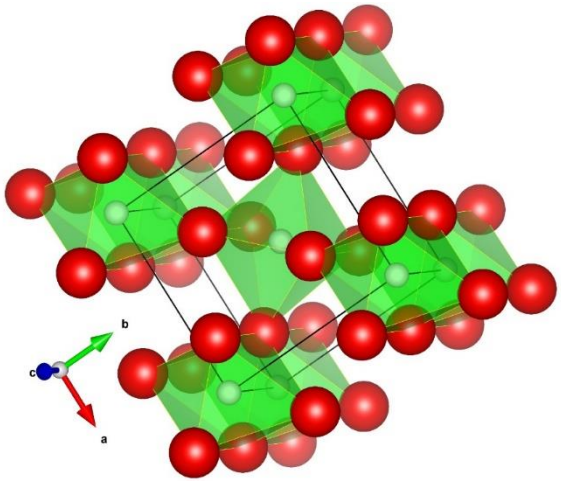

Figure 1.2. Crystal structure of rutile SnO_2. Sn^{4+} and O^{2-} ions are demonstrated by white and red spheres, respectively.

1.2.3 Gallium Oxide

Ga_2O_3 has the widest band gap among TCOs (4.9 eV), which crystallizes in five different polymorphs (α, β, γ, δ, and ε phases) and shows n-type conductivity. The unique properties make Ga_2O_3 suitable for a variety of applications including, but not limited to, photocatalysts,[39–41] phosphors,[4,42,43] photodetectors,[5] and spintronics.[44] The structural and photonic properties of β -Ga_2O_3 (monoclinic phase) have been investigated more than any other phase, as it is the most thermodynamically stable phase. There are two and three nonequivalent sites in which cations and anions reside, respectively (Figure 1.3a). Half of Ga^{3+} cations adopt distorted tetrahedral symmetry,

while the other half is located in highly distorted octahedral sites. On the other hand, two third of anions are threefold coordinated and one third reside in tetrahedral sites.[45,46] However, in colloidal NC form, Ga_2O_3 can be stabilized in a metastable state, and adopts cubic structure (γ-phase).[11] Owing to complexity, much less is known about γ -Ga_2O_3 crystal structure. The cubic phase has a defective spinel structure, with two Ga^{3+} vacancies per each 18 gallium sites (Figure 1.3b). Analogous to the monoclinic phase, γ-Ga_2O_3 is also composed of cationic tetrahedral and octahedral sites. However, the ratio of those sites varies, depending on preparation method and size of particles.[47] Generally, an increase in tetrahedral relative to octahedral ratio was reported with decreasing crystallite size.[48,49] A consensus was recently reached that approximately 35 % of cations are tetrahedrally coordinated in nanocrystalline materials.[48] Both β-Ga_2O_3 and γ-Ga_2O_3 exhibit important functional properties arising from the presence of native defects. Ga_2O_3 therefore represents an excellent model system for investigation of the influence of the crystal structure and defects on the optical and photocatalytic activity.

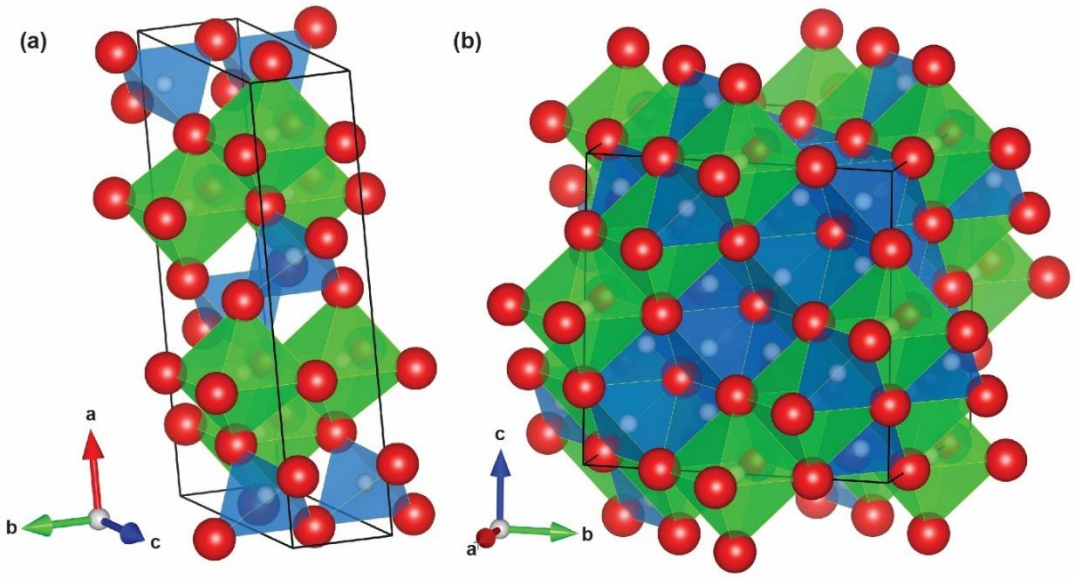

Figure 1.3. Crystal structure of (a) monoclinic Ga_2O_3 and (b) cubic Ga_2O_3. Ga^{3+} and O^{2-} ions are indicated by white and red spheres, respectively. The green and blue polyhedra illustrate six and four coordinated Ga^{3+} sites, respectively.

Optoelectronic properties of monoclinic gallium oxide (β phase) have been most extensively studied.[50–52] The UV and blue emission in β -Ga_2O_3 originate from recombination of self-trapped

excitons and a tunnel recombination of an electron on a donor with a hole on an acceptor, respectively. Oxygen vacancies ($V_O^{\bullet}$), which are readily formed in Ga_2O_3, act as electron donors, while a complex consisting of gallium-oxygen vacancy pair ($(V_O, V_{Ga})^{\prime}$) likely gives rise to the acceptor state. Figure 1.4 depicts the processes resulting in UV and visible emission of β -Ga_2O_3. Upon exciton formation after UV light absorption (process 1), the CB electron is trapped in the donor state (process 2), while the hole in the VB is trapped in the acceptor state (process 3), forming a donor-acceptor pair (DAP), according to the following equations.

$$(V_O, V_{Ga})^{\prime} + V_O^{\bullet} \overset{h\nu}{\rightarrow} (V_O, V_{Ga})^{x} + V_O^{x} \tag{1.1}$$

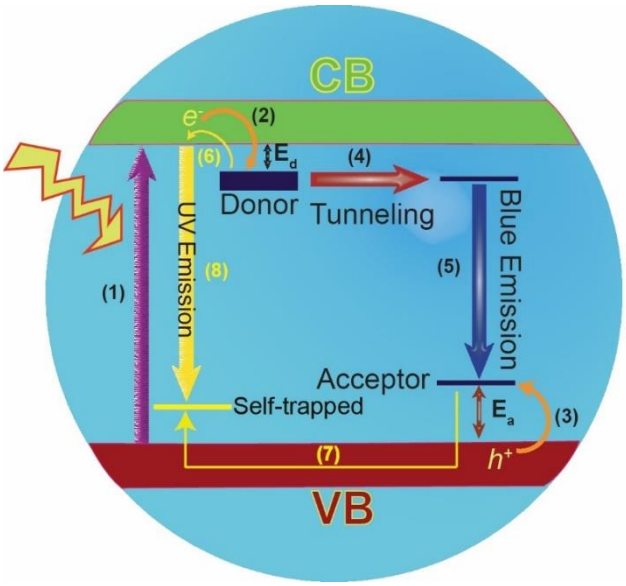

Figure 1.4. Schematic representation of Ga_2O_3 emission in the UV and visible range of the spectrum. Initially, electron and hole are trapped on donor and acceptor sites, respectively. Next, electron migrate to an acceptor site by tunneling and generate localized exciton, followed by radiative recombination at the acceptor site, raising to blue emission. UV emission is enabled by recombination of detrapped electrons in CB with self-trapped holes.

The trapped electron migrates to an acceptor site through tunnel transfer (process 4), which is the rate determining step, to form a trapped exciton. Blue emission stems from radiative recombination of electrons and holes on an acceptor site (process 5, reverse of Eq. 1.1). High energy emission in the UV (process 8) is generated by electron and hole detrapping (process 6 and 7) and the recombination of the charge carriers in the CB and VB, respectively. The activation energies of the detrapping states,

corresponding to activation energies of defects was determined by low temperature PL.[51] The donor and acceptor ionization energies were estimated to be ~ 0.04 eV and ~ 0.42 eV, located below the CB and above the VB, respectively. A notable feature of Ga_2O_3 PL is the large Stokes shift, originating from a strong electron–phonon coupling, which is an indication of strong localization of the charge carriers. While the UV emission decays on the nanosecond scale (~ 30 ns), the low energy emission exhibits, at least, a three order of magnitude longer lifetime.[53] The contribution of a strong phonon coupling and a wide distribution of donor and acceptor states leads to the broadness of blue PL band in Ga_2O_3.

1.3 Donor-Acceptor Pair Model

Because the optical properties of oxides investigated in this thesis are explained by DAP mechanism, it is worth discussing the underlying mechanism in terms of energy and its impact on the lifetime of the photoexcited carriers. The PL properties arise from the electron-hole recombination upon transfer of the electron from the donor to the acceptor site (tunnel transfer).[51,54] This DAP mechanism is a hallmark of Ga_2O_3, and the resulting PL can be manipulated by defect interactions. The ionized nature of donors and acceptors results in Coulomb interaction between them, which influence the energy of DAP emission, as illustrated by the following equation.

$$E_{em.} = E_g - (E_D + E_A) + \frac{e^2}{4\pi\varepsilon r} \pm nE_{phonon} \tag{1.2}$$

where E_g is band gap energy, E_D and E_A are donor and acceptor binding (ionization) energies, respectively, r is the average donor-acceptor separation, ε is the absolute permittivity of material (dielectric constant), E_{phonon} is the energy of phonons involved in the radiative transition and the third term on the right, $E_c = e^2/4\pi\varepsilon r$, is the Coulomb term. The closer proximity of DAPs (smaller r) leads to an increase in Coulomb interaction between them and consequently, a blue-shift in emission energy. Defect density, as a result, is a degree of freedom which can be utilized to tune the PL emission in the visible range to enhance the applicability of these nanomaterials. The other outcome which can be inferred from the DAP model is the impact of excitation power on emission energy. Greater excitation power is anticipated to generate more active donor and acceptor pairs, resulting in a rise in E_c and eventually tailing of DAP emission towards blue.

Several measures can be taken to modulate the emission of nanoparticles (NPs) whose PL is governed by DAP mechanisms. Our research group has recently showed that γ-Ga_2O_3 can also be

stabilized in the nanocrystalline form through the colloidal synthesis, and its optical properties can be altered by tuning the size and composition of the NCs.[11] The relationship between concentration of defects and lifetime of excited carrier is another valuable conclusion withdrawn from the DAP model. High energy emission is expected to decay faster, compared to the low energy side of DAP emission. Shorter separation between defects, which causes the phosphor to emit at higher energy, also translates into higher probability of charge recombination. Reduced donor-acceptor separation is achievable by synthesizing small NCs either at lower temperature or shorter reaction duration. Reducing environment, intensifies the PL emission remarkably, while oxidizing environment leads to a pronounced decrease in the PL intensity, both of which indicate the influence of the control over internal structural defects to chemically manipulate the optical properties of NCs.[55] Subsequently, they illustrated that luminescent dopants or conjugated molecular adsorbates can interact with native defects *via* energy transfer, and could be utilized to exploit the PL properties of these NCs of generate white light emission.[1,42,56,57]

1.4 Modulating TCOs Properties by Doping

Doping and alloying have proven to be efficient methods for altering the electronic structure of semiconductor NCs, thereby introducing new magnetic, optical, and electrical properties.[1,16,26,58–63] Through generating new energy states within the band gap of NPs, introduction of extrinsic defects in nanoparticles can tailor their electronic structure and manipulate their optoelectronic properties. Furthermore, the impact of dopants on native defects illuminate light on their interactions with dopant centers and their influence on sensitization of dopant emissions. The presence of such defects in polymorphic oxides leads to enrichment of optical properties of TCOs, which is a motivation for their investigation.

1.4.1 Doping at Nanoscale: Challenges and Mechanism

Effective doping- substitution of the host atoms in the NC core by the dopant instead of adsorption on the NC surface- would lead to the enhancement of NC inherent properties. However, this was regarded as a formidable task and the feasibility of the NC doping was achieved more recently. A primary explanation was the reduced ejection distance to the surface of NCs to expel impurities, compared to bulk materials.[64] Self-purification is also a barrier to achieve doping content close to the nominal doping concentration. This allegedly intrinsic mechanism explains that NCs are hard to dope because impurities solubility in reduced dimensional materials is lower than their bulk

counterparts.[65,66] The host lattice, which is in thermodynamic equilibrium with the synthetic medium, anneals out the dopants during growth due to a higher formation energy of defects in NCs relative to the bulk.[66,67] Growth of a macroscopic semiconductor crystal at elevated temperatures allows for a facile diffusion of dopants in the host, yielding a high doping concentration. However, typical solution-phase syntheses of semiconductor nanomaterials are performed at relatively low temperatures (< 400 °C).[68] Thermal equilibrium, and accordingly facile diffusion of dopants, is not established under this condition. Diffusion of Mn in II-VI semiconductor was determined to be only 1-3 Å at 300 °C, implying that thermal equilibrium is not an appropriate starting point for explaining doping in nanostructures.[68] This also indicates that kinetic factors govern NC growth and control the dopant incorporation in the host lattice.[67,68] The dopant must initially bind to the surface of the NC and subsequently be encapsulated by host overgrowth. When the dopant atoms can bind to the host surface for a long enough time that is analogous to the reciprocal growth rate, they are "trapped" during growth. The main factors that regulate adsorption and hence, doping efficiency are surfactants, nanocrystal shape, and surface morphology.[68] The residence time of an impurity on a facet is controlled by its binding energy. As an example, the doping efficiency of Mn in II-VI semiconductor improves due to its strong binding energy on (001) facet of zinc-blend crystal structure.[68]

Choosing appropriate coordinating ligands plays a crucial role in optimizing the reactivity of host and dopant. The relative Lewis acidity of the precursors has both thermodynamic and kinetic implications. It influences both the ease of breaking metal-ligand bonds (thermodynamic stability) and the precipitation reaction rate (kinetic reactivity). When dopant and host cations possess identical coordinating ligands, their relative Lewis acidity may dictate the doping efficiency. For instance, a harder Lewis acidity of a dopant cation, relative to the host cation, leads to poor dopant incorporation. An approach to overcome an ineffective doping is to separate NC nucleation and growth step from doping process. For this to occur, the precursor reactivities are optimized for the dopant nucleation to take place first. Coating the nuclei with a shell of the host substance produces a core/shell structure.[69]

Attractive characteristics of lanthanides, such as sharp f-f transitions and sensitization by the host lattice, is a motivation to study the optical properties of Eu: In_2O_3 (Chapter 3). In addition, optical and photocatalytic activities of alloyed gallium tin oxide are explored in Chapters 4 and 6. The main features of lanthanides and heterovalent doping are discussed in the following subsections.

1.4.2 Lanthanides

The active area of research on lanthanides (Ln) is triggered by the demand for radiant materials to satisfy the need of bioimaging, telecommunication, lighting and sensors.[70,71] The continuous filling of shielded 4f orbitals and numerous energy states are characteristics of lanthanides. The energy of these states is regulated by electrostatic repulsion between them, ligand field splitting and spin-orbit coupling. As 4f orbitals are shielded by the filled 5s and 5p outer shells, they are insensitive to the chemical environment, giving rise to very sharp 4f-4f transitions. However, the probability of such transitions is governed by spectroscopic selection rules and due to the similar parity of ground and excited states, they are forbidden (Laporte selection rule). Consequently, 4f-4f transitions possess very low absorption coefficients and the radiative decay of their excited states often lasts for milliseconds.[72,73]

The forbidden character obstructs the use of these luminescent materials in optoelectronic devices. Nonetheless, there has been considerable effort to exploit unique properties of lanthanides, such as resistance to photobleaching, upconversion photoluminescence and PL band covering the entire visible and NIR spectral region.[2,74–78] The small molar absorptivity of lanthanide ion f-f transitions can be overcome by sensitization of the lanthanide dopants by host materials (matrix). The host lattice must be chemically and photophysically stable as well as presenting low lattice phonon energy to reduce nonradiative recombination processes. Yet, the most widely- studied systems are alkaline earth fluorides, although oxides are an interesting alternative.[79,80]

Eu^{3+}, as a luminescent structural probe, is of particular interest among lanthanides because it supplies information such as number of metal ion sites, site symmetry, donor-acceptor distance and solution state of the lanthanide ion.[71] Among Eu^{3+} f-f transitions, ${}^5D_0 \rightarrow {}^7F_{2,3,4}$ emissions are electric dipole allowed transitions and therefore, sensitive to chemical environment of Eu^{3+} ion, while ${}^5D_0 \rightarrow {}^7F_1$, as a magnetically allowed transition is not impacted by the surroundings. As corollary, the integrated intensity ratio of ${}^5D_0 \rightarrow {}^7F_2$ to ${}^5D_0 \rightarrow {}^7F_1$, established as *R* value, contains information about Eu^{3+} doping site and the extent of disorder around the ion. It was illustrated that Eu^{3+} incorporation in non-centrosymmetric sites, such as surface sites, suppresses the ${}^5D_0 \rightarrow {}^7F_2$ transition while it gains intensity upon internal incorporation.[56,81] Another informative transition is ${}^5D_0 \rightarrow {}^7F_0$which discloses information about Eu^{3+} occupancy. Its emission appears in 577-584 nm range and its splitting and ratio of the resultant peaks varies, inferring distinct chemical environment and site occupancy.[56,57,71]

The interest in europium is also stimulated by the existence of its multiple stable oxidation states, providing an opportunity to incorporate dual emission centers into the host lattice. Contrary to Eu^{3+}, the Eu^{2+} transition ($5d^1$-$4f^6$) is parity allowed, giving rise to broad and intense emission in the visible range with the molar absorptivity of 200-1000 M^{-1} cm^{-1}.[71] The influence of ligand field on 5d orbitals is more significant compared to the 4f orbital, leading to higher sensitivity to the local environment and shorter lifetime relative to Eu^{3+}. The concurrence of Eu^{3+} and Eu^{2+} in nanomaterials is a viable alternative to codoping and represent an innovative approach to introduce and control a combination of optical properties in complex multifunctional materials. In addition, exploiting Europium oxidation states in solid states materials is advantageous for various technologies such as production of photoluminescent X-ray storage phosphors.

1.4.3 Aliovalent Doping and Alloying

Isovalent substitution of the host atoms with dopants does not introduce additional carriers in NC lattice. However, aliovalent (heterovalent) dopants donate extra electrons (n-type doping) or extra holes (p-type doping) and change photophysical relaxation process of the host and enhance their optoelectronic applications. It must be mentioned that intrinsic self-compensation effect makes it difficult to switch the sign of conductivity from n- to p-type or vice versa.[82–84] For instance, the charge induced in ZnSe structure by incorporation of Cu^+ is compensated by a selenium vacancy.[82]

Rational incorporation of aliovalent impurities into a host lattice generates extrinsic defects with energy levels usually located within the band gap. Substitutional doping of external cation with higher oxidation state than the host lattice cation introduces energy levels below the CBM acting as localized donor states. On the contrary, substitution with a cation possessing lower oxidation state than the host lattice cation results in introducing the acceptor states above the valence band maximum (VBM).[61] The impurity-derived states localize the photogenerated carriers before nonradiative recombination can occur, resulting in an increase in fluorescence quantum yield of doped semiconductors even further.[67] To compensate for the charge imbalance, further defects, such as oxygen vacancies, concurrently form in the lattice.[82] As an example, the incorporation of Ga^{3+} in SnO_2, and Sn^{4+} in Ga_2O_3 can be depicted by Kröger-Vink notation.

$$Ga_2O_3 \xrightarrow{SnO_2} 2Ga'_{Sn} + 3O_O^{\times} + 2V_O^{\bullet} \tag{1.3}$$

$$SnO_2 \xrightarrow{Ga_2O_3} Sn_{Ga}^{\bullet} + 2O_O^{\times} + e' \tag{1.4}$$

The negatively and positively charged states tend to attract owing to the Coulomb interaction, forming donor-acceptor pairs. The ability to induce such extrinsic defects and control their concentration opens up the possibilities for tailoring the functional properties of materials at nanoscale.

Motivated by these opportunities and considering the fact that octahedrally-coordinated Ga^{3+} and Sn^{4+} have similar ionic radii (Ga^{3+} 0.62 Å and Sn^{4+} 0.69 Å), several research groups have attempted to dope Ga_2O_3 with Sn^{4+} or SnO_2 with Ga^{3+} in order to enhance the charge carrier concentration and mobility, or tune the band gap and optical properties of the respective host lattices.[5,43,61,85,86] Since the adopted synthetic methods were based on solid state reactions, the difference between the vapor pressure and density of gallium and tin prevented them from achieving high doping concentrations or alloying, and thus, tuning the aforementioned properties in a broad range. The solubilities of Ga^{3+} in SnO_2 and Sn^{4+} in Ga_2O_3 were reported to be less than 1 mol %. At higher concentrations, phase segregation was reported.[87] Chapters 4 and 6 illustrate how rational selection of reaction condition enables the synthesis of the alloyed gallium tin oxide in the entire composition range, and allows for a design of light emitting NCs and highly active photocatalysts.

1.5 Photocatalysis

Since the second half of the thesis deals with photocatalytic activity of Ga_2O_3 and alloyed gallium tin oxide, this part is dedicated to photocatalysis. After addressing the main environmental concerns, advantages and disadvantages of TiO_2, as the most widely used catalyst, are discussed. Feasible solutions to the countered challenges are sought and eventually, mechanistic view on the involved processes is provided.

1.5.1 Environmental Contaminations

Continuing increase in global population together with the dwindling sources of fresh water has led to more stringent environmental regulations,[88] placing particular emphasis on water remediation and wastewater treatment.[88,89] Various synthetic dyes are indispensable in textile, paper, and other industries involving coloring, but also as human antidotes, antiseptics in veterinary medicine, and for in vitro diagnostics in biology, histology, and hematol.[90] Up to 20 % of all dyes produced worldwide are released in the environment as wastewater and represents a major source of stream pollution.[91,92]

The development of efficient and scalable methods for remediation of such wastewater has become a major societal challenge.

1.5.2 TiO_2: Advantages and Drawbacks

The discovery of water electrochemical photolysis on TiO_2 by Fujishima and Honda[93] in 1972 was the inception of a new era in the generation of semiconductor photocatalysis as it is considered a green technology which could potentially address the global energy and environmental remediation issues. Thereafter a tremendous amount of effort was devoted for TiO_2 photocatalytic activity improvement through adopting various strategies such as morphological modification, surface area and porosity enhancement, controlling the size and phase of the semiconductor, doping and forming heterostructures, etc.[94–101] As the most widely used photocatalyst for water treatment, TiO_2 owes its success to its efficiency, stability, and relative abundance. The majority of studies have focused on the photocatalytic activity of anatase (metastable phase) and rutile (stable phase) TiO_2.[91,102–104] Anatase is generally found to be a better photocatalyst than rutile, despite having a wider band gap by ca. 0.2 eV. This phenomenon is associated with a higher density of localized surface states and slower charge carrier recombination in anatase relative to rutile.[103–106]

Extensive efforts have been devoted to alter the band gap of TiO_2 to absorb a larger portion of the solar spectrum in the visible range.[98,107–110] Because the CB of TiO_2 is located slightly above the reducing potential of water, the only remaining alternative to narrow the band gap is to raise the valence band maxima. However, the valence band maxima composed of O 2p orbitals is typically ca. 3.0 eV and therefore, non-oxygen 2p orbitals contribution is required to lift the VBM.[98] Accordingly, diverse types of ions, such as Cr^{3+}, Ni^{2+}, Nb^{5+}, Sb^{5+} and Cu^{2+}, have been incorporated into the lattice. In lieu of the fact that these ions may act as recombination centers due to unbalanced charge, codoping was regarded as a more feasible option. Systems such as (Mo+C), (Sb+Cr) and (Nb+Ni) combined visible light absorption and high photocatalytic activity.

Despite the photostability and abundance of TiO_2, its innate drawbacks contribute to its remarkably low performance (quantum yields less than 1%).[111] A few of those, which are of primary concerns, are as follows. Only about 10% of photogenerated electrons and holes have lifetime longer than 10 ns and only a small fraction of carriers reaches the surface to react with adsorbates.[94] The conduction band chemical potential is marginally above the water reduction potential, leading to a small driving force of photoexcited electrons in the CB to reduce the pollutants.[107] The large band gap (3.2 and 3.0

eV for anatase and rutile, respectively) hampers the harvesting of a large portion of the solar spectrum and confines it to less than 5%.[112] Consequently, designing an efficient photocatalyst still remains a significant challenge for scientists.

1.5.3 Solutions to Photocatalysis Limitations

In general, the capability of present-day heterogeneous photocatalysts is still unsatisfactory with regard to efficiency and long-term performance. The main obstacle is to control and balance numerous competing processes (Figure 1.5). Charge carrier generation, suppressing charge recombination and charge transportation to the surface are of primary concerns for practical applications. Surface poisoning, compositional and morphological change, particularly under corrosive conditions of photochemical process, also impede industrial implementation. Thus, designing complex heterostructures which allow for synchronous efficient solar spectrum absorption, carrier generation, separation and transportation is crucial for a new era of cost-effective and robust photocatalysts. Such stringent requirements pose technical challenges for chemists in the synthesis of such complex nanomaterials with intricate architectures and optimized progressive charge delivery to active sites.

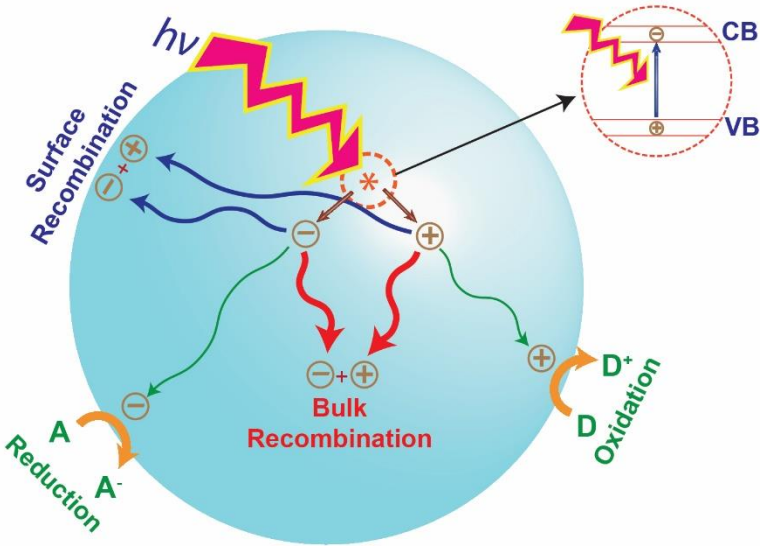

Figure 1.5. Schematic demonstration of a typical photocatalytic process. Electrons and holes are generated by exciting the semiconductor with the light having higher energy than its band gap. Majority of the carriers recombine in the bulk and surface of the semiconductor, as indicated by red

and blue arrows, respectively. Reduction of an electron acceptor (A) by an electron takes place at the surface (green arrow). Holes reaching the surface can oxidize the electron donors (green arrow).

Nanostructuring has been regarded as an excellent method to enhance photocatalytic properties, as zero dimensional nanoparticles possess high surface-to-volume ratio which translates into more catalytically active sites. Moreover, opaque dispersion of macroparticles, caused by light scattering inhibits the collection of mechanistic information. In contrast, scattering by semiconductor nanoparticles drops, relative to macroparticles, due to reduced dimensions and the dispersion appear clear, facilitating the data acquisition to study the mechanism. In addition, photogenerated electrons in the CB of many bulk semiconductors, such as SnO_2 and In_2O_3, cannot be employed as active carriers for the reduction of hazardous waste because of low chemical potential. Band gap widening, as a result of strong quantum confinement effect can enhance the activity of some of these semiconductors through introducing two active carriers. Furthermore, the competition between charge recombination and charge transfer to the surface determines the success of the photon energy into electrochemical reaction conversion.[113] The higher the rate of charge diffusion to the surface, the higher the quantum yield of photocatalysts. The influence of this overwhelming limiting factor is attenuated in nanostructures as the gap between the point of charge generation and reactive sites on the surface lessens.[105] Another consequence of nanostructuring is to increase the density of defects in the structure. The defects are the points where the chemical bonding is altered compared to a perfect crystal, resulting in the reduction of the separation between bonding and antibonding orbitals and rendering additional electronic states within the band gap. The role of the modified electronic structure in controlling the dynamics of charge separation has been the subject of much controversy.[105,113–115] The new energy states are occasionally considered as the recombination sites and therefore are detrimental to photocatalysis. However, recent studies at ultrafast scale (picosecond range) shed more light on the role of the trapped states and revealed that engineering their location and the ratio of surface to bulk defects can be utilized as a degree of freedom to architect the effective photocatalysts.[105,113]

Previous calculations demonstrated that the CB of a p-block metal cation is composed of hybridized sp orbitals, providing a low effective electron mass which enhance the carrier transport from the bulk to the surface and suppress the charge recombination.[36,45] In light of this, photocatalysts with d^{10} electronic configuration (e.g., Ga^{3+} and Sn^{4+}) have been prepared to explore photocatalytic activity of novel non-TiO_2 materials.[40,116–119] SnO_2 is a wide bandgap (3.6 eV) transparent

semiconductor with n-type conductivity. The oxygen vacancies are accounted for its high carrier density of up to 10^{20} cm^{-3},[26] comparable to that of semimetals (10^{17} – 10^{20} cm^{-3}).[120] Moreover, its electronic structure allows for high electron mobility (∼100− 200 cm^2 V^{-1} s^{-1})[62] compared to TiO_2 (0.1- 4 cm^2 V^{-1} s^{-1})[121], rendering its application in dye-sensitized solar cells, and photocatalysis. In spite of these unique strengths, the low CBM of SnO_2 impedes its reduction power in photodegradation of the organic dyes. Effective measures have been taken to foster superior characteristics of this catalyst. The CB offsets with other oxides such as TiO_2[122] and ZnO[123] was exploited in heterojunctions to separate photogenerated carriers and charge recombination retardation. Coupling with graphene,[118,119] small bandgap semiconductors[124] and iodination[125] are few examples attempts to employ the visible portion of the solar spectrum to achieve better photoactivity of this TCO. Overall, SnO_2 has proven to be highly promising for fabricating high-performance catalyst and an alternative to TiO_2.

Reducing power of a catalyst is a function of its CBM energy with respect to vacuum level. The smaller the difference between CBM and the vacuum level, the stronger reducing agent the photocatalyst is. More recently, Ga_2O_3 has emerged as a promising photocatalyst because its VB edge energy is lower and the CB edge energy is higher than the oxidation (O_2/H_2O) and reduction (H^+/H_2) potential of water, respectively. Such band alignment enables the formation of reactive carriers originated from both VB and CB, contrary to SnO_2.[126] As Ga_2O_3 crystalizes in five different polymorphs, it therefore represents an excellent model system for investigation of the influence of the crystal structure and defects on the photocatalytic activity. The phase-dependent photocatalytic activity of Ga_2O_3 has mostly been discussed in the context of the phase junctions,[126–128] in analogy to other oxide-based photocatalytic systems.[6,129,130] It has been reported that *α-β* phase junctions have significantly higher photocatalytic activity than these polymorphs alone.[126,128] The increase in photocatalytic activity has been associated with the charge transfer across the *α-β* phase junction, and an efficient charge separation. Conversely, *γ-β* phase junctions were shown to have lower photocatalytic activity than *γ* and *β* polymorphs,[127] with *γ*- Ga_2O_3 being less active than the *β*- Ga_2O_3.[116,127] The lower activity of *γ*- Ga_2O_3 and *γ-β* phase junctions relative to the *β*- Ga_2O_3 were suggested to arise from the structural disorder characteristic for the defective spinel structure of *γ*- Ga_2O_3. The point defects in Ga_2O_3 and extended defects within the junctions have been proposed to serve as charge recombination centers, resulting in a decrease in the photocatalytic activity. Broader understanding of the role of crystal structure on the photocatalyst efficiency and the origin of phase-

dependent photocatalyst activity is still lacking, but could provide a guideline for the development of new photocatalysts for environmental remediation, energy conversion, and biomedical applications.

1.5.4 Mechanistic View on Photocatalytic Reactions

Advanced oxidation processes (AOPs) have become preferential methods for degradation of various organic pollutants in water.[131,132] These methods involve a wastewater treatment with UV irradiation in combination with ozone, H_2O_2 or Fenton's reagent. To optimize semiconductor photocatalysis-based AOP, a variety of different oxide semiconductors have been investigated,[91,92,133–138] as well as the role of preparation conditions, grain size, surfaces, and structural defects.[70,139–143] Most metal oxides are also polymorphic, with phase-dependent electronic structure and properties.[8,16,19,59,104,144,145] Understanding the role of crystal structure can therefore be critical for the design of improved photocatalysts. Among AOPs, heterogeneous semiconductor photocatalysis has emerged as an effective technology for complete mineralization of most organic pollutants.[96,99,133,135] The basis for this technology is high surface area semiconductors that can generate redox-active electron-hole pairs upon excitation with UV and/or visible light.[96] Upon excitation of a semiconductor (*SC*) in or above the band edge (Eq. 1.5), the resulting conduction band electrons (e_{CB}^-) and valence band holes (h_{VB}^+) can recombine, trapped in sub-band gap states, or oxidize (h_{VB}^+) or reduce (e_{CB}^-) adsorbed molecules on the semiconductor surface. In addition to direct redox degradation of dye molecules, photogenerated electrons can react with O_2 as an electron acceptor, reducing it to superoxide radical anion ($O_2^{\bullet-}$) (Eq. 1.6), while photogenerated holes can react with OH^- or H_2O oxidizing them to $OH^\bullet$ radicals, as shown in Eqs. 1.7 and 1.8, respectively.

$$SC + h\nu \rightarrow SC(e_{CB}^- + h_{VB}^+) \quad (1.5)$$

$$SC(e_{CB}^-) + O_2 \rightarrow SC + O_2^{\bullet-} \quad (1.6)$$

$$SC(h_{VB}^+) + OH^- \rightarrow SC + OH^\bullet \quad (1.7)$$

$$SC(h_{VB}^+) + H_2O \rightarrow SC + H^+ + OH^\bullet \quad (1.8)$$

These and other radical species (such as peroxide radicals, $HO_2^\bullet$) are strong oxidizing agents and significantly contribute to the heterogeneous decomposition of organic molecules in water. The efficiency of molecular degradation is, therefore, ultimately determined by the carrier dynamics, initially *via* competition between exciton recombination and charge carrier trapping or transfer, and subsequently *via* competition between trapped carrier recombination and interfacial charge transfer.[96]

Increasing the photocatalytic quantum efficiency can be achieved by decreasing the rate of electron-hole recombination or increasing the rate of interfacial charge transfer.

The comprehensive study performed by Rothenberger et. al,[146] sheds light on the dynamics of electron-hole generation and recombination:

$$SC + h\nu \rightarrow SC\ (e_{CB}^{-} + h_{VB}^{+}) \tag{1.9}$$

$$SC\ (e_{CB}^{-} + h_{VB}^{+}) \rightarrow\ SC\ \left(e_{trap}^{-} + h_{VB}^{+}\right) \tag{1.10}$$

$$SC\ (e_{CB}^{-} + h_{VB}^{+}) \rightarrow\ SC\ \left(e_{CB}^{-} + h_{trap}^{+}\right) \tag{1.11}$$

$$SC\ \left(e_{trap}^{-} + h_{VB}^{+}\right) \rightarrow SC \tag{1.12}$$

$$SC\ \left(e_{trap}^{-} + h_{trap}^{+}\right) \rightarrow SC \tag{1.13}$$

The absorption of the light by a semiconductor is an ultrafast process and takes place in the femtosecond time domain (Eq. 1.9), followed by conduction band electron trapping in ca. 30 ps (Eq. 1.10). On the other hand, hole trapping (Eq. 1.11) requires a much longer time (250 ns). When the concentration of electron-hole pairs is high, the charge carrier recombination occurs within a nanosecond (Eq. 1.12). Under this condition, the photocatalytic activity is low unless the charge transfer to the surface is very rapid and a hole trapping agent (OH^{-}) is preadsorbed on the surface of the catalyst. At low concentration of electron-hole pairs, the lifetime of the pair was determined to be ca. 30 ns. The hole trapping (Eq. 1.11) can now compete with the recombination process (Eq. 1.12). It is believed that trapped holes are unreactive towards electrons, leading to the extension of the lifetime of the excited carriers to microsecond regime.[95,96,99,146]

1.6 Purpose and Scope of the Thesis

Principally, this thesis targets a more profound understanding of defect chemistry of nanomaterials in the hope that the acquired knowledge paves the way of nanomaterials for desired functionalities such as lighting, photocatalysis and water splitting. The main impetus for the development of novel functional nanomaterials comes from the pressing need for sustainable energy, achieved in a scalable fashion and environmentally-friendly techniques.

The first part of the thesis illustrates the coexistence of Eu^{2+} and Eu^{3+} in *rh*- and *bcc*-In_2O_3 NCs, achieved by adjusting the NC synthesis conditions. Blue (Eu^{2+}) or red (Eu^{3+}) emission was achieved

in both *bcc*- and *rh*-In_2O_3 NCs owing to the controlled interactions of dopant ions with the host lattice defect sites. Both dopant centers show dramatically different behavior in the two NC lattices owing to the difference in NC size, and the structure and concentration of oxygen vacancies. Furthermore, the ability to impact the formation and electronic structure of NC native defects in both phases allows for elucidation of their interactions with dopant centers and their role in sensitization of the dopant emissions. The Eu dopant oxidation state and concentration, and nanocrystal size and structure are effective tools for controlling the defect density in In_2O_3 nanocrystals.

In the next section, hydrothermal synthesis of ternary gallium tin oxide ($Sn_{1-x}Ga_xO_{2-0.5x}$, $0 \leq x \leq 1$, further denoted by GTO) NCs in the entire composition range is reported, demonstrating a modulation of the PL throughout the visible part of the spectrum. The effects of the reaction duration, synthesis temperature, and NC composition on the photoluminescence quantum yield (PLQY) and lifetime of the NCs are discussed. The interaction among intrinsic and dopant-induced defects can lead to phosphors with high PLQY (> 40 %) even in SnO_2 NC lattice with intrinsically low PLQY (ca. 0.5 %). The ability to simultaneously control the emission efficiency and fine-tune the PL of these broadly-emitting NCs allows for the design of new energy-efficient lighting sources with optimal photopic-to-scotopic ratio and other lighting characteristics.

The third part of the thesis presents a superior photocatalytic efficiency of γ-Ga_2O_3 relative to β-Ga_2O_3 prepared from the same colloidal NCs, using Rhodamine 590 (Rh-590) and methylene blue (MB) dyes. The photocatalytic efficiency is strongly correlated with the electronic structure, location, and concentration of native defects, suggesting their role in reversible trapping of the photogenerated charge carriers and charge separation. The long lifetime of the native defect states and their proximity to the γ-Ga_2O_3 NC surface promotes interfacial charge transfer responsible for the degradation of dye molecules, while reducing the effect of charge recombination. The results of this work indicate that NC structure and size allow for the control of the charge carrier dynamics, enabling the enhancement of the photocatalytic activity of polymorphic metal oxides.

Finally, the sol-gel synthesis of ternary gallium tin oxide NCs throughout the entire composition range is demonstrated. Using photoluminescence spectroscopy, the concentration of defects in the NCs can be adjusted *via* changing the composition. A high intensity in steady-state PL spectroscopy generally indicates a high concentration of radiative centers. The effect of composition on the electron–hole recombination kinetics was monitored by employing time-resolved PL which reveals

information on the timescale at which the carrier recombination/transfer takes place. The effect of electronic structure modification and surface area on photocatalytic activity of GTO NCs is discussed. The rate of photodegradation of organic pollutants on GTO NCs surpass that of the benchmark photocatalyst, Aeroxide P25. By employing different scavengers, the role of the dopant on modulating the relative position of CBM and affecting its reduction potential is elucidated. The attained knowledge of this work on controlling the chemistry of defects, their concentrations and charge recombination dynamics open a new avenue to develop highly efficient photocatalysts.

The results of this work provide deeper understanding of the role of defect chemistry in tailoring the optoelectrical properties of TCOs which is pivotal for the design of new functional materials. Developing the concept of rational doping to induce extrinsic defects and, hence, alter the electronic structure of nanoscale materials is a promising and vital area of research, serving as a prerequisite for the architecture of novel multifunctional systems.

Chapter 2
Experimental Procedures

2.1 Materials

All reagents and solvents are commercially available, and were used as received without further purification. Indium acetylacetonate ($In(acac)_3$; 98%), gallium acetylacetonate ($Ga(acac)_3$, 99.99%), gallium(III) nitrate hydrate ($Ga(NO_3)_3$. xH_2O, 99.99%), tin(IV) chloride pentahydrate ($SnCl_4 \cdot 5H_2O$, 98%) and europium chloride ($EuCl_3$; 99.9%) were purchased from STREM Chemicals. Oleylamine (OAm; 70%), tri-n-octylphosphine oxide (TOPO; 90%), oleic acid (OA, 90%), ethanol (EtOH, HPLC grade), dodecylamine (DDA, 98%), ammonium hydroxide (NH_4OH, 28.0−30.0%), 1,4-dioxane (> 99.0%), rhodamine 590 (Rh-590) and hexane (HPLC grade) were purchased from Sigma-Aldrich Corporation. Methanol (MeOH, 99.9%) was obtained from Fisher Chemicals.

2.2 Syntheses and Preparations

2.2.1 Synthesis of Eu-Doped Indium Oxide Nanocrystals

The synthesis of colloidal In_2O_3 NCs was performed in OAm as a coordinating solvent and reducing agent.[12] In a typical synthesis, in a 100 mL round bottom flask, 1.0 g of $In(acac)_3$ and 10 g of OAm were combined with different amounts of $EuCl_3$ (0.5−15 mol % relative to In). The solution was magnetically stirred and heated to desired temperature (200-300 ^oC), and refluxed over the course of 1 h. The resulting suspension was cooled to room temperature, precipitated, and washed three times with ethanol. After the final washing, TOPO was added to the precipitated NCs in an approximately volume-equivalent amount. The NCs were then heated and stirred in TOPO in a 90 ^oC oil bath for 1 h, and subsequently precipitated and washed with ethanol. The TOPO treatment was repeated two more times. Finally, TOPO-capped NCs were dispersed in hexane for spectroscopic measurements.

2.2.2 Ga_2O_3 Photocatalyst Synthesis and Processing

2 g of $Ga(acac)_3$ was mixed with 20 g of OAm in a three-neck round-bottom flask under a flow of argon.[11] The solution was heated up to the desired synthesis temperature (200°C or 300°C) and refluxed at that temperature for 1 hour. Once cooled, the NCs were collected by the addition of ethanol and centrifuged. This was repeated two more times to rinse the NCs, and the product was

dried on a watch glass with acetone. The dried product was then annealed in a preheated furnace (Vulcan A-130) at a designated temperature ranging from 400 to 1025°C for 2 hours.

For the synthesis of In^{3+}-doped γ-Ga_2O_3 NCs, 10 % of $Ga(acac)_3$ was replaced with $In(acac)_3$ in the reaction mixture, and the reaction was performed at 300 ºC. The obtained NCs were treated as described above for γ-Ga_2O_3 NCs, and subsequently annealed at 400 ºC for 2 hours.

2.2.3 Hydrothermal Synthesis of GTO Nanocrystals

In a typical synthesis of SnO_2 NCs, 1g of $SnCl_4 \cdot 5H_2O$, 7 mL MeOH, 20 mL OA and 4 mL OAm were added into a 45 mL Teflon-lined stainless-steel autoclave.[27] The autoclave was transferred to a preheated oven (190 ºC). The reaction duration varied from 4 to 32h, after which the autoclave left to cool down to room temperature naturally. The obtained xerogel was washed with ethanol and centrifuged 3 times, followed by TOPO treatment at 90 ºC for 30 minutes. Next, NPs were washed with ethanol, centrifuged and finally dispersed in hexane for optical measurements. A certain portion of tin chloride (10-100%) was replaced with $Ga(NO_3)_3.xH_2O$ to obtain alloyed GTO NPs throughout the full composition range.

2.2.4 Sol-gel Synthesis of GTO Photocatalysts

In a typical sol-gel synthesis of GTO NCs, 1.4 g of $SnCl_4 \cdot 5H_2O$ and varying amount of $Ga(NO_3)_3.xH_2O$ (from 0 to 100 mol %) were added to 25 mL of deionized water and the solution was stirred till all precursors dissolved.[147] Having cooled down the reaction mixture in an ice bath for 15 min, the nucleation of particles was stimulated by dropwise addition of NH_4OH (30 %) until reaching pH 6. After leaving the reaction beaker for 3 h, the particles were washed with deionized water 3 times. Next, a pipet-full of NH_4OH was added to the suspension in 15 min intervals until it became completely transparent. After refluxing this suspension for 15 h at 90 °C, and then cooling it to room temperature, the NCs were extracted by the addition of 1,4-dioxane, collected by centrifuging, and washed with ethanol three times. The main portion of the product was dried on a watch glass at room temperature for photocatalysis measurements. A small amount of the precipitated NCs were surface-capped for optical measurements. They were resuspended in an excess amount of melted DDA and heated at 120 °C for 30 min resulting in a clear suspension. The suspensions were precipitated and washed with ethanol. Finally, DDA-capped NCs were treated with TOPO at 140 °C for 1 h, and

afterward washed with ethanol three times. TOPO treatment was repeated two more times. In the final step, NCs were suspended in a small amount of hexane for optical measurements.

2.3 Nanocrystal Structural Characterization

Nanocrystal size and structure were characterized by powder X-ray diffraction (XRD), transmission electron microscopy (TEM) and Brunauer-Emmet-Teller (BET) surface area.

XRD patterns were recorded with INEL XRG 3000 powder diffractometer having a Cu Kα radiation source (λ = 1.540598 Å), an INEL CPS 120 curved position sensitive detector operating at 30 kV and 30 mA with germanium crystal monochromator. After loading powder samples into an aluminum sample holder, each pattern was recorded for up to 1 h to acquire sufficiently high signal-to-noise ratio

TEM imaging and energy dispersive X-ray spectroscopy (EDX) elemental analysis were performed with a JEOL-2010F microscope operating at 200 kV. A small portion of sample was diluted in toluene, followed by a 10-minute sonication. The dilute suspensions of colloidal NCs in toluene were drop casted on TEM copper grids with lacey formvar/carbon support films purchased from Ted Pella, Inc. The europium doping concentrations determined by EDX were in good agreement with the concentrations determined by inductively coupled plasma atomic emission spectrometry (ICP-AES), and are defined as a percent of substituted In^{3+} ions.

TEM specimens of Ga_2O_3 photocatalysts were prepared by dropping an ethanol suspension of NCs on a copper grid containing lacey Formvar/carbon support film.

TEM samples of hydrothermally synthesized GTO NPs, synthesized by sol-gel method, were prepared by dropping a hexane solution of NCs on a copper grid containing carbon support film (Ted Pella, Inc), while maintaining the other parameters as described above.

By dropping a hexane solution of GTO photocatalysts on a copper grid containing lacey Formvar/carbon support film (Ted Pella, Inc.), TEM samples were prepared.

BET surface area measurements were conducted on a Quantachrome Autosorb ASiQ-MP instrument, using N_2 as the probing gas. The sample cell was outgassed at 250 °C for approximately 2 hours prior to measurement in order to remove any water present on the surface of the sample.

2.4 Spectroscopic Measurements in the UV-Visible Range

2.4.1 Absorption and PL Measurements

All spectroscopic measurements were performed at room temperature. The absorption spectra of colloidal NCs were collected with a Varian Cary 5000 UV−vis-NIR spectrophotometer, in a 1 cm path length quartz cuvette with transparency range 170 – 2700 nm. Steady-state PL excitation and emission spectra of colloidal NCs were measured with a Varian Cary Eclipse spectrometer, using standard quartz fluorescence cuvettes. For the direct comparison of PL intensities, the concentrations of colloidal suspensions of NCs were adjusted to exhibit the band gap absorbance of 1.0 at 300 nm and 270 nm for *bcc*-In_2O_3 and *rh*-In_2O_3 NCs, respectively. For Eu^{3+} PL emission measurements, the samples were excited at the excitation band maxima for *bcc*-In_2O_3 and *rh*-In_2O_3 NCs. The PL spectra of Eu^{2+} were measured upon excitation at 300 nm. For PL excitation measurements, the emission was monitored at the maximum of the Eu^{2+} 4f−5d transition band (402 nm) or at the maximum of the Eu^{3+} $^5D_0 \rightarrow {}^7F_2$ peak (614 nm). Emission and excitation spectra for Eu^{3+} dopants were recorded in the phosphorescence mode (with 0.1 ms delay time, 5 ms gate time, 1.00 nm data interval and 0.10 s averaging time), using a Xenon flash lamp as the excitation source. High-resolution PL spectra were measured with a Renishaw 1000 spectrometer. For these measurements the NCs were deposited on a silicon substrate and excited at ca. 260 nm using frequency-tripled Millenia-pumped Tsunami laser (SpectraPhysics).

Powder samples for PL measurements of Ga_2O_3 were prepared by adhering samples to a glass substrate using double sided tape. Samples were excited at 260 nm with the excitation and emission slits set to 5 nm, using Varian Cary Eclipse spectrometer.

PL spectra of GTO NPs and photocatalysts were recorded at room temperature with a Varian Cary Eclipse fluorescence spectrometer. Samples were excited at 240 nm with the excitation and emission slits set to 5 nm.

2.4.2 Time-resolved PL Measurements

Time-resolved measurements of Eu^{2+} dopant and defect-based DAP emissions were performed by time-correlated single photon counting (TCSPC) method with a Horiba Jobin Yvon IBH Ltd. spectrometer. A 250 nm NanoLED (IBH Ltd.) was used as the excitation source, and the signal was monitored at the corresponding emission band maxima. The instrument response function (IRF) was

recorded by detecting the scattered excitation using a Ludox solution (Sigma Aldrich), and the data were fit with exponential function. Time decay of Eu^{3+} was measured with a Varian Cary Eclipse fluorescence spectrometer. In a typical experiment, the delay was set to 0.01 ms and the excitation wavelength was 230 nm. The signals were detected at the maximum of the $^5D_0 \rightarrow ^7F_2$ peak (614 nm).

Time-resolved measurements of Ga_2O_3 was carried out using the same instrument and excitation source as described above. However, powder samples were prepared by adhering samples to a glass substrate using double sided tape.

Time-resolved measurements of GTO NPs and photocatalysts were recorded employing the same instrument, excitation source and conditions described above for Eu-doped In_2O_3 NCs.

2.4.3 Determination of Relative PLQY of GTO NCs

A solution of quinine bisulfate (QBS) in 1 N sulfuric acid and 1,4-bis(5-phenyloxazole-2-yl)benzene (POPOP) in cyclohexane were used to obtain the relative PLQY of the NCs on the basis of the following equation:

$$Q_x = \frac{Q_R \times A_R \times E_x \times \eta_x^2}{A_X \times E_R \times \eta_R^2}$$

where the subscripts *R* and *X* denotes the quantities of the reference and unknown compound, respectively, *Q* is the photoluminescence quantum yield, *A* is the absorbance of the solution, *E* is the integrated fluorescence intensity, and η is the refractive index of the solution. The PLQY of QBS and POPOP was reported to be 0.55 and 0.97 under these conditions. The averaged values for PLQY of NCs with respect to QBS and POPOP are reported.

2.4.4 Conjugation of GTO NCs with Atto-590

A solution of GTO NCs in hexane was prepared with absorbance of 0.5 at 240 nm. 4 mL of this solution was added to 1 mL aqueous solution of Atto-590 with the concentration of 5.9 μM, forming a bilayer. The bilayer emulsion was gently stirred and the non-polar portion was extracted every 10 minutes to monitor the emission colour under UV lamp. After 40 minutes of stirring and binding the dye to the surface of GTO NCs, the emission colour turned white, followed by PL spectrum collection.

2.5 Photocatalysis

2.5.1 Photocatalytic Activity Evaluations

Photocatalysis was carried out in a 100 mL beaker containing 12 mg of Ga_2O_3 catalyst suspended in 50 mL of 5 mg/L Rh-590 solution. The reaction vessel was situated on a stir plate 20 cm below dual 40 W 254 nm fluorescent tube lamp. Before irradiation, the solution was stirred for 30 minutes in dark to ensure adsorption-desorption equilibrium was achieved. The concentration of unreacted Rh-590 was determined by monitoring the absorbance at the maximum of $S_0 \rightarrow S_1$ band at 520 nm over the light exposure time, by using Varian Cary 5000 UV-vis-NIR spectrophotometer. All photocatalytic measurements were performed identically, and the calculated apparent quantum efficiency (AQE) values are given in the relevant chapter.

To test recyclability, once all the dye was degraded, the NCs were allowed to settle to the bottom of the flask and collected. The powder was allowed to dry at 80 °C for 90 minutes before repeating the photocatalytic measurements. Scavengers were used to determine the species involved in photocatalysis. A scavenger (KSCN, methanol, ascorbic acid, or isopropanol) was added immediately before irradiation to achieve a concentration of 10 mM. The reaction and measurements were then performed as described.

Photocatalytic evaluations of GTO NCs was conducted according to procedure reported above for Ga_2O_3 particles, with the exception of running a 15-minute sonication in dark to reach adsorption-desorption equilibrium instead of half an hour stirring. To identify the species involved in photocatalysis, different scavengers were used. Before irradiation, a scavenger ($NaHCO_3$, methanol, or $FeCl_3$) was added to the beaker to achieve a concentration of 10 mM. N_2 gas was also utilized as a superoxide radical scavenger and it was blown into the solution for 15 min prior to turning on the UV lamps. Afterwards, the measurements were carried out as described.

2.5.2 Determination of the apparent quantum efficiency (AQE):

The apparent quantum efficiency (ϕ_X) was calculated based of the following equation.[96]

$$\Phi_X \equiv \frac{\pm(d[X]/dt)}{d[h\nu]_{inc}/dt}$$

ϕ_X: the apparent quantum efficiency for chemical species (Rh-590)

d[X]/d*t*: the initial rate of formation or loss of chemical species (mol/Ls or mol/m^3s)

d[*hv*]/d*t*: the incident photon flux per unit volume (moles of photon/m^3s)

d[X]/d*t* can be extracted from a plot of [Rh-590] (mol/L) versus time (seconds). The slope of this plot equals d[X]/d*t*. d[*hv*]/d*t* is determined by measuring the power of irradiation per unit area at the same height as the top of the Rh-590 solution and determining the photon flux per unit volume of the dye solution.

2.6 X-ray Absorption Spectroscopy Measurements

The Eu M-edge X-ray absorption spectroscopy measurements were performed at the Spherical Grating Monochromator (SGM) beamline 11ID-1 at the Canadian Light Source. Eu-doped In_2O_3 NC samples in the powder form were deposited on the carbon tape attached to the custom-made copper sample holder. The sample stage was inserted in ultra-high vacuum (UHV) X-ray chamber using a load-lock procedure. The signal was detected by both total electron yield (TEY) and total fluorescence yield (TFY) using channel plate detectors.

2.7 Multiplet Structure Calculations

The ratio of Eu^{2+}/Eu^{3+} in Eu-doped In_2O_3 NC samples was determined by comparison of measured Eu M-edge X-ray absorption spectra (XAS) with the linear combinations of the theoretical Eu^{2+} and Eu^{3+} spectra, which were reproduced within the atomic multiplet calculations. The spin-orbit coupling term was included in the calculations.[148] Assuming dipole selection rule $\Delta J = 0, \pm 1$ in the calculation reduces the total number of final states and reproduces simulated $M_{4,5}$-edge spectra. The simulated relative intensities corresponding to transitions in Eu^{2+} ($3d^{10}4f^7$ ($^8S_{7/2}$)→ $3d^94f^8$ (^7F)) and Eu^{3+} ($3d^{10}4f^6$ (^7F)→ 3d94f7 (^8S)) are shown in Figure 3.6a (vertical lines). The Slater integral parameters (F^k) for the Eu^{2+} ground state $3d^{10}4f^7$ configuration are F^2=10.398, F^4=6.486, F^6=4.655, and the spin orbit coupling parameter is 0.160 eV. For the final Eu^{2+} state ($3d^94f^8$) the Slater integral parameters are F^2=11.031, F^4=6.896, F^6=4.954, G^1=4.921, G^3=2.882, G^5=1.990, and spin-orbit coupling parameter is 0.187 eV. Similarly, for Eu^{3+} the Slater integral parameters for the configuration of the initial state $3d^{10}4f^6$ are F^2=11.266, F^4=7.071, F^6=5.088, and the spin-orbit coupling parameter is 0.175 eV. For the final state of Eu^{3+} ($3d^94f^7$) the Slater parameters are F^2=11.840, F^4= 7.442, F^6=5.358, G^1= 5.326, G^3=3.121, G^5=2.156, and spin-orbit coupling term is 0.202 eV. The values of the Slater parameters used in the calculations are consistent with those reported in the literature.[148,149]

Chapter 3

Native Defects Determine Phase-Dependent Photoluminescence Behavior of Eu^{2+} and Eu^{3+} in In_2O_3 Nanocrystals

3.1 Overview

Solution phase synthesis and manipulation of colloidal nanocrystals offers various opportunities to control their optical and electrical properties *via* intentional impurity doping, surface modification, and structural transformation. Simultaneous control of these processes is often challenging due to the required reaction conditions and the nature of the given colloidal NCs.[12] Wide band gap metal oxides are a unique class of materials characterized by polymorphism, transparency, and electrical conductivity.[14] Such combination of properties makes them exploitable for numerous technologies including photovoltaics, sensors, displays, lighting, and photocatalysis.[14,150,151] In_2O_3 is one of the extensively studied transparent metal oxides because of its wide transparency, and the possibility of generating high n-type conductivity and carrier mobility.[14,150] There are two known polymorphs of In_2O_3 adopting body-centered cubic (*bcc*-In_2O_3, bixbyite) and rhombohedral (*rh*-In_2O_3, corundum) crystal structures.[20] These polymorphs also have different electronic structure,[152] allowing for the control of the optical and electrical properties by structural transformation at high pressure and temperature. Our group has recently shown that high energy *rh*-In_2O_3 phase can be stabilized in NCs smaller than ca. 5 nm by controlling the growth kinetics during colloidal synthesis.[7,8,19] This metastable form is shown to be an intermediate in the growth of *bcc*-In_2O_3 NCs, which is a stable form of In_2O_3 at room temperature.

One of the attractive means of manipulating optical properties of colloidal NCs is through substitutional doping with luminescent impurities. Lanthanide(III) ions have attracted much attention due to the unique nature of f-f transitions, resulting in sharp photoluminescence spectra, stability to photobleaching, and long-lived excited states suitable for upconversion PL.[71] However, three-valent lanthanide ions generally require a sensitization by a host matrix due to the small absorptivity of intra-4f transitions. Some lanthanides can also be stabilized in 2+ oxidation state,[57,153,154] leading to uniquely different PL properties and the possibility of direct excitation into the parity allowed d-f transitions. While some applications require a single color emission, the coexistence of both oxidations states in a host lattice can be useful for multiplexed imaging and the design of X-ray

storage phosphors for digital radiography and medical imaging.[71,153,154] Most notable example is the europium ions; Eu^{3+} shows red emission arising from $^5D_0 \rightarrow {}^7F_J$ transitions, while Eu^{2+} usually emits in blue due to parity allowed transition $4f^6 5d^1 \rightarrow 4f^7 ({}^8S_{7/2})$. Both Eu^{2+} and Eu^{3+} have comparable ionic radii to In^{3+} and can adopt six-coordinate environment when substitutionally doped in both bixbyite and corundum phases. Furthermore, the ability to control NC structure and Eu oxidation state can lead to simultaneous manipulation of the optical and electrical properties, and reveal the role of host lattice in the stabilization and sensitization of lanthanide dopants.

Here the coexistence of Eu^{2+} and Eu^{3+} in *rh*- and *bcc*-In_2O_3 NCs, which is achieved by adjusting the NC synthesis conditions, is demonstrated. Both dopant centers show dramatically different behavior in the two NC lattices owing to the difference in NC size, and the structure and concentration of oxygen vacancies. Furthermore, the ability to impact the formation and electronic structure of NC native defects in both phases allows for elucidation of their interactions with dopant centers and their role in sensitization of the dopant emissions.

3.2 Results and Discussion

3.2.1 The Influence of Dopant on the Host Crystal Structure

The Eu-doped In_2O_3 NCs having variable crystal structure were synthesized by modifying the procedure for the synthesis of pure In_2O_3 NCs.[19] Briefly, the samples were synthesized at different temperatures (200-300 ºC) from oleylamine as a coordinating solvent, using indium acetylacetonate ($In(acac)_3$) and $EuCl_3$ as precursors (see section 2.2.1 for experimental details).

Figure 3.1a,b shows typical TEM images of 3.9 % Eu-doped In_2O_3 NCs synthesized at 300 ºC. These NCs are well dispersed and have an average size of 9.6±1.7 nm. As the concentration of $EuCl_3$ increases, individual NCs undergo oriented attachment forming flower-like nanostructures (Figure 3.1c and Figure A.1 in Appendix A). The oriented attachment of In_2O_3 NCs has been observed for high ionic strength of the reaction mixture.[16] High concentration of an ionic dopant precursor could lead to the displacement of coordinating ligands on NC surfaces by anions in solution (Cl^-), causing a limited protection and anisotropic charging of NC surfaces, which results in the formation of local dipole moments, and oriented van der Waals interactions of NCs. All samples prepared at 300 ºC have bixbyite structure, as shown in Figure 3.1f (red trace) and Figure 3.2a. Figure 3.1d, e shows TEM images of 5.3 % Eu-doped In_2O_3 NCs synthesized at 200 ºC. These NCs are smaller than 5 nm

and have corundum structure (Figure 3.1f, black trace). At higher Eu^{3+} precursor concentration (Figure 3.2b) the obtained NCs attain *bcc*-In_2O_3 structure, similarly to the samples synthesized at 300 ºC. While the presence of impurities in the reaction mixture tends to inhibit NC growth,[12] increased concentration of Eu^{3+} appears to stimulate the growth of *bcc*-In_2O_3 NCs. This is consistent with the fact that Eu_2O_3 is isostructural to *bcc*-In_2O_3, favoring *rh*- to *bcc*-phase transformation.[12]

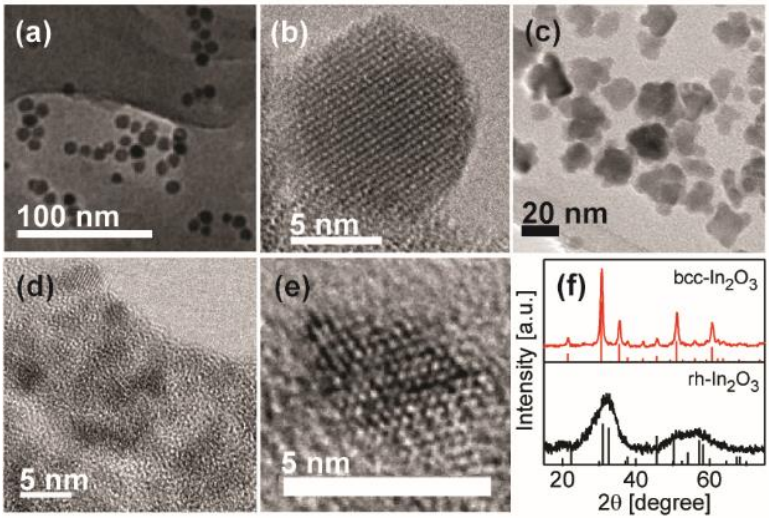

Figure 3.1. (a-e) TEM images of (a,b) 3.9 % and (c) 11.5 % Eu-doped In_2O_3 NCs synthesized at 300 °C, and (d,e) 5.3 % Eu-doped In_2O_3 NCs synthesized at 200 °C. (b) and (e) are lattice-resolved images of typical NCs from (a) and (d), respectively. (f) XRD patterns of NCs in (a) and (d) having *bcc*-In_2O_3 (red, top) and *rh*-In_2O_3 (black, bottom) crystal structure, respectively. Vertical lines represent the corresponding bulk patterns.

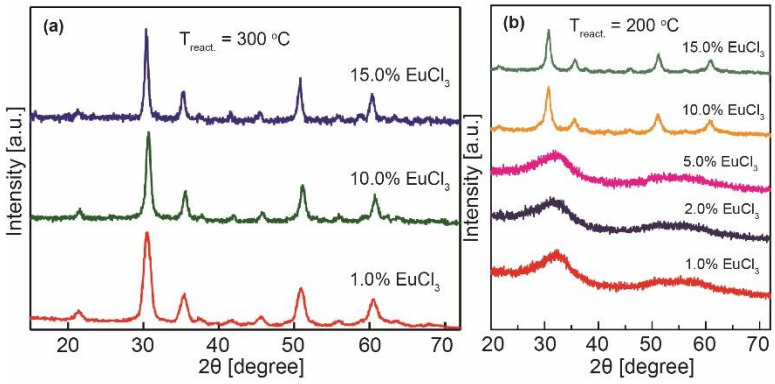

Figure 3.2. XRD patterns of Eu-doped In_2O_3 NCs synthesized at (a) 300 °C and (b) 200 °C with different starting concentrations of $EuCl_3$ precursor, as indicated in the graph. All XRD patterns can

be assigned to bixbyite-type crystal structure in (a). For low starting concentrations of Eu precursor (below ca. 5%) the NCs have corundum-type crystal structure (*rh*-In_2O_3), while for higher Eu concentrations they adopt cubic bixbyite structure (*bcc*-In_2O_3) in (b).

3.2.2 Spectroscopic Studies on Eu-In_2O_3 in the UV-Vis Range

The PL properties of Eu-doped In_2O_3 NCs synthesized at different temperatures are shown in Figure 3.3. The NCs synthesized at 300 ºC show only minor delayed emission from Eu^{3+} (Figure 3.3a, red). The excitation spectrum corresponding to Eu^{3+} ($^5D_0 \rightarrow {}^7F_2$) PL at 614 nm (purple) coincides with the NC band gap absorption, indicating that Eu^{3+} PL is sensitized by the *bcc*-In_2O_3 NC host lattice, albeit very weakly. A dominant emission feature for this sample is a relatively broad band centered at ca. 400 nm (Figure 3.3b, blue). The excitation spectrum corresponding to this emission (Figure 3.3b, yellow) also overlaps with the band gap absorption, but has a different band shape and is blue shifted relative to the Eu^{3+} excitation spectrum. Based on its energy, band shape, and intensity, this PL band is assigned to the parity allowed $4f^6 5d^1 \rightarrow 4f^7$ transition in Eu^{2+}.[155]

Although the reaction is performed in reducing environment of oleylamine, it is unusual for a divalent Eu to substitute for a trivalent host cation. This is in contrast to the Eu^{3+} substitution for a divalent host cation, which has been suggested to lead to "abnormal" Eu^{3+} reduction due to the charge compensation.[156] In addition to Eu^{2+} emission, a much broader band is observed at lower energies, which increases with increasing doping concentration (Figure 3.4a). The position, shape, and width of this new band are very similar to defect-based donor-acceptor pair recombination emission observed for Ga_2O_3 and *rh*-In_2O_3 NCs,[1,11] suggesting the formation of native defects in *bcc*-In_2O_3 NCs concurrently with the incorporation of Eu dopants. In the DAP emission mechanism in Ga_2O_3 NCs the majority donor states have been associated with oxygen vacancies ($V_O^{\bullet}$), while the minority acceptor states are suggested to be due to Ga-O vacancy pairs.[10,54,55] Contrary to *rh*-In_2O_3, undoped *bcc*-In_2O_3 NCs obtained at higher temperatures (> 230 °C) do not show any appreciable defect-based PL.[1] This difference is likely associated with smaller surface-to-volume ratio and lower concentration of defects in *bcc*-In_2O_3 NCs, consistent with the finding that oxygen vacancy formation energy decreases with decreasing distance from the surfaces.[157] It has been suggested that dopant ions having lower oxidation state relative to the host lattice cation attract anion vacancies having a net positive charge, due to electrostatic interactions.[158] Accordingly, Eu^{2+}, which forms a negatively charged site in In_2O_3, can attract and stimulate the formation of oxygen vacancies. Given the absence of defect-

based PL in *bcc*-In_2O_3 NCs, the appearance of DAP band in Eu-doped *bcc*-In_2O_3 NCs serves as a direct evidence of the mutual interaction between defects and dopant ions. Figure 3.3c shows steady-state (green) and time-delayed (red) PL spectra of 5.3 % Eu- doped *rh*-In_2O_3 NCs synthesized at 200 ºC. The steady state spectrum consists of a broad DAP band spanning most of the visible range, which is structureless on the high energy side and exhibits a set of sharp features between ca. 600 and 700 nm (see also Figure 3.4b). These features match the peaks for Eu^{3+} ($^5D_0 \rightarrow {}^7F_J$) emission. The DAP emission has a much shorter lifetime relative to f-f transitions of Eu^{3+}, and the delayed PL measurements clearly confirm the spectrum characteristic for Eu^{3+} (Figure 3.3c, red).[159,160] The excitation spectrum corresponding to Eu^{3+} ($^5D_0 \rightarrow {}^7F_2$) PL at 614 nm (purple) coincides with the NC band gap absorption, indicating that Eu^{3+} PL is relatively strongly sensitized by the NC host lattice.

The time-resolved data of Eu-doped *bcc*-In_2O_3 NC samples synthesized at different temperatures are shown in Figure 3.3d. For NCs synthesized at 300 ºC (Figure 3.3d, top) the lifetime of Eu^{2+} emission (blue) is significantly shorter than the defect emission (green). The average lifetimes obtained by exponential fitting of the decays are 83 ns and 0.57 μs for Eu^{2+} and DAP PL, respectively. For the samples synthesized at 200 ºC (bottom), the lifetime of Eu^{3+} (red) is much longer than the lifetime of the DAP emission (0.55 ms for Eu^{3+} vs 0.18 μs for DAP). While shortening of the DAP emission lifetime for NCs synthesized at 200 ºC can be explained by the smaller defect separation (Figure 3.5a),[10,55] the faster decay of Eu^{2+} relative to Eu^{3+} emission reflects higher recombination probability in Eu^{2+} due to parity allowedness of d-f transitions. Now, the dependence of the PL intensities on the doping concentration for the samples synthesized at 300 ºC (Figure 3.3e) and 200 ºC (Figure 3.3f) can be summarized. At 300 ºC, the dominant Eu^{2+} PL (blue squares) increases with doping concentration and begins to saturate at high doping levels, most likely due to self-quenching. Meanwhile, the emission of Eu^{3+} remains negligible throughout the entire doping concentration range (open red triangles). The DAP emission, which is absent in pure *bcc*-In_2O_3 NCs[1] appears in doped NCs and increases with doping concentration (green circles). It is clear that this DAP emission correlates with the Eu^{2+} emission, suggesting its role in attracting and stabilizing the oxygen vacancy sites. The situation is reverse at 200 ºC; the Eu^{2+} emission is vanished, while the Eu^{3+} PL increases with doping concentration before being quenched at high doping levels as a result of cross-relaxation processes (red triangles). The DAP emission (green circles), initially strong, drops in intensity above ca. 6 % doping concurrently with the transformation of NCs from *rh*- to *bcc*-phase. This is associated with the change in phase and an increase in NC size (Figure 3.5b). Other types of

surface defects characteristic for oxide NCs (i.e. hydroxyl group) could potentially also form donor states and participate in DAP recombination.

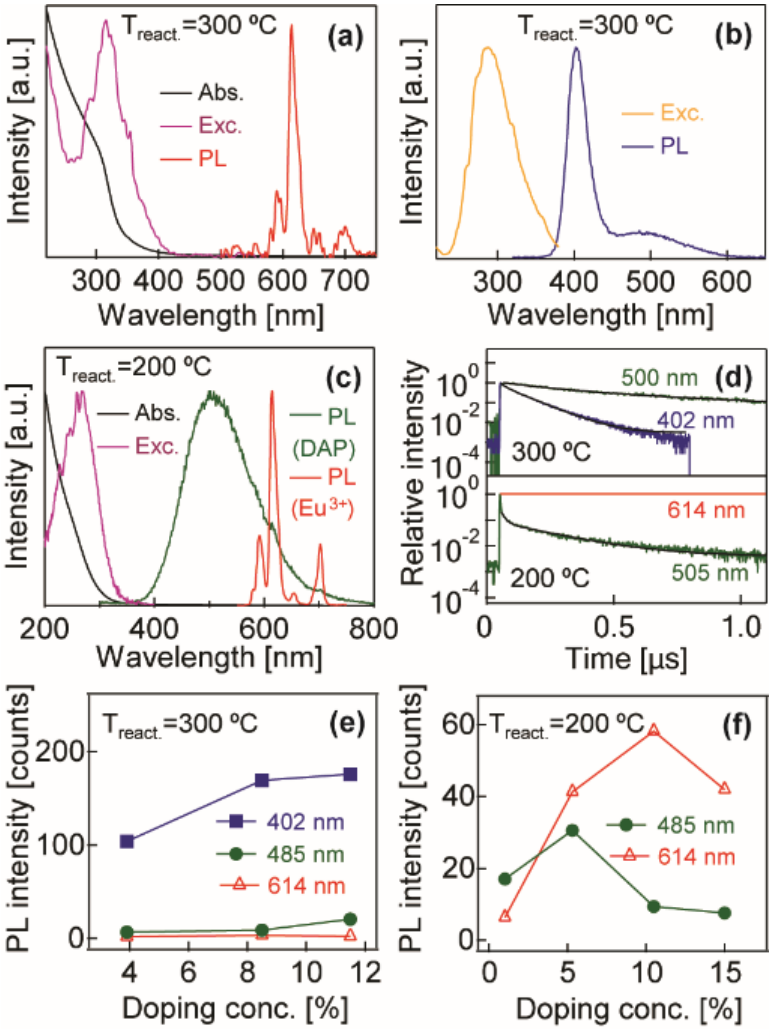

Figure 3.3. (a,b) Excitation and PL spectra of 3.9 % Eu-doped *bcc*-In_2O_3 NCs synthesized at 300 °C: (a) Eu^{3+} and (b) Eu^{2+}. (c) Excitation and PL spectra of 5.3 % Eu-doped *rh*-In_2O_3 NCs synthesized at 200 °C. Eu^{3+} spectra are collected with 0.1 ms delay. (d) Time-resolved PL decay of typical Eu-doped In_2O_3 NCs synthesized at 300 °C (top) and 200 °C (bottom) monitored at different wavelength. (e,f) PL intensity at different wavelengths as a function of the doping concentration for NCs synthesized (e) 300 °C and (f) 200 °C.

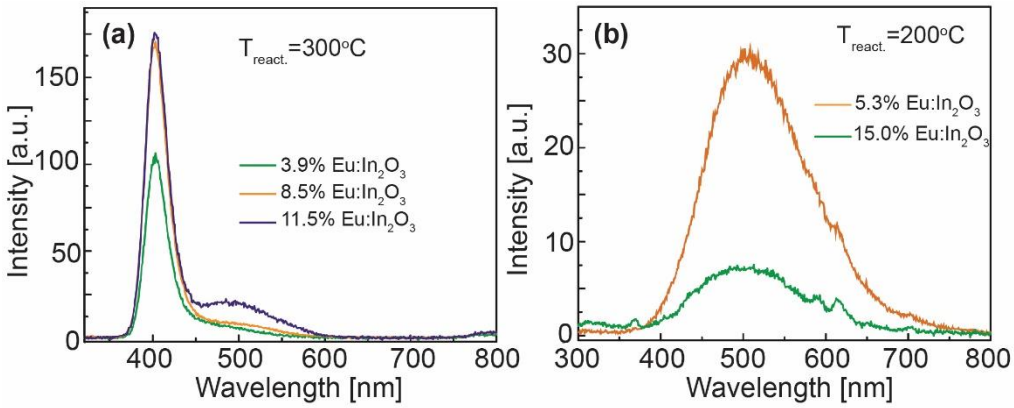

Figure 3.4. (a) PL spectra of Eu^{2+} in Eu-doped *bcc*-In_2O_3 NCs synthesized at 300 °C, having different doping concentrations (λ_{exc}= 300 nm). With increasing doping concentration, the broad defect-based band centered at ca. 500 nm increases in intensity. (b) PL spectra of Eu-doped In_2O_3 NCs synthesized at 200 °C upon excitation above the band gap energy. With increasing doping concentration the sharp Eu^{3+} transitions (580-700 nm) become more pronounced.

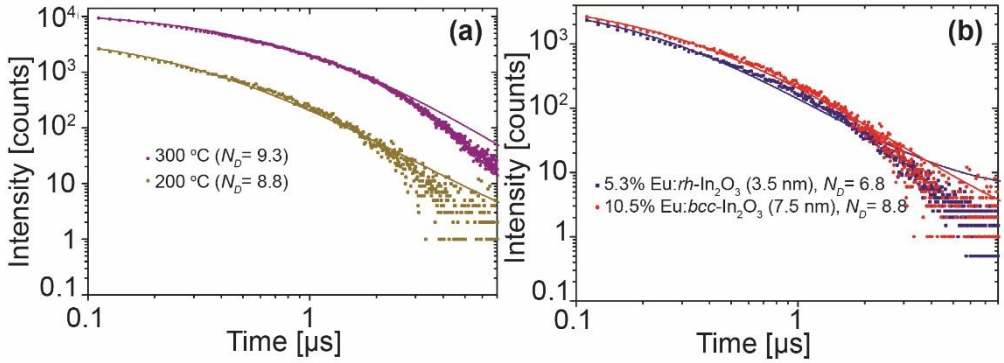

Figure 3.5. (a) Time-resolved DAP PL decay of 10.5 % Eu-doped In_2O_3 NCs synthesized at 200 °C having an average size of ca. 7.5 nm (ocher dots), and 11.4 % Eu-doped In_2O_3 NCs synthesized at 300 °C having an average size of ca. 20.0 nm (purple dots). Although the absolute number of donor defects is similar the defect concentration is significantly higher in smaller NCs. Since both samples have *bcc*-In_2O_3 crystal structure and comparable doping concentration, higher defect concentration (or smaller defect separation) arises from the lower synthesis temperature and higher surface-to-volume ratio of NCs synthesized at 200 °C. (b) Time-resolved DAP PL decay of 5.3 % Eu-doped *rh*-In_2O_3 NCs having an average size of ca. 3.5 nm (blue dots), and 10.5 % Eu-doped *bcc*-In_2O_3 NCs having an average size of ca. 7.5 nm (red dots) synthesized at 200 °C. The defect concentration is more than 7

times higher in *rh*-In_2O_3 NCs. Higher propensity of defect formation in *rh*-In_2O_3 NCs is mostly associated with smaller NC size and higher surface-to-volume ratio. The solid lines represent the fits to the experimental data using DAP time decay model.[54] The number of donor defects N_D (oxygen vacancies) per NC, obtained as a fitting parameter, is shown in the graph.

3.2.3 Determination of Eu^{3+} and Eu^{2+} Concentration; X-ray Absorption Spectroscopy

To determine the ratio of Eu^{3+} and Eu^{2+} in In_2O_3 NCs, the Eu M-edge X-ray absorption data in the framework of the multiplet calculations was analyzed (see section 2.6 and 2.7 for details). Figure 3.6a shows the calculated spectra of Eu^{2+} (top) and Eu^{3+} (bottom). The main M_5-edge peak for Eu^{3+} lies at higher energy than that for Eu^{2+} allowing for a differentiation between the two oxidation states. The relative fractions of Eu^{2+} and Eu^{3+} in *bcc*-In_2O_3 NCs for different doping concentrations were estimated using the linear combination of the theoretical spectra (Figure 3.6b). For 5% doping concentration (Figure 3.6b, top panel), the contributions of Eu^{2+} and Eu^{3+} are nearly equivalent. The fraction of Eu^{2+} only slightly decreases with increasing doping concentration (Figure 3.6b, bottom panel). Despite a significant amount of Eu^{3+} in *bcc*-In_2O_3 NCs its PL intensity is very low, suggesting a weak sensitization by the NC lattice. This result is consistent with the low concentration of oxygen vacancies in *bcc*-In_2O_3 NCs, which have been suggested to facilitate sensitization of Eu^{3+} by energy transfer.[57] On the other hand, the presence of defects in *rh*-In_2O_3 NCs, evident by the DAP emission, leads to a strong Eu^{3+} sensitization. Although a comparable amount of Eu^{2+} is observed in *bcc*- and *rh*-In_2O_3 NCs (Figure A.2, Appendix A), Eu^{2+} emission in *rh*-In_2O_3 NCs could not be detected together with the DAP PL band. This interesting observation might be due to the overlap of the Eu^{2+} and NC band gap absorption, as well as the spatial distribution of Eu^{2+} dopants. Due to high surface-to-volume ratio defects that attract and stabilize Eu^{2+} ions are located in the immediate vicinity of the NC surfaces. The presence of Eu^{2+} close to or on the NC surfaces could lead to non-radiative quenching of their PL. Other types of surface defects characteristic for oxide NCs (i.e. hydroxyl group) could also form donor states and participate in DAP recombination.

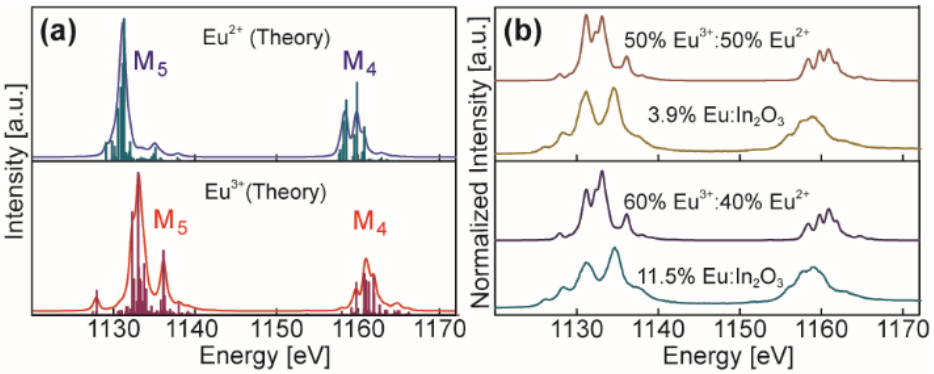

Figure 3.6. (a) Calculated Eu M-edge X-ray absorption spectra of Eu^{2+} (top) and Eu^{3+} (bottom). (b) Comparison of the experimental spectra of 3.9 % (top) and 11.5 % (bottom) Eu-doped *bcc*-In_2O_3 NCs with the linear combination of the calculated spectra.

3.2.4 Europium Site Occupancy

In spite of the high intensity and valence electron participation in Eu^{2+} $4f^65d^1 \rightarrow 4f^7$ transition, broadening and structurelessness of the PL band often hampers the elucidation of Eu^{2+} coordination. In contrast, the splitting of the sharp $^5D_0 \rightarrow {}^7F_J$ transitions in Eu^{3+} can be used to infer the dopant environment. Figure 3.7a compares the high-resolution PL spectra of Eu^{3+} in In_2O_3 NCs synthesized and treated at different temperatures. The spectrum of a sample prepared at 300 ºC (middle) is significantly more resolved than that for NCs synthesized at 200 ºC (top). This difference suggests a more homogeneous dopant environment in *bcc*-In_2O_3 NCs grown at higher temperatures, which arises from lower concentration of defects and/or lower NC surface area. Annealing of the samples synthesized at 300 ºC (bottom) leads to expulsion of the dopants and broadening of the $^5D_0 \rightarrow {}^7F_J$ peaks. The resulting spectrum resembles that in the top panel, confirming that Eu^{3+} ions partly reside on NC surfaces. This conclusion was reinforced by comparing the PL spectra of the NCs that were subjected to a different degree of treatment with TOPO (Figure A.3, Appendix A), which leads to the removal the surface-bound dopant ions. The lowest lying $^5D_0 \rightarrow {}^7F_0$ transition shown in Figure 3.7b is particularly instructive for identifying different Eu^{3+} sites. Owing to non-degenerate ground and excited states, each $^5D_0 \rightarrow {}^7F_0$ peak corresponds to a specific Eu^{3+} site. The spectrum for NCs prepared at 200 ºC features two well-defined peaks at ca. 580.3 nm and 581.5 nm (blue). The peak at 580.3 nm has been associated with surface-bound Eu^{3+} ions, and it decreases in upon repeated TOPO treatment (Figure A.4, Appendix A). The peak at 581.5 nm is proposed to be due to internally incorporated

Eu^{3+}.[56] The spectrum of 300 ºC synthesized NCs has an additional peak at ca. 582.7 nm. Unlike *rh*-In_2O_3, *bcc*-phase has two types of substitutional sites b-site having the C_{3i} (or S_6), and d-site having the C_2 point group symmetry. Given the similarity of the b-site with the substitutional site in *rh*-In_2O_3 (C_{3v}) it is likely that the peak at 582.7 nm corresponds to the d-site in *bcc*-In_2O_3 NCs. It has been suggested that the b-site occupancy is favorable for dopant ions larger than In^{3+}.[161] It is likely that the b-site is occupied first, followed by the d-site at higher doping levels. In addition to the number of peaks for $^5D_0 \rightarrow {}^7F_0$, the ratio of $^5D_0 \rightarrow {}^7F_2$ and $^5D_0 \rightarrow {}^7F_1$ peak intensities (R) contains important information about the Eu^{3+} site symmetry. The R-value increases with decreasing coordination symmetry. It has been suggested in cases of Eu^{3+} doped in Ga_2O_3 and TiO_2 NCs that the R-value for surface-bound Eu^{3+} is lower than that for internally incorporated Eu^{3+},[56,81] owing to the distortion of the substitutional sites. The dependence of R on the overall doping concentration is shown in Figure 3.7c; it initially increases, reaching the maximum for ca. 2 % doping, followed by a gradual decrease. This behavior is similar to that of Eu^{3+} in Ga_2O_3 NCs, indicating that Eu^{3+} incorporation is slower than the rate of NC growth. As the starting amount of Eu^{3+} increases, a larger number of Eu^{3+} can be incorporated into the NCs, until the occupation of internal substitutional sites reaches maximum.

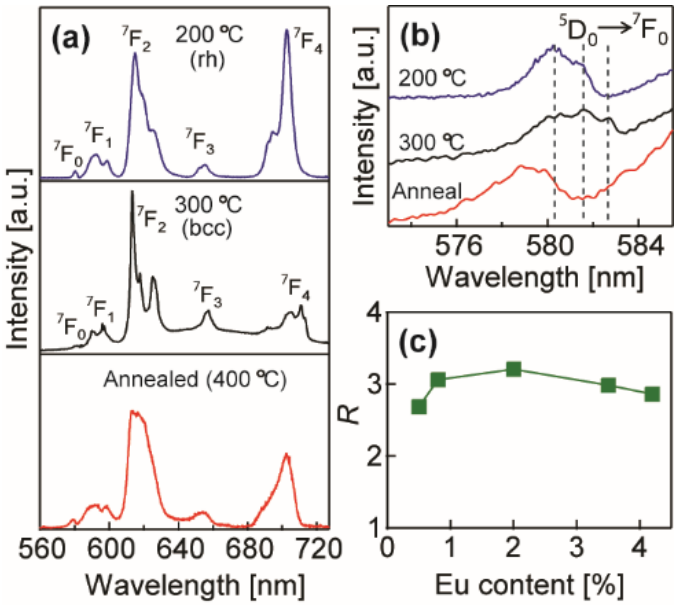

Figure 3.7. (a) High-resolution Eu^{3+} PL spectra of Eu-doped *rh*-In_2O_3 NCs synthesized at 200 °C (top), and *bcc*-In_2O_3 NCs synthesized at 300 °C before (middle) and upon annealing at 400 °C (bottom). (b) Eu^{3+} ($^5D_0 \rightarrow {}^7F_0$) spectra of samples in (a). (c) R-value as a function of the doping concentration for Eu-doped *bcc*-In_2O_3 NCs synthesized at 300 °C.

3.3 Conclusions

In summary, the effect of NC phase and Eu oxidation state on the PL properties of colloidal Eu-doped In_2O_3 NCs were demonstrated. Blue (Eu^{2+}) or red (Eu^{3+}) emission in both *bcc*- and *rh*-In_2O_3 NCs, owing to the controlled interactions of dopant ions with the host lattice defect sites, were achieved. The NC size and structure, and dopant oxidation state are effective tools for controlling the native defects in In_2O_3 NCs. Using different means to control defect concentration, interdependence of the defect formation, and dopant incorporation and emission was demonstrated. The incorporation Eu^{2+} ions leads to stabilization of oxygen vacancies, which in turn act as sensitizers for the Eu^{3+} emission. The ability to simultaneously control the NC structure and oxidation state of lanthanide dopants in NCs allows for controlling optical properties or inducing multifunctionality in colloidal NCs.

Chapter 4
Turning Non-Luminescent Metal Oxide Nanocrystals into Tunable Materials with High Scotopic to Photopic Ratio

4.1 Overview

Aliovalent doping of metal oxide nanocrystals is an attractive way to tailor their electronic structure and manipulate their optoelectronic properties. Incorporation of such extrinsic defects generates new electronic states within the band gap, which can trap photoexcited electrons and holes, acting as radiative recombination centers. Herein, the synthesis of ternary gallium tin oxide nanocrystals throughout the full composition range is reported. It is demonstrated that their photoluminescence can be tuned through most of the visible region by changing Ga:Sn ratio. By substitutional doping with Ga^{3+}, the PL intensity of SnO_2 nanocrystals is enhanced by nearly three orders of magnitude, reaching photoluminescence quantum yield of > 40%. Increase in PL intensity is attributed to the formation of donor and acceptor pairs, and the increase in emission energy is discussed in the context of band gap expansion and stronger Coulomb interaction between charged defect sites. Time-resolved and steady-state photoluminescence spectroscopies reveal that the interaction of extrinsic and native defects is driven by the nature of the dopant ion. By adjusting various reaction conditions, the nanocrystals with nearly ideal scotopic to photopic ratio and a quantum yield of ca. 34% were prepared, attesting to the potential of these nanocrystals as light sources for general lighting applications. The results of this work provide new insight into the role of defect chemistry in tailoring the optoelectronic properties of transparent metal oxide nanocrystals, and pave the way for the rational design of light sources and photonic devices with high photoluminescence efficiency, minimum toxicity, and optimal lighting characteristics.

4.2 Results and Discussion

4.2.1 Structural Characterization

First, the structure and composition GTO NCs synthesized under different conditions were examined. XRD patterns of GTO NCs prepared with different starting concentrations of Ga^{3+} precursor for the reaction duration of 8 h are presented in Figure 4.1a. The patterns of pure SnO_2 and Ga_2O_3 NCs agree well with the pattern of bulk rutile tin oxide (JCPDS 088-0287, red sticks) and γ-phase gallium oxide (JCPDS 020-0426, blue sticks), respectively. With increasing content of substitutional Ga^{3+} in SnO_2 NCs, the rutile XRD peaks shift to higher angles (Figure B.1 in Appendix B), which is consistent with the smaller ionic radius of octahedrally coordinated Ga^{3+} (0.62 Å) compared to Sn^{4+} (0.69 Å). Increasing the gallium concentration is accompanied by a decrease in NC size (Table B.1 and Figure B.2 in Appendix B). The NCs retain rutile structure until the Ga:Sn ratio becomes 50:50, suggesting that SnO_2 NCs have high capacity to dissolve foreign ions to form a solid solution. The NC structure transforms to γ-Ga_2O_3 when Ga:Sn precursor ratio exceeds 75:25. The broadening of the XRD peaks for undoped SnO_2 and Ga_2O_3 NCs is associated their small size. An increase in the concentration of dopant impurity (Ga^{3+} in SnO_2 and Sn^{4+} in Ga_2O_3) causes an increase in the local disorder of the NC host lattice, leading to an increased full width at half maximum (fwhm) for both host lattices. On the other hand, the XRD peaks become narrower by increasing the reaction duration (Figure 4.1b) or temperature (Figure 4.1c), for the same ratio of Ga:Sn (50:50), suggesting the improvement in the crystalline order of GTO NCs. It is also evident that the peak at ca. 35 degrees for rutile GTO NCs has the smallest fwhm, suggesting the anisotropic morphology of SnO_2 NCs, and the longest dimension along {101} plane.[27]

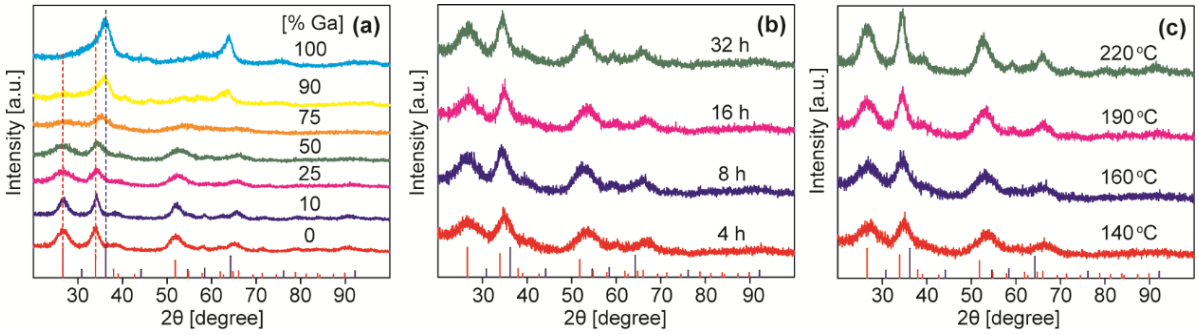

Figure 4.1. (a) XRD patterns of GTO NCs with different Ga content (in atom %), as indicated in the graph. (b) XRD patterns of GTO NCs with 50 % Ga content, synthesized for different reaction

duration (4, 8, 16, and 32 hours). (c) XRD patterns of GTO NCs with 50 % Ga content, synthesized for 8 h at different temperatures, as shown the graph. Red and blue sticks in all panels represent the patterns of bulk rutile SnO_2 and γ-Ga_2O_3, respectively.

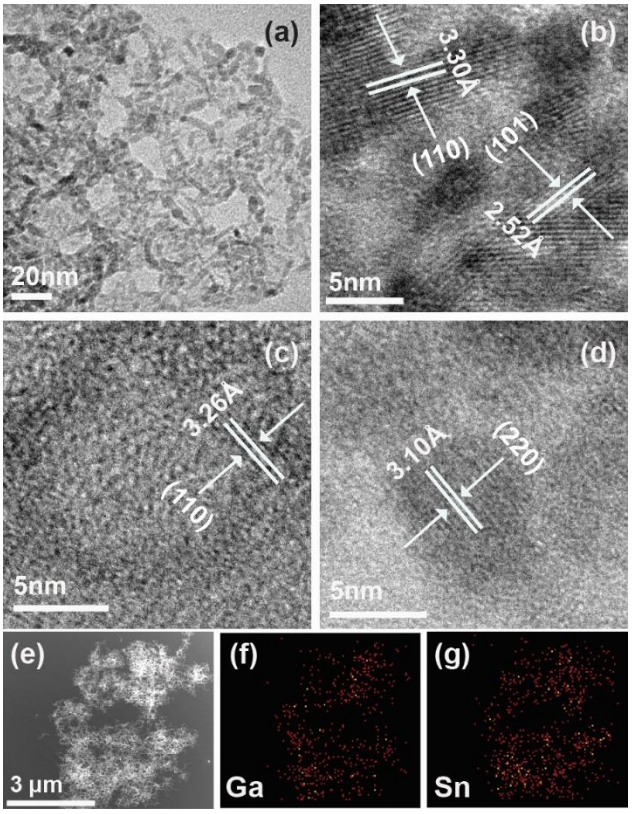

Figure 4.2. (a-d) TEM images of GTO NCs synthesized under the same conditions, but with different Ga contents: (a, b) 10 % Ga, (c) 50 % Ga, and (c) 90 % Ga. The measured average lattice spacing corresponds to rutile SnO_2 (b, c), and γ-Ga_2O_3 (d). (e-g) Scanning transmission electron microscopy (STEM) image (e) and the corresponding elemental mapping for Ga (f) and Sn (g) of GTO NCs containing 50 % Ga synthesized for 32 h.

TEM images of GTO NCs, synthesized with different Ga^{3+} precursor concentrations for 8 h reaction duration are shown in Figure 4.2. At low Ga concentration (≤ 25%), the NCs have elongated morphology and high crystallinity, as evident in Figure 4.2a and b, respectively. Increasing Ga content induces the lattice disorder and adversely affects the crystallinity of the SnO_2 NCs (Figure 4.1c). The measured average lattice spacing for {110} planes in GTO NCs for Ga content of ≤ 50% is smaller than that for SnO_2 NCs (3.35 Å) owing to the substitutional incorporation of Ga^{3+} in the NC

lattice, and is consistent with XRD patterns in Figure 4.1a. The morphology of the NCs becomes spherical for high Ga content (90%), and the measured lattice spacing reflects the transformation to γ-Ga_2O_3 crystal structure (Figure 4.2d). The actual Sn and Ga concentrations, determined by EDX spectroscopy, reveals that Sn tends to be incorporated in the lattice more readily than Ga for all starting precursor ratios (Table B.2 in Appendix B). The spatial distribution of Ga and Sn in NCs was assessed by EDX elemental mapping (Figure 4.2e-g). Similar maps for both Ga and Sn (Figure 4.2f and g, respectively) suggest the lack phase segregation, and the formation of the corresponding oxides. To understand the origin of the elongated morphology of rutile GTO NCs, the NC shape evolution with respect to the reaction time was examined. Overview and high resolution TEM images of GTO NCs prepared for varied reaction times are shown in Figure B.3 (Appendix B). At shorter reaction times the isolated NCs are largely spherical. As the reaction continues, these NCs undergo oriented attachment, assembling into nanowires with <101> orientation,[26,27] consistent with narrowing of fwhm of the corresponding XRD peak (Figure 4.1b). No significant change in the concentration of Ga was observed at longer reaction times. Performing the reaction at higher temperature also elongates the particles (Figure B.4 in Appendix B), although it is accompanied by the exclusion of Ga, as indicated in Table B.2 (Appendix B).

4.2.2 Investigation of Composition Impact on Band Gap and PL Tunability

Our group has previously shown that colloidal γ-Ga_2O_3 NCs do not exhibit quantum confinement in the size range achievable by colloidal synthesis,[11,55] rendering their band gap energy independent of the NC size. However, because of the considerable difference between the band gap of SnO_2 and γ-Ga_2O_3, the optical band gap of GTO NCs is strongly dependent on their composition. As evident from Figure 4.3a, the onset of the band edge absorption of GTO NCs shifts continuously to lower energy with decreasing Ga content up to band edge absorption for pure SnO_2 NCs. In contrast to Ga_2O_3, the Bohr radius of SnO_2 (2.7 nm) is comparable to an average size of hydrothermally-synthesized SnO_2 NCs, at least in one dimension, causing a blue shift of their band edge absorption relative to bulk SnO_2. It is widely accepted that oxygen vacancies are common structural defects in different metal oxides. In SnO_2 these point defects form donor states ca. 0.15-0.3 eV below the CBM, delivering both high n-type electrical conductivity and transparency to the visible region of the spectrum.[37] On the other hand, aliovalent doping of SnO_2 with cations having lower oxidation state than 4+, induces acceptor centers within the bandgap. Theoretical calculations have suggested low formation energy of acceptors and high binding energy between acceptors and donors (oxygen vacancies), resulting in

formation of donor-acceptor complexes.[38,162,163] Following the excitation of rutile-phase GTO NCs into the bandgap, the electrons and holes are trapped in the donor and acceptors states, respectively, which then act as radiative recombination centers. Similar mechanism has been suggested for γ-Ga_2O_3 NCs, involving oxygen vacancy and gallium-oxygen vacancy pair as donor and acceptor sites, respectively.[10,11,51,53]

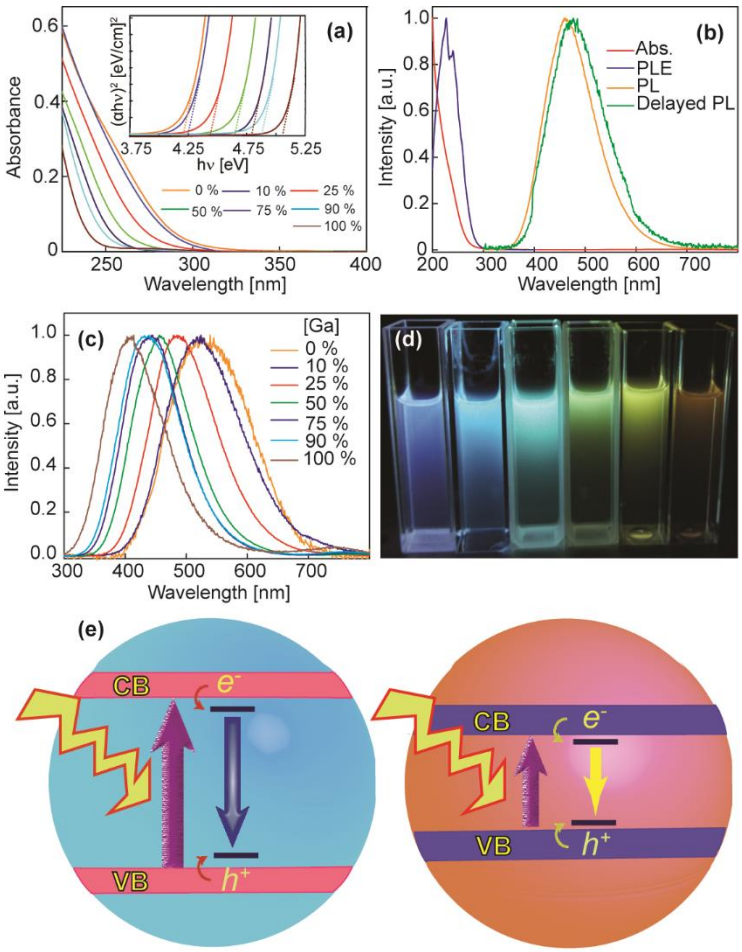

Figure 4.3. (a) Absorption spectra of GTO NCs with different Ga content, as indicated in the graph. The numbers in the legend represent Ga concentration (in atom %). (b) Excitation (blue trace) and PL (steady-state, orange trace; delayed, green trace) spectra of GTO NCs with 50% Ga content. Absorption spectrum (red trace) is shown for comparison. (c) PL spectra of GTO NCs with different Ga content. (d) Photograph of the emission of colloidal GTO NCs with various Ga content. (e) Schematic illustration of the alteration of sub-band gap states due to the change in the band gap width. The photoexcited electrons and holes are trapped in donor and acceptor states, located below

CB and above VB, respectively. Radiative recombination of the carriers in GTO NCs with smaller band gap (low Ga content) is responsible for yellow-orange emission (right). Increased Ga content results in band gap widening and increased energy separation between donor and acceptor levels, causing the blue emission (left).

Large energy separation between excitation (Figure 4.3b, blue trace) and emission (Figure 4.3b, orange trace) bands for all GTO NCs is consistent with PL originating from localized intra-band-gap states. Neglecting the lattice phonon effects, the energy of the DAP emission (E_{DAP}) can be described by the following equation.

$$E_{DAP} = E_g - (E_D + E_A) + \frac{e^2}{4\pi\varepsilon r} \tag{4.1}$$

where E_g is the band gap energy, E_D and E_A are donor and acceptor binding energies, respectively, and r is the donor-acceptor separation. The last term in Eq. 4.1 represents the Coulomb interaction between singly-charged donor and acceptor sites, which has been shown to be the determining parameter of the DAP emission energy dependence on the NC size.[10] Increasing the average donor-acceptor separation with increasing NC size leads to a red shift of the DAP PL band. The range of separations between donor and acceptor sites within a NC is also responsible for a red shift of the delayed emission relative to the steady-state PL spectrum (*vide infra*), as shown in Figure 4.3b (green trace).[11,55] However, the dependence of the DAP emission energy on the NC composition is mostly due to the change in the electronic structure. The DAP band follows the blue shift of the band edge absorption with increasing Ga content (Figure 4.3c). The increase in E_g has a larger effect on E_{DAP} than the decreased average separation between donor and acceptor sites caused by Ga doping (Figure 4.3e). The ability to manipulate the difference in energy between donor and acceptor states in GTO NCs by composition control allows for an expansion of the PL tuning range throughout the entire visible part of the spectrum. Photograph of the light emission of colloidal GTO NCs having different Ga content is shown in Figure 4.3d, attesting to their potential for photonic, optoelectronic, and biomedical applications.

4.2.3 Defect Concentration Determines the PLQY

The separation between donor and acceptor sites also determines the decay dynamics of the DAP emission.[54,164] The rate determining step in the DAP recombination is a tunnel transfer of the electron

trapped in the localized donor state to the associated acceptor site where the charge carriers recombine. The electron and hole trapped in the nearest donor and acceptor site, respectively, have the highest probability of recombining first.[164] More distant donor-acceptor pairs recombine subsequently, causing a red shift and a delay in the observed emission (see Figure 4.3b). Typical time-resolved PL data of GTO NCs containing different concentrations of gallium are shown in Figure 4.4a. The average DAP recombination lifetime shortens with increasing Ga:Sn ratio in rutile-phase GTO NCs (i.e., Ga% ≤ 50), which is consistent with the reduction in the DAP separation owing to an increased density of donor-acceptor pairs. In principle, the highest density of the defect-based recombination sites is formed for the maximum concentration of aliovalent dopants. The closest associated donor-acceptor pairs will recombine with the highest efficiency, suggesting the possibility of increasing PLQY by substitutional incorporation of aliovalent dopants. Figure 4.4b compares the PLQY of GTO NCs having different composition. The quantum efficiency increases with increasing Ga content, and reaches the maximum value at ca. 50 % Ga^{3+}. Further increase in Ga:Sn ratio leads to diminished PLQY, concomitantly with a structural transformation to cubic γ-Ga_2O_3 phase and decreasing doping level of Sn^{4+}. The results of Figure 4.4b confirmed our hypothesis that higher concentration of aliovalent dopants induces smaller average separation of donor-acceptor pairs resulting in more efficient radiative recombination. This is in contrast with isovalent doping (i.e., In^{3+} in Ga_2O_3 NCs), which leads to significant reduction in PL efficiency.[1] The highest measured PLQY for GTO NCs is ca. 45 %, which is one of the highest values reported for defect-based emission in oxides.

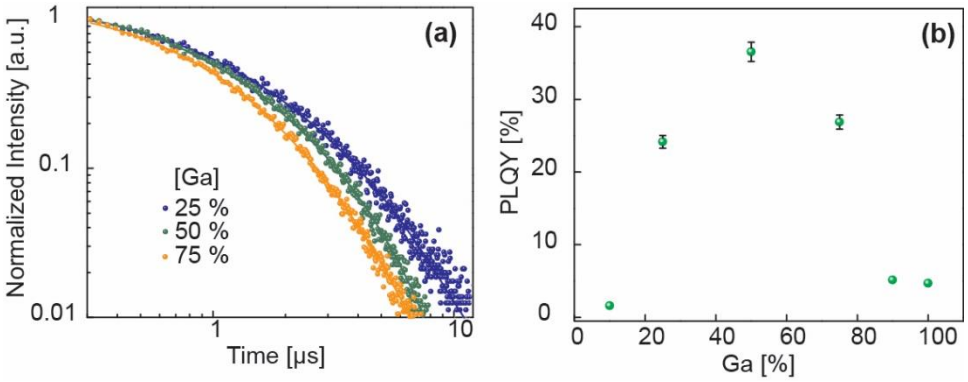

Figure 4.4. (a) Time-resolved PL decay of selected GTO NCs. The Ga content corresponding to each sample is shown in the graph. The PL lifetime data for other samples were left out for clarity. (b) PLQY of GTO NCs with different Ga concentration.

4.2.4 The Influence of Reaction Length on Optical Properties

To probe the impact of the reaction duration on the optical properties of GTO NCs, NCs with 50% Ga content by varying the reaction time between 4 and 32 hours were synthesized. The EDX measurements confirmed that the composition did not change with prolonging the reaction time (Table B.2 in Appendix B). However, as the reaction time increases, the NCs continue to grow and their band edge shifts to lower energy due to quantum confinement of SnO_2 NC host lattice (Figure 4.5a). The prolonged growth of NCs also leads to a small decrease in donor/acceptor defect density and an increase in their average separation, causing minor but detectable red shift of the DAP emission band (Figure 4.5b). Surprisingly, the PLQY is enhanced from ca. 25 % to 43 % by increasing the reaction duration from 4 h to 32 h (Figure 4.5d, green symbols).

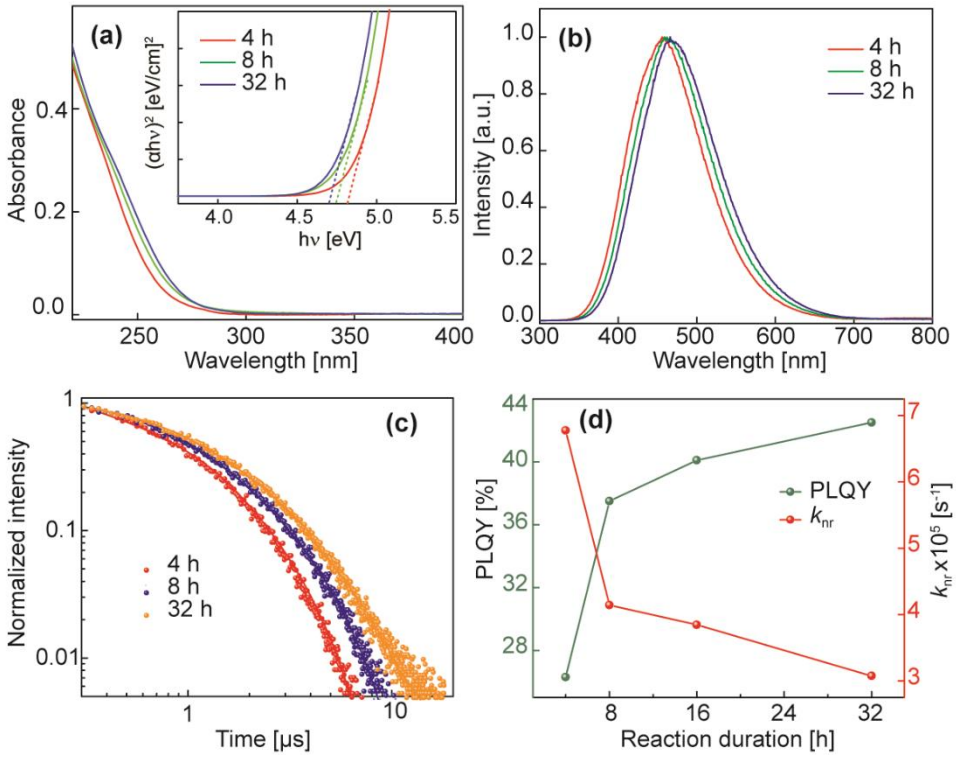

Figure 4.5. (a) Absorption spectra of GTO NCs with 50 % Ga content, synthesized for varied lengths of time, as indicated in the inset. (b) PL spectra of GTO NCs in (a). (c) Time-resolved PL decay of GTO NCs in (a). (d) PLQY and non-radiative recombination rate constant for GTO NCs as a function of reaction duration.

A decrease in the PL decay rate with increasing reaction time (Figure 4.5c) is consistent with a larger average donor-acceptor separation, although it is evident that the change in the PL decay rate is much more significant than the shift in the steady-state emission band. The overall lattice disorder, stemming from heavy doping, concurrently leads to the formation of non-radiative recombination centers. The improvement in the long-range lattice order, caused by lengthening the reaction time, stimulate the radiative recombination pathway and therefore enhance the PL efficiency. Radiative (k_r) and non-radiative (k_{nr}) recombination rates were estimated utilizing the following equations:

$$\tau = \frac{1}{(k_r + k_{nr})} \tag{4.2}$$

$$Q_x = \frac{k_r}{(k_r + k_{nr})} \tag{4.3}$$

where τ and Q_x are the average PL lifetime and quantum yield, respectively. Using the average lifetimes determined form the exponential fitting of the data in Figure 4.5c (see Table B.3 in Appendix B) and the corresponding relative PLQYs, k_r and k_{nr} for different synthesis times were calculated. Figure 4.5d plots the non-radiative recombination rate (red circles) and PLQY (green circles) with respect to the reaction duration. With extended reaction time radiative contribution to the PL decay increases, while non-radiative contribution decreases. A decrease in k_{nr} is accompanied by a symmetric increase in PLQY, highlighting the utility of hydrothermal synthesis and aliovalent alloying in tailoring the electronic structure and optical properties of metal oxide nanostructures.

4.2.5 Exploring the Role of Temperature on Modulating the Electronic Structure

To investigate the effect of the synthesis temperature on the efficiency of the GTO NC emission, the NC syntheses were performed at different temperatures between 140 ^{o}C and 220 ^{o}C, keeping the other parameters unchanged. The increase in the synthesis temperature leads to the improvement in the sample crystallinity (see Figure 4.1c and the associated discussion). However, the Ga content drops from 43 % (for 140 ^{o}C synthesized NCs) to 28 % (for 220 ^{o}C synthesized NCs), as shown in Table B.2 (Appendix B). Lower Ga concentration and larger NC sizes are both responsible for the red shift of the band gap absorption (Figure 4.6a) and DAP PL band (Figure 4.6b) with increasing temperature. Similar to reaction time dependence in Figure 4.5, the influence of temperature on the lifetime and PLQY must be discussed in the context of the competition between the crystallinity and DAP concentration of the NCs. On one hand, the NC treatment at elevated temperatures in solution

diminished the fast nonradiative recombination pathway, leading to an increase in the DAP PL lifetime and PLQY. On the other hand, it reduces the concentration of radiative centers by removing Ga^{3+}-induced defects, leading to a decrease in in PL efficiency. As depicted in Figure 4.6d, while k_r experiences relatively little change over the investigated temperature range, k_{nr} drops sharply when the temperature is raised from 140 °C to 190 °C, followed by a slight upward turn at higher temperatures. PLQY at first increases with increasing reaction temperature and then significantly declines (Figure 4.6d, green spheres). The maximum PLQY is achieved for the reaction temperature of ca. 190 °C due to the optimal balance between DAP concentration and long-range structural order.

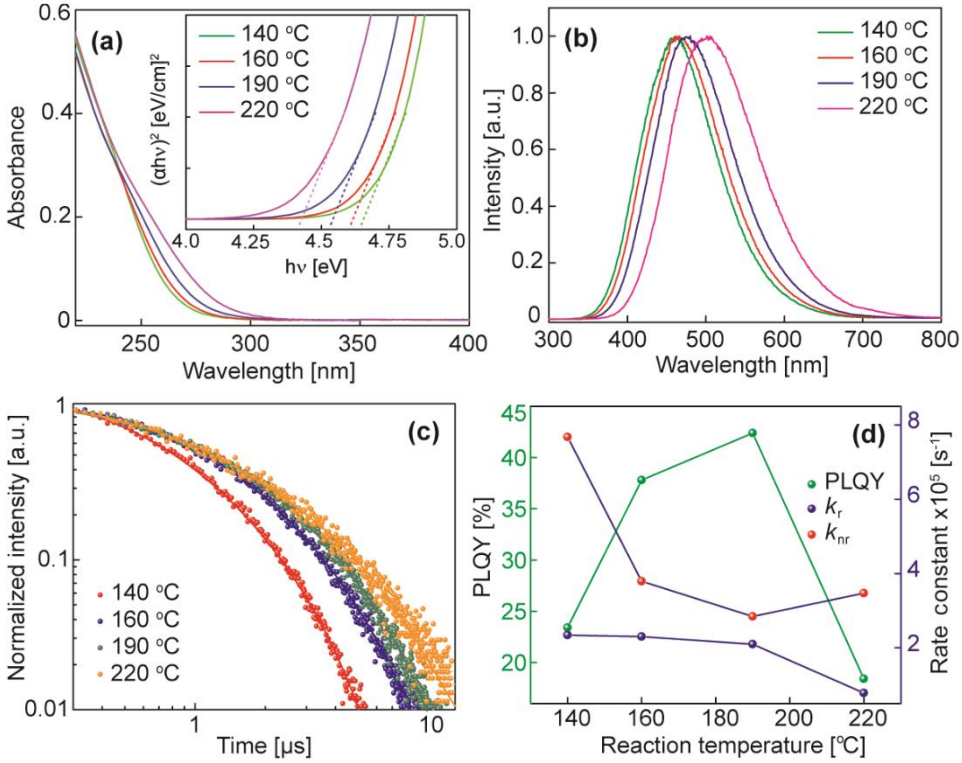

Figure 4.6. (a) Absorption spectra of GTO NCs with 50 % Ga content, synthesized in ethanol at different temperatures, as indicated in the inset. (b) PL spectra of GTO NCs in (a). (c) Time-resolved PL decay of GTO NCs in (a). (d) PLQY and electron-hole recombination rate constants (radiative and non-radiative) for GTO NCs as a function of reaction duration.

4.2.6 Toward Functional Properties of GTO NCs

The ever-increasing global demand for lighting and the necessity to lower energy consumption have, in recent years, placed an emphasis on finding new ways of improving the efficiency and characteristics of light emitting phosphors and devices. One of the emerging ways to maximize the efficiency of a light source is to design a light emitting material that can most effectively stimulate human eye under particular lighting conditions. Human vision occurs by two primary modes: photopic and scotopic vision. Photopic vision is the vision under well-lit conditions and is primarily enabled by cone cells in the eye. It is responsible for color perception, visual acuity and temporal resolution. Scotopic vision, on the other hand, is vision in dark, which is monochromatic and functions due to rod cells in the eye. A combination of photopic vision and scotopic vision at low lighting levels is known as mesopic vision, and involves a combination of rod and cone cells in the eye. The mesopic luminous efficiency is defined as a linear combination of photopic and scotopic luminosity functions:

$$V_m(\lambda) = (1-x)V'(\lambda) + xV(\lambda) \tag{4.4}$$

where $V(\lambda)$ and $V'(\lambda)$ are is the standard photopic and scotopic luminosity function (Figure 4.7a), respectively, and x is the function of photopic adaptation luminance (L_p). Therefore, the objects are perceived brighter in the dark, when the light source maximum emission is at ca. 505 nm (scotopic function), while in well-lit environment the maximum emission at ca. 555 nm (photopic function) simulates the objects to be identified brighter. Light sources with (high) scotopic to photopic ratio (S/P) of ca. 2.5 are recognized to be visually more efficient. Such light sources can be operated at lower power relative to those with low S/P ratio.[165,166]

The ability to simultaneously manipulate PL properties of GTO NCs, including emission energy, spectral band width, and quantum efficiency, renders GTO NCs promising for designing light sources with optimal S/P ratio. A series of GTO NCs under diverse reaction conditions was prepared (Table B.4 and Figure B.5 in Appendix B), allowing us to generate samples that have a maximum emission wavelength matching those of the maxima of both scotopic (Figure 4.7a) and photopic (Figure B.6 in Appendix B) luminosity functions. The measured PLQY of ca. 34% for S/P = 2.60 is approximately two times greater in efficiency than that reported for CdSe-based QDs with the similar S/P ratio (Figure 4.7a).[165,166] The photograph of the sample emission showing its yellowish-green color under UV excitation is displayed in the inset of Figure 4.7a. To generate white light for lighting

applications, nanoconjugates by functionalizing these NCs with dye molecules emitting in the complementary spectral range were prepared.[42,167] These hybrid organic-inorganic nanostructures act as single nanophosphors owing to the distance-dependent energy transfer between the two moieties. A photograph of a typical white light emitting nanoconjugate sample is also shown in Figure 4.7b (inset). These results serve as an instructive example how the control of the metal oxide NC electronic structure and defect interactions by aliovalent doping/alloying and synthesis methodology can result in improved efficiency and characteristics for lighting and other photonic applications.

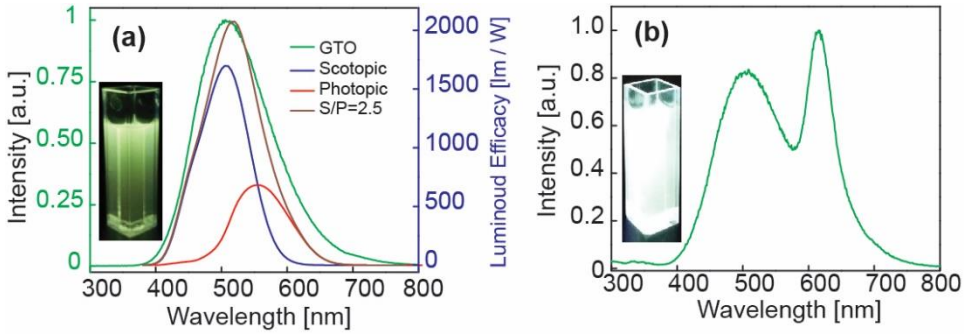

Figure 4.7. (a) PL spectrum of GTO NCs (green trace) covering both scotopic (blue trace) and photopic (red trace) luminosity functions. The function corresponding to S/P ratio of 2.5 is shown as a brown trace. The photograph of the emission of the NCs excited into the band gap is shown in the inset. (b) PL spectrum of GTO NCs in (a) conjugated with Atto-590. The photograph of the emission of the nanoconjugates excited into the band gap is shown in the inset.

4.3 Conclusions

In summary, new ternary gallium tin oxide NCs were synthesized, and it was demonstrated that their PL color can be tuned from blue to orange-red by composition modulation. Substitutional incorporation of group 13 elements into SnO_2 lattice creates acceptor levels within the band gap, simultaneously increasing intrinsic donors ($V_O^{\bullet}$) to compensate for charge imbalance. Using SnO_2 NCs as a model system in which majority of photogenerated carriers tend to recombine non-radiatively, it was shown that induced donor-acceptor pairs introduce a new radiative recombination pathway, resulting in the enhancement of the PLQY to above 40 %. The observed blue shift of the DAP emission of GTO NCs with increasing Ga content originates from widening of the band gap and stronger Coulomb interaction between the donor-acceptor pairs. Systematic increase in the DAP concentration, associated with an increase in Ga^{3+} doping level, leads to smaller separation between

electron and hole trap states, resulting in a faster PL decay rate. Non-radiative recombination mechanisms can be further suppressed by improving the long-range order of NCs through increased reaction duration and temperature. The interaction of the dopant impurity with native defects is a function of its chemistry, and serves as another degree of freedom to control the electronic structure of NCs. Broad PL tunability, chemical stability, and efficiency of these TMO NCs are compelling features for various photonic applications, including the generation of light sources having ideal scotopic/photopic ratio and appreciable PLQY. The results of this work demonstrate the possibility of converting non-luminescent TMO NCs into tunable and efficient light emitters by simultaneous control of the NC composition and defect interactions. This process is enabled by judicious selection of the synthesis method and reaction conditions, and allows for a design of light emitting devices with optical characteristics.

Chapter 5
Anomalous Photocatalytic Activity of Nanocrystalline *γ*-Phase Ga_2O_3 Enabled by Long-Lived Defect Trap States

5.1 Overview

Semiconductor photocatalysis has emerged as an efficient and sustainable advanced oxidation process for wastewater treatment and other environmental remediation, and forms the basis for water splitting and solar-to-fuel conversion. Nanocrystalline metal oxides are particularly promising photocatalysts because of their efficiency, stability, and low toxicity. However, the influence of the crystal structure and defects on the photocatalytic activity of these polymorphic materials is still poorly understood. In this work the structural dependence of the photocatalytic activity of nanocrystalline Ga_2O_3 is investigated. It is demonstrated that metastable cubic-phase γ-Ga_2O_3 prepared from colloidal nanocrystals exhibits an anomalously high photocatalytic activity, which rapidly decreases upon thermally-induced transformation to monoclinic β-Ga_2O_3. Using steady-state and time-resolved photoluminescence measurements, it is shown that the reduction in photocatalytic activity upon annealing is accompanied by a decrease in native defect (i.e., oxygen vacancy) concentration and interactions. Trapping charge carriers in defect-induced states in γ-Ga_2O_3 nanocrystals results in a reduced rate of charge recombination and enhanced interfacial charge transfer, which has been unambiguously confirmed by comparative measurements using In^{3+}-doped Ga_2O_3. These phenomena are enabled by the unique character of defect states in γ-Ga_2O_3 nanocrystals which have much longer lifetime than typical metal oxide surface states. Using various scavengers, it is demonstrated that reactive radicals ($OH^{\bullet}$ and $O_2^{\bullet -}$) formed by photogenerated charge carriers play a key role in the mechanism of photocatalytic degradation by Ga_2O_3. The results of this work demonstrate how manipulation of the location and electronic structure of defect sites in nanostructured metal oxides can be effectively used to control charge carrier separation and enhance photocatalytic activity, without a detriment to high surface-to-volume ratio.

5.2 Results and Discussion

5.2.1 Structural Analysis: *γ/β* Phase Transformation of Ga_2O_3 NCs

Typical XRD patterns of Ga_2O_3 NCs annealed at various temperatures from 400 °C to 800 °C for 2 hours are presented in Figure 5.1a and Figure C.1 (Appendix C). The XRD pattern of as-synthesized Ga_2O_3 NCs (Figure 5.1a, blue trace) is well matched with that of bulk γ-Ga_2O_3 (blue sticks, JCPDS 20-0426). Significant broadening of the peaks is consistent with small average NC size. The XRD patterns show no evidence of a significant increase in size of γ-phase NCs upon annealing up to ca. 550 °C. However, between 550 °C and 575 °C the narrower XRD peaks characteristic β-Ga_2O_3 (red sticks, JCPDS 41-1103) appear (Figure 5.1b). The presence of mixed phase is clearly observed in the XRD pattern of 600 °C annealed samples (Figure 5.1a, orange trace), and is particularly evident between 25° and 40° where the sharp peaks belong to β-phase while the broad peaks belong to γ-phase (Figure 5.2). The samples annealed at or above 700 °C (red trace in Figure 5.1a, and purple trace in Figure 5.1b) exhibit monoclinic β-phase crystal structure, and much larger crystalline domains. Unlike γ -Ga_2O_3, the average domain size of β-Ga_2O_3 increases gradually with an increase in annealing temperature. These results indicate that NC phase is sensitive to annealing temperature, and that phase transformation from γ-Ga_2O_3 to β-Ga_2O_3 is accompanied by a rapid increase in the NC size. Our group has previously demonstrated that *in situ* phase transformation of In_2O_3 NCs can be controlled by controlling NC size and growth kinetics, where surface energy and surface stress lead to stabilization of the metastable phase below the critical size.[8,19] It has also been suggested that this process occurs *via* surface or interface nucleation mechanism depending on the reaction conditions.[7,8] The results in Figure 5.1a demonstrate the generality of these findings, and suggest that phase transformation occurs when temperature-induced NC fusion causes the increase in the size of nanocrystalline grains above ca. 6 nm.

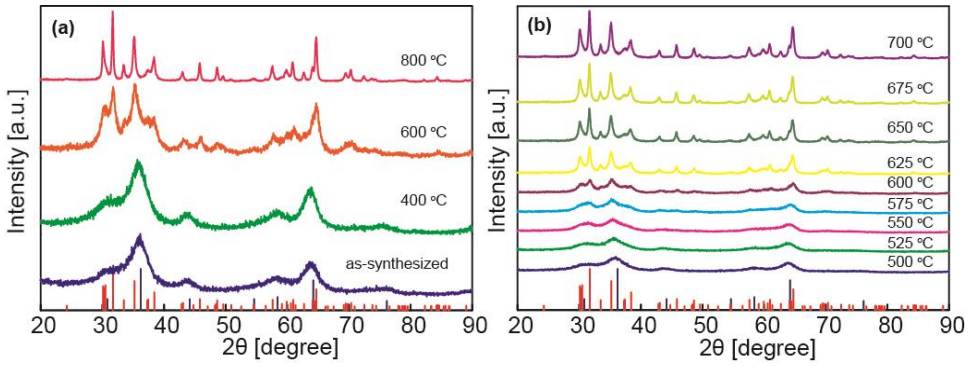

Figure 5.1. (a) XRD patterns of Ga_2O_3 NCs synthesized at 200 ºC and annealed at different temperatures as indicated in the graph. (b) XRD patterns of Ga_2O_3 NCs annealed at different temperatures in the range near the phase transformation from γ-phase to β-phase. Blue and red sticks represent the patterns of bulk γ-Ga_2O_3 and β-Ga_2O_3, respectively.

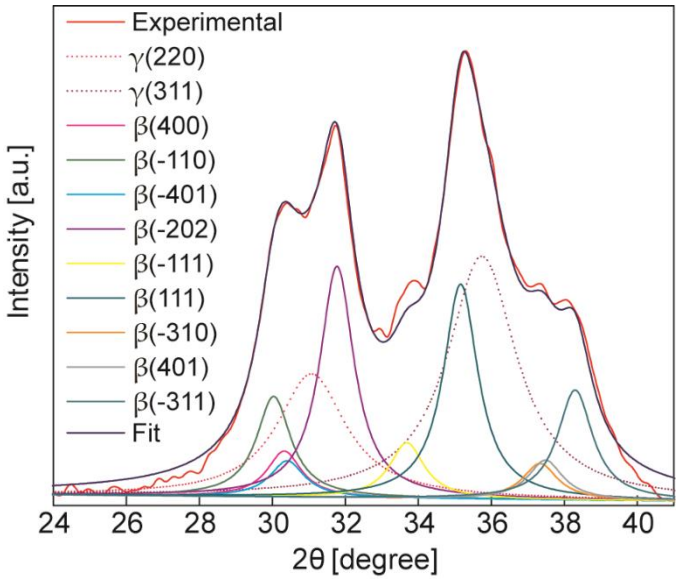

Figure 5.2. Deconvolution of the XRD peaks for Ga_2O_3 NCs synthesized at 200 ºC and annealed at 600 ºC. The presence of both β- and γ-phase is clearly observed between 25° and 40°, and specific peaks for both phases are designated in the graph.

Typical TEM images of the samples in Figure 5.1 are shown in Figure 5.3. Figure 5.3a shows an overview image of the NCs annealed at 400 °C. Annealing at lower temperatures causes the aggregation of NCs, creating a porous structure. This aggregation is evident in all samples that contain γ-phase (Figure C.2 in Appendix C). Figure 5.3b shows a high resolution TEM image of

Ga_2O_3 NCs in Figure 5.3a. The measured average lattice spacing of 2.90 Å corresponds to {220} plane of γ-Ga_2O_3, consistent with the XRD data. The boundaries between individual NCs remain clearly observable, suggesting that annealing does not lead to a fusion of NCs and the formation of larger single crystal domains, but rather an aggregation of individual NCs. This observation is also in accordance with XRD results discussed above. Figure 5.3c and d shows high resolution TEM images of the samples annealed at 600 °C and 950 °C, respectively. For the samples annealed at 600 °C the lattice spacing indicates the presence of both γ-Ga_2O_3 and β-Ga_2O_3. This conclusion also agrees with the results in Figure 5.1. The inspection of multiple TEM images of this sample reveals some junctions between the two NC phases, although significant aggregation largely prevents distinction of separate NCs. Lattice–resolved TEM image of the sample annealed at 950 °C shows the formation of large single-crystal grains, with the lattice spacing corresponding to {001} plane of β-Ga_2O_3 (5.64 Å). There is no evidence that any γ-phase is present, as expected based on the XRD results.

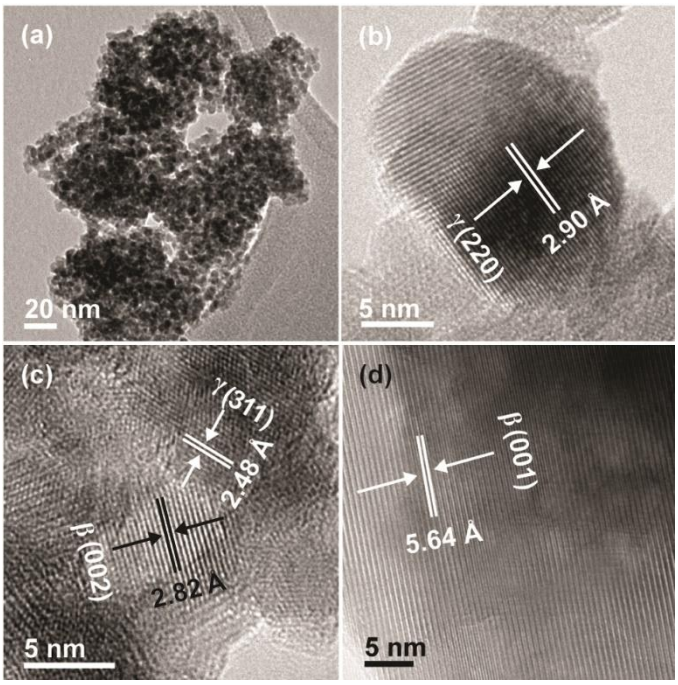

Figure 5.3. TEM images of Ga_2O_3 NCs annealed at (a, b) 400 ºC, (c) 600 ºC, and (d) 950 ºC. The assignment of the observed lattice spacing is indicated in the images.

5.2.2 Photocatalytic Evaluations

The photocatalytic activity of Ga_2O_3 samples was evaluated by monitoring the degradation of Rh-590 dye over time upon exposure to 254 nm light source. The initial concentration of Rh-590 (C_0) was determined after absorption-desorption equilibrium was achieved. Based on the Beer-Lambert law, the relative change in concentration of Rh-590 (C/C_0) is equal to the relative change in absorbance (A/A_0), where C and A are the concentration and the corresponding absorbance, respectively, at a given point in time, while A_0 is the initial absorbance corresponding to C_0. It has been suggested that the degradation of various dyes by semiconductor photocatalytic oxidation can be approximated by the Langmuir-Hinshelwood model,[91,106] which assumes the pseudo-first order kinetics:

$$\ln \frac{C_0}{C} = k_{app} t \tag{5.1}$$

where t is time and k_{app} is the apparent rate constant. The value of $\ln(C_0/C)$ plotted against time produces a linear fit where the slope equals k_{app}. A series of kinetic experiments was conducted to ensure that the concentration of Rh-590 and the mass of Ga_2O_3 NCs used were such that the reaction remains pseudo-first order. Optimal dye concentration was 2-5 mg/L and catalyst mass ≤12 mg. The Langmuir-Hinshelwood model was applied to the early stage or reaction until the minimum value of R^2 was 0.99.

Figure 5.4a shows a change in the absorption spectrum of Rh-590 in the presence of Ga_2O_3 NCs (annealed at 400 °C) for different duration of exposure to light. Absorption measurements of Rh-590 in the presence of the catalyst in dark, and exposed to UV light in the absence of the catalyst were also conducted to ensure that the degradation of the dye is a result of the photocatalytic activity. These control experiments confirmed little to no degradation of the dye. However, upon exposure to light there is a progressive decrease in the intensity of $S_0 \rightarrow S_1$ band maximum over time, indicating photocatalytic degradation. Figure 5.4b shows the Langmuir-Hinshelwood plot of the kinetic data for Ga_2O_3 samples annealed at various temperatures, together with the corresponding linear fits (Eq. 5.1). The samples annealed at temperatures below 650 °C produce a linear fit with a similar slope. Above 650 °C the slope is distinctly less steep, indicating a sharp decrease in the degradation rate.

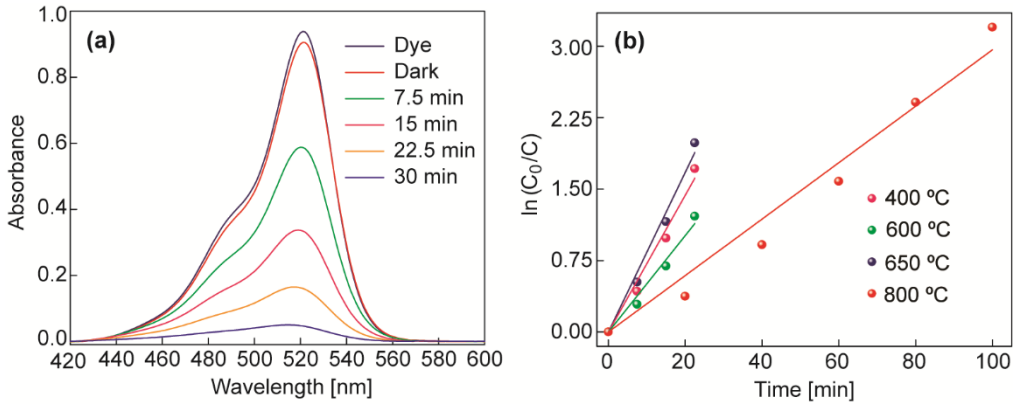

Figure 5.4. (a) Absorption spectra of Rh-590 monitored over time (as indicated in the graph) in the presence of γ-Ga_2O_3 photocatalyst under UV excitation. The photocatalyst was prepared by annealing as-synthesized NCs at 400 ºC. Black trace is the absorption spectrum of Rh-590 solution in the absence of the catalyst, and red trace is the absorption spectrum of Rh-590 stirred in dark for 30 mins in the presence of the catalyst. (b) Langmuir-Hinshelwood plot for the Rh-590 photocatalytic degradation for Ga_2O_3 prepared by annealing as-synthesized NCs at different temperatures. Straight lines are linear fits to the experimental data using Eq. 5.1.

5.2.3 Phase-Dependent Photocatalytic Activity

Figure 5.5 plots the k_{app} with respect to the annealing temperature for Ga_2O_3 NCs annealed at various temperatures from 400 °C to 1025 °C (blues spheres). All kinetic measurements were performed at least three times to determine the standard deviation. Between 400 °C and 550 °C k_{app} remains relatively constant with annealing temperature. There appears to be a slight increase in k_{app} between 550 °C and 650 °C, followed by a steep decline for samples annealed at 700 °C. Annealing at temperatures higher than 700 °C leads to a more gradual decrease in k_{app}. The specific surface area has a distinctly different behavior, displaying a continuous decrease with increasing annealing temperature (Figure 5.5, red triangles). Therefore, it is highly unlikely that the change in surface area is the sole reason for the k_{app} dependence on annealing temperature. On the other hand, the general behavior of k_{app} in Figure 5.5 is well correlated with the change in crystal structure of Ga_2O_3 shown in Figure 5.1. Importantly, a steep decrease in k_{app} upon annealing Ga_2O_3 between 600 °C and 700 °C coincides with a structural transformation from γ- to β-phase. While the samples annealed at 600 °C still contain a significant amount of γ-Ga_2O_3 (ca. 50 %), for annealing temperatures of 700 °C and higher, Ga_2O_3 is present exclusively in the β-phase. These results indicate that photocatalytic activity

is significantly larger for γ-Ga_2O_3 than for β-Ga_2O_3, which is opposite from the previously reported results.[116,127] There may also be other factors that affect the rate constant, although to a much lesser extent. As an example, it has been suggested that the presence of structurally ordered phase junctions in a mixed phase photocatalyst can lead to an increase in the photocatalytic activity by promoting the separation of charge carriers.[128] Mixed phase is evident in the samples annealed in the 550-650 °C range, which is in accord with an ostensible increase in k_{app}.

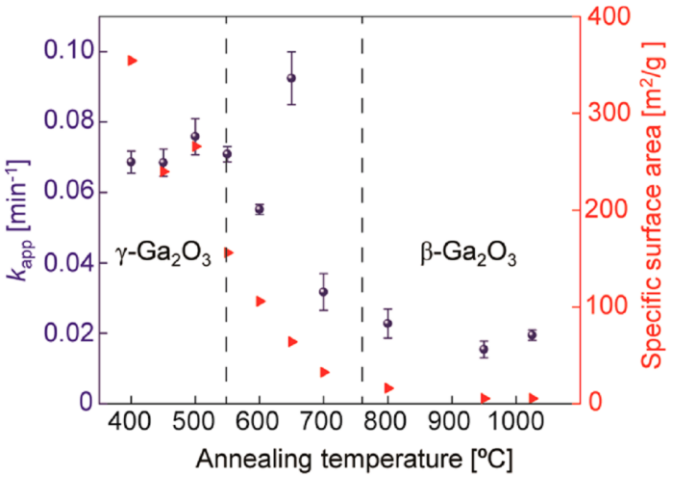

Figure 5.5. Ga_2O_3 NC annealing temperature dependence of the apparent rate constant of Rh-590 degradation (blue spheres) and the specific surface area of the photocatalyst (red triangles). The area designated with dashed lines represents the region of mixed γ-Ga_2O_3 and β-Ga_2O_3 phases.

To test this effect, larger γ-Ga_2O_3 NCs were prepared at a higher synthesis temperature (300 °C), and tested their activity upon annealing in the same temperature range. An increase in the k_{app} is observed concurrently with the appearance of β-phase in the same temperature range, confirming the possibility of the phase junction-induced increase in the k_{app} (Figure C.3 in Appendix C). Although it has been suggested that the γ/β phase junctions are disordered and cause a decrease in photocatalytic activity owing to the charge carrier trapping,[127] in our samples the presence of mixed phase has a positive influence on the photocatalytic activity. Nevertheless, any effect of the mixed phase and phase junctions is clearly minor relative to the pure phase dependence.

5.2.4 Correlation between Photodegradation Rate and Defect Concentration

To investigate the origin of the phase-dependent photocatalytic activity of Ga_2O_3, the electronic structure of the samples obtained at different annealing temperatures was examined, using steady-

state and time-resolved PL spectroscopy. Absorption spectra of all samples are nearly identical (Figure 5.6a), indicating that γ- and β-phase have practically the same band gap energy, allowing for an equivalent sensitization by using the same light source. We therefore specifically focused on the role of the defect states on the photocatalytic properties. The energy of the DAP recombination emission (E) depends on the band gap energy (E_{gap}), donor and acceptor binding energies (E_D and E_A, respectively), and the Coulomb interaction between the donor and the acceptor (E_C), as demonstrated by Eq. 4.1 in section 4.2.2.

Our previous studies have shown that the donor binding energy (electron trap depth) decreases with increasing NC size, despite the red shift of the DAP PL band with increasing NC size.[10] This correlation indicates a dominant role of the Coulomb term in Eq. 4.1, which is inversely proportional to the separation (r) between singly-charged donor and acceptor sites ($E_C=e^2/4\pi\varepsilon r$). The DAP recombination emission therefore serves as an indication of the relative concentration of the native defects (predominantly oxygen vacancies, as donor sites) in Ga_2O_3 NCs, based on their separation.

Figure 5.6b shows DAP PL bands for the photocatalytic samples annealed at different temperatures, as indicated in the graph. The DAP band red-shifts with increasing annealing temperature, indicating a decrease in the donor defect concentration (or equivalently an increase in the average separation between donors and acceptors). Thermal annealing of the samples resulted in expelling of the native defects (i.e., oxygen vacancies) from the NCs. Given the small NC size this process is effective even at low temperatures. A decrease in the defect concentration with increasing annealing temperature is also evident from time-resolved PL data. Figure 5.6c shows PL time-decay curves for Ga_2O_3 NCs before and after annealing at selected temperatures. The average PL lifetimes for the samples annealed at different temperatures (τ_{avg}) were estimated from the exponential fits. Table 5.1 summarizes the results of these fittings, including the estimated values of $\tau_{avg.}$ Increasing average separation between donors and acceptors is reflected through a prolonged electron transfer from a donor to an acceptor, as the PL decay rate determining process.

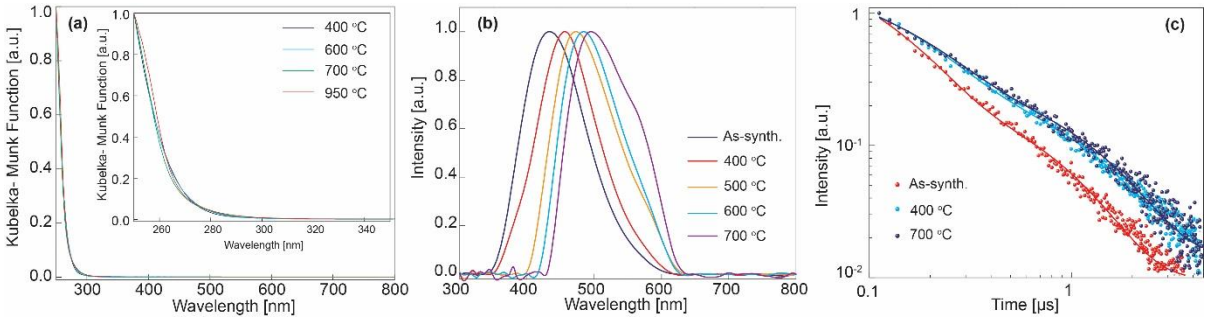

Figure 5.6. (a) Diffuse reflectance spectra of Ga_2O_3 NCs annealed at different temperatures, as indicated in the graph. Inset: magnified band edge absorption region. The spectra of all samples are nearly identical indicating negligible difference in the band gap energy between γ- and β-phase. (b) PL spectra of Ga_2O_3 NCs as-synthesized and annealed at different temperatures, as indicated in the graph. (c) Time-resolved PL data for selected samples in (a), as designated in the graph. The PL time-decay curves for the remaining samples were left out for clarity.

Table 5.1. PL Lifetime Parameters Obtained from Biexponential Fitting of the PL Time Decay Data for Ga_2O_3 NCs Annealed at Different Temperatures.

	A_1 [%]	τ_1 [μs]	A_2 [%]	τ_2 [μs]	τ_{avg} [μs]
As-synth.	30.6±0.4	0.086±0.004	69.4±0.7	0.601±0.014	0.570±0.012
400 °C	25.0±0.3	0.118±0.006	75.0±0.7	0.837±0.019	0.805±0.018
500 °C	23.6±0.4	0.115±0.005	76.4±0.8	0.863±0.022	0.833±0.020
600 °C	21.7±0.4	0.113±0.006	78.3±0.8	0.870±0.023	0.844±0.021
700 °C	22.2±0.4	0.123±0.006	77.8±0.9	0.898±0.025	0.869±0.023

These PL results can be correlated with the photocatalytic behavior. Unlike typical surface defects that may form short-lived excited states within the band gap, and are often associated with a reduced photocatalytic activity due to competitive charge carrier recombination,[95,168] the native defects in Ga_2O_3 can trap charge carriers on a microsecond to millisecond time scale before they undergo recombination. Localization of charge carriers in these long-lived trap states can facilitate charge separation and potentially enhance photocatalytic activity. According to the PL data in Figure 5.6, the concentration of defects is generally the highest in γ-Ga_2O_3 NCs annealed at low temperatures, which also corresponds to the highest photocatalytic performance. High rates of dye degradation by γ-Ga_2O_3

NCs annealed at low temperatures are also fostered by the proximity of defects to the surfaces of these nanocrystalline samples owing to their high surface-to-volume ratios. Although the concentration of native defects in γ-Ga_2O_3 NCs decreases continually with increasing annealing temperature, the expected deceleration of the photocatalytic reaction rate is likely compensated by the concurrent decrease in closely spaced donor-acceptor pairs that recombine most rapidly and are most competitive with interfacial charge transfer, and/or the appearance of the mixed phase (phase junctions). However, once the γ-phase is consumed at ca. 700 °C, the photocatalytic activity decreases rapidly. This drop in the photocatalytic performance is likely a consequence of multiple interdependent factors that accompany the phase transformation in our samples. Firstly, the β-phase is inherently less defective than the γ-phase. Secondly, the surface area of the obtained β-Ga_2O_3 is smaller than that of γ-Ga_2O_3 resulting in the lower number of defects that are preferentially formed in the surface vicinity. Thirdly, the larger average grain size of β-Ga_2O_3 brings about a larger average distance of internal defects from the surface. It should be mentioned that the red shift of the DAP emission band of β-Ga_2O_3 (700 °C annealing temperature) likely underestimates the defect separation because of the lower donor binding energy in β-Ga_2O_3 relative to γ-Ga_2O_3.[55,169] The common consequence of these phenomena is the reduced level of carriers available for interfacial charge transfer in β-Ga_2O_3. Upon annealing the β-Ga_2O_3 above 700 °C, there is a more gradual decrease in k_{app} which is governed by a further decrease in surface area.

To further demonstrate the effect of the trap states on the photocatalytic activity, and to eliminate the contributions of the grain size and surface area, In^{3+}-doped γ-Ga_2O_3 was prepared, and compared its photocatalytic performance with that of identically prepared γ-Ga_2O_3. Our research group has previously demonstrated that the band maximum and the lifetime of the DAP emission of γ-Ga_2O_3 NCs is strongly dependent on their composition.[1] Figure 5.7a shows XRD patterns of pure and 10 % In^{3+}-doped Ga_2O_3 NCs synthesized under identical conditions at 300 ºC, and subsequently annealed at 400 ºC. In^{3+}-doped Ga_2O_3 retains γ-phase crystal structure, and both samples have similar surface area (235 m^2/g for In^{3+}-doped Ga_2O_3 and 210 m^2/g for undoped Ga_2O_3), as determined by BET measurements. The PL spectra of pure and In^{3+}-doped Ga_2O_3 are compared in Figure 5.7b. The DAP PL band red shifts upon doping NCs with In^{3+}. Importantly, the red shift of the DAP emission is accompanied by a significant decrease in the emission lifetime (Figure 5.7c), indicating faster recombination of the trapped charge carriers. The kinetic data for the photocatalytic degradation of Rh-590 based on the Langmuir-Hinshelwood model (Eq. 5.1) are plotted in Figure 5.7d for undoped

and In^{3+}-doped Ga_2O_3. The linear fit to the data for undoped Ga_2O_3 has a steeper slope (blue line), indicating a decrease in the photocatalytic activity upon doping NCs with In^{3+}. The values of k_{app} determined as the fitting parameter are 0.088 and 0.035 min^{-1} for undoped and In^{3+}-doped Ga_2O_3, respectively. The decrease in the apparent rate constant upon doping NCs coincides with shortening of the DAP PL lifetime, directly confirming the role of the defect-induced trap states in the charge separation and photocatalytic activity of γ-Ga_2O_3.

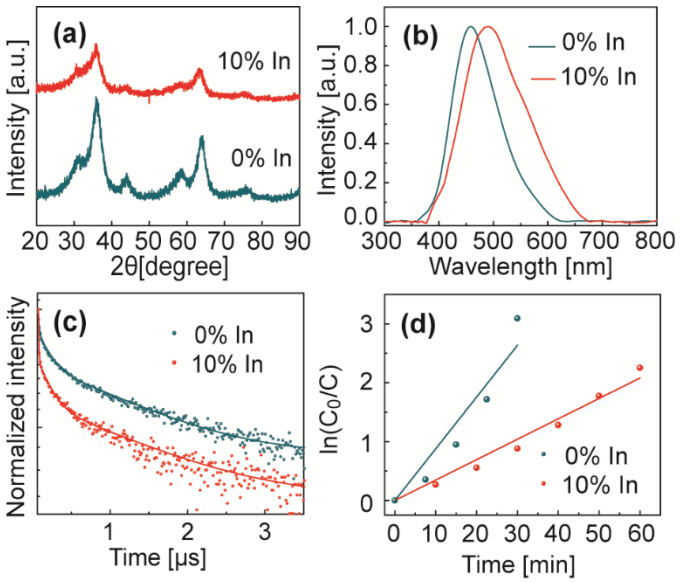

Figure 5.7. (a) XRD patterns, (b) PL spectra, and (c) time-resolved PL decays of Ga_2O_3 (blue trace) and 10 % In-doped Ga_2O_3 (red trace) NCs synthesized and annealed under the same conditions, as descried in the text. The ordinate in part (c) is logarithmic. (d) Langmuir-Hinshelwood plot for the Rh-590 photocatalytic degradation by Ga_2O_3 (blue trace) and 10 % In-doped Ga_2O_3 (red trace) samples in (a-c). Straight lines are linear fits to the experimental data using Eq. 5.1.

5.2.5 Probing the Role of Reactive Species

To probe the role of different reactive species in photocatalytic degradation of Rh-590 using γ-Ga_2O_3, the kinetic studies were performed in the presence of various scavengers (Figure C.4 in Appendix C).[170,171] Figure 5.8a shows the relative decrease in the amount of degraded dye upon addition of selected scavengers. The light-induced degradation of Rh-590 in the presence of ascorbic acid, which acts a scavenger of $O_2^{\bullet-}$ radicals, is significantly less pronounced than the degradation in the presence KSCN as an electron scavenger. The small "negative" percentage of dye degradation

with ascorbic acid suggests a displacement of Rh-590 adsorbed initially on the surfaces of the photocatalyst by the scavenger, together with completely inhibited dye degradation. A comparison between the effect of these two scavengers on the Rh-590 degradation suggests that the role of conduction band electrons is largely to generate superoxide and peroxide radical anions (Eq. 1.6 in Chapter 1), as highly oxidizing agents. Similarly, the role of the valence band holes can be inferred by comparing the effect of methanol and isopropanol on the photocatalytic efficiency. Methanol is found to be a highly efficient h_{VB}^{+} scavenger, effectively competing with H_2O and $OH^{\bullet}$ for the valence band holes. Isopropanol readily reacts with $OH^{\bullet}$, inhibiting the photocatalytic oxidation. Strong reduction in the degree of dye degradation by the addition of i-PrOH indicates the role of h_{VB}^{+} in the formation of these radicals. Despite MeOH efficiency as a hole scavenger, the comparable effect of i-PrOH suggests that the primary role of h_{VB}^{+} is the formation of $OH^{\bullet}$ (Eqs. 1.7 and 1.8 in Chapter 1). These results indicate a particularly important role of reactive radicals ($OH^{\bullet}$ and $O_2^{\bullet-}$) in the mechanism of dye degradation, and suggest that the main effect of the separated electron-hole pairs is through the formation of these radicals.

5.2.6 Photocatalyst Robustness

The γ-Ga_2O_3 photocatalyst shows stable performance after multiple cycles (Figure 5.8b). A small decrease in the photocatalytic activity observed after several cycles is associated with the strong adsorption of a fraction of dye molecules which block a relatively small portion of the surface sites. Mild temperature treatment can remove these strongly-bound dye molecules, reestablishing the original activity of the photocatalyst. Importantly, the structure and morphology of γ-Ga_2O_3 remain unchanged after recycling (Figure C.5 in Appendix C). The efficient photocatalytic degradation by nanocrystalline γ-Ga_2O_3 is general and applicable to a wide range of conjugated dyes and other organic pollutants. Figure 5.8c shows the photocatalytic degradation of MB in 2 mg/L aqueous solution using γ-Ga_2O_3 prepared by annealing as-synthesized NCs at 400 °C. MB is degraded to a greater extent within 10 minutes of exposure to light than Rh-590 in a solution of the same concentration (Figure C.6 in Appendix C), suggesting a higher degradation rate of MB relative to Rh-590. Figure 5.8d compares the kinetics of MB and Rh-590 degradation under identical conditions, based on the Langmuir-Hinshelwood model. The value of k_{app} calculated for MB is 0.35 min^{-1}, which is 75 % higher than that for Rh-590, demonstrating dye-dependence of the photocatalytic rate. This dependence is likely induced by a higher adsorption affinity of MB on NC surfaces, as well as higher

rate of MB oxidation by $OH^{\bullet}$ and $O_2^{\bullet -}$ radicals. Anomalous photocatalytic activity of nanocrystalline γ-Ga_2O_3 toward degradation of colorless organic pollutants was also confirmed (Figure C.7 in Appendix C).

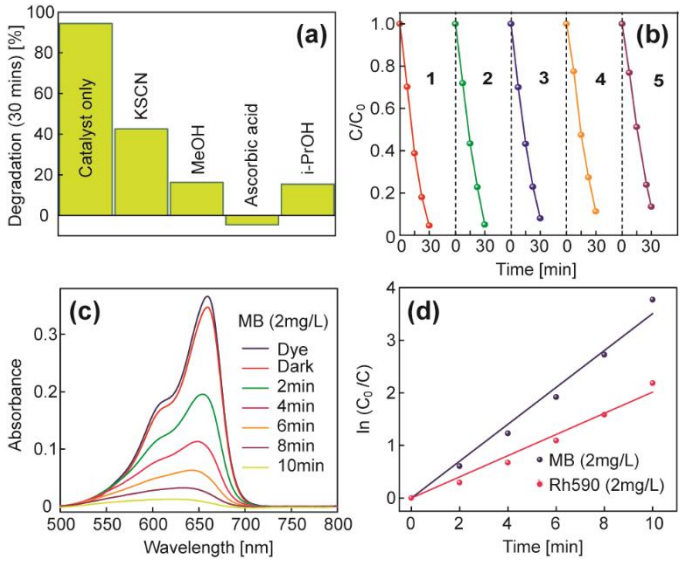

Figure 5.8. (a) Percentage of the photocatalytic degradation of Rh-590 by γ-Ga_2O_3, prepared by annealing as-synthesized NCs at 400 ºC, in the presence of various scavengers, as indicated in the graph. (b) Photocatalytic activity of γ-Ga_2O_3 for the degradation of Rh-590 measured over 5 cycles. (c) Absorption spectra of MB solution (2 mg/L) monitored over time in the presence of γ-Ga_2O_3 photocatalyst under UV excitation. The photocatalyst was prepared by annealing as-synthesized NCs at 400 ºC. Absorption spectra of MB solution in the absence of the catalyst (blue trace) and stirred in dark for 30 mins in the presence of the catalyst (red trace) are shown for comparison. (d) Langmuir-Hinshelwood plots for the MB (blue spheres) and Rh-590 (red spheres) photocatalytic degradation measured under identical conditions for the same Ga_2O_3 photocatalyst. Straight lines are linear fits to the experimental data using Eq. 5.1.

5.2.7 Proposed Mechanism of Photochemistry

Finally, we wish to discuss the origin of this anomalous photocatalytic activity of γ-Ga_2O_3. In most photocatalytic NCs, typical defect-induced trap states are a source of efficient charge recombination, and in addition to exciton recombination result in a decrease in the photocatalytic activity (Figure 5.9a). The photogenerated charge carrier separation in such NCs is usually enabled by the formation of various types of heterojunctions. However, in γ-Ga_2O_3 NCs electrons and holes trapped in shallow

long-lived donor and acceptor states, respectively,[10] can access the NC surface before undergoing mutual recombination (Figure 5.9b). The unique nature of these defect and their proximity to the NC surfaces promotes interfacial charge transfer to adsorbed reactants at the expense of charge recombination, resulting in the enhanced photocatalytic activity. Although long-lived trap states exist in β-Ga_2O_3 as well, the corresponding defect sites are present in lower concentration and on average located further away from the surfaces, reducing the interfacial charge transfer responsible for the photocatalytic activity.

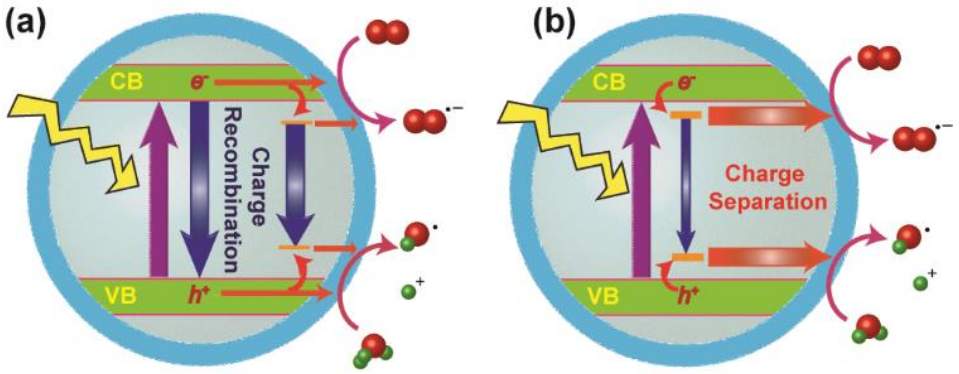

Figure 5.9. Schematic representation of the competition between the charge carrier recombination and interfacial energy transfer in photocatalytic NCs: (a) Semiconductor NCs containing typical surface states that favor charge recombination, and (b) Ga_2O_3 NCs containing long-lived defect trap states, resulting in a reduced charge recombination and enhanced interfacial charge transfer. Higher concentration of defects and their closer proximity to NC surfaces in γ-Ga_2O_3 relative to β-Ga_2O_3 leads to higher photocatalytic activity. Red spheres represent oxygen, and green spheres represent hydrogen atoms.

5.3 Conclusions

In summary, a series of Ga_2O_3 photocatalyst samples was prepared by annealing colloidally-synthesized γ-Ga_2O_3 NCs at various temperatures between 400 °C and 1025 °C. For annealing temperatures below ca. 550 °C the NCs aggregate, but remain in the γ-phase. The formation of β-phase becomes evident at ca. 575 °C and the samples are fully converted to β-Ga_2O_3 at ca. 700 °C. Using these samples it was demonstrated that γ-phase has superior photocatalytic activity, which cannot be solely ascribed to a decrease in surface area with increasing annealing temperature. Using

steady-state and time-resolved PL spectroscopy, it was shown that γ-Ga_2O_3 possesses a higher concentration of native defects (oxygen vacancies) relative to β-Ga_2O_3, and that the decrease in photocatalytic activity is strongly correlated with the phase transformation from γ- to β-phase. Surprisingly, a larger number of long-lived charge carrier traps in γ-Ga_2O_3, induced by its more defective structure, results in a reduced rate of charge recombination and enhanced probability of charge transfer to surface-adsorbed reactants. Both of these mutually related phenomena are enabled by the unique character and long lifetime of defect-induced traps in Ga_2O_3. Furthermore, the closer proximity of defects to the surface of nanocrystalline γ-Ga_2O_3 promotes more efficient charge transfer responsible for its photocatalytic activity. Using appropriate scavengers, it was shown that reactive radicals ($OH^{\bullet}$ and $O_2^{\bullet -}$) play a major role in the mechanism of photocatalytic degradation by Ga_2O_3. The results of this work demonstrate how manipulation of the electronic structure of defect sites in metal oxides, allowed by the control of the crystal phase and size, can be effectively used to control charge carrier separation and enhance photocatalytic activity, while retaining high surface-to-volume ratio. Although this work emphasizes the role of polymorphism, other means of optimizing the photocatalytic performance by controlling the defect structure, including synthesis conditions, morphology, and composition represent a rich area for future research.

Chapter 6
Synergistic Effect of Defect Chemistry and Surface Active Sites in GTO to Form a Highly Efficient Photocatalyst

6.1 Overview

Sustained human endeavor is required to address the worldwide issues such as energy shortages and environmental pollution. Heterogeneous photocatalysis has already drawn a great amount of interest as a remedy to photochemical degradation of organic dyes in wastewater. Among many other factors affecting the performance of a photocatalyst are the number of active sites, redox potential of the VB and CB, electron-hole generation efficiency and charge carrier recombination rate. Herein, the synthesis of gallium tin oxide ternary catalyst (GTO), by the coprecipitation method, across the entire composition range is reported, and the role of dopant in altering the electronic structure of the catalysts, by employing time-resolved and steady-state photoluminescence spectroscopy, is investigated. An excellent performance of GTO catalysts for photodegradation of Rh-590 was observed, possessing an apparent rate constant two times greater than that of commercial catalyst, P25. Through structural and spectroscopic analysis, it is shown that expansion of surface area is not the solitary reason for the high performance of the catalysts. While the CB carriers are photocatalytically inactive in pure SnO_2 due to having a lower reductive potential than water, the incorporation of Ga^{3+} in SnO_2 lattice blueshifts the band gap absorption, leading to photoactivity of CB electrons. Another advantage of Ga doping is the trapping of VB holes by acceptors (Ga^{3+} ions), which, in conjunction with the CB electrons trapping by donors (oxygen vacancies), leads to stabilization of the photoexcited carriers. The charge recombination retardation, high surface area, and redox-suitable CB and VB synergistically promote the efficiency of the GTO photocatalysts. However, at high doping concentration, the increased density of donor-acceptor pairs shortens the

lifetime of photoexcited carriers, reducing the degradation rate. In this report, the role of scavengers is also discussed in order to understand the mechanism of photodecomposition. The use of scavengers revealed that a degradation process proceeds through the generation of electrons, holes, hydroxyl and superoxide radicals. We hope the concepts of rational doping for band alignment modification, systematic control of intrinsic and extrinsic defect concentration, as well as charge recombination kinetics serve as an instructive model to design versatile highly efficient photocatalysts to preserve the planet.

6.2 Results and Discussion

6.2.1 The Effect of Composition on Crystal Structure

XRD patterns and TEM images of representative GTO NCs are exhibited in Figure 6.1 and Figure D.1 (Appendix D). As indicated in Figure 6.1a, the patterns of undoped SnO_2 and Ga_2O_3 are indexed to bulk rutile SnO_2 (JCPDS 088-0287, red sticks), and bulk γ-Ga_2O_3 (JCPDS 020-0426, blue sticks), respectively. The broadened diffraction peaks are indicative of small average NC size. Doping Ga^{3+} as a smaller size cation (0.62 Å in an octahedral site) in SnO_2 with cationic radius of 0.69 Å causes the lattice to shrink, evidenced by shifting the XRD patterns towards higher angles. This, furthermore, signifies the substitutional doping of the Group IIIA in the rutile structure. Impurity-induced crystal deformation leads to a notable widening in the diffraction patterns. However, no secondary phase is identified with the addition of the dopant, even at high doping concentration. The NCs retain SnO_2 rutile structure until the starting concentration of Ga reaches 75%, after which γ-Ga_2O_3 is the dominant phase. Elemental analysis results (Table D.1 in Appendix D) reveal that the concentrations of the two cations are virtually equal in the sample with Ga nominal concentration of 75%, elucidating the capability of SnO_2 in hosting a large portion of Ga to compose a solid solution. An overview and high resolution TEM images of GTO NCs with nominal Ga concentration of 25% are illustrated in Figure 6.1b and 6.1c. The size of spherical particles is sub- 5 nm and some degree of aggregation is observed. The measured lattice fringes (Figure 6.1c) are slightly smaller than their {110} plane of SnO_2 counterpart due to the smaller ionic radius of Ga^{3+} compared to Sn^{4+}. To ensure uniform distribution of Sn and Ga in the NCs and lack of phase segregation, EDX elemental mapping on GTO NCs with starting Ga concentration of 75% was performed (Figure 6.1d-f). Homogenous dispersion of the two cations on the TEM grid is apparent. The typical high resolution TEM images of the rest of GTO NCs are demonstrated in Figure D.1 (Appendix D) for comparison.

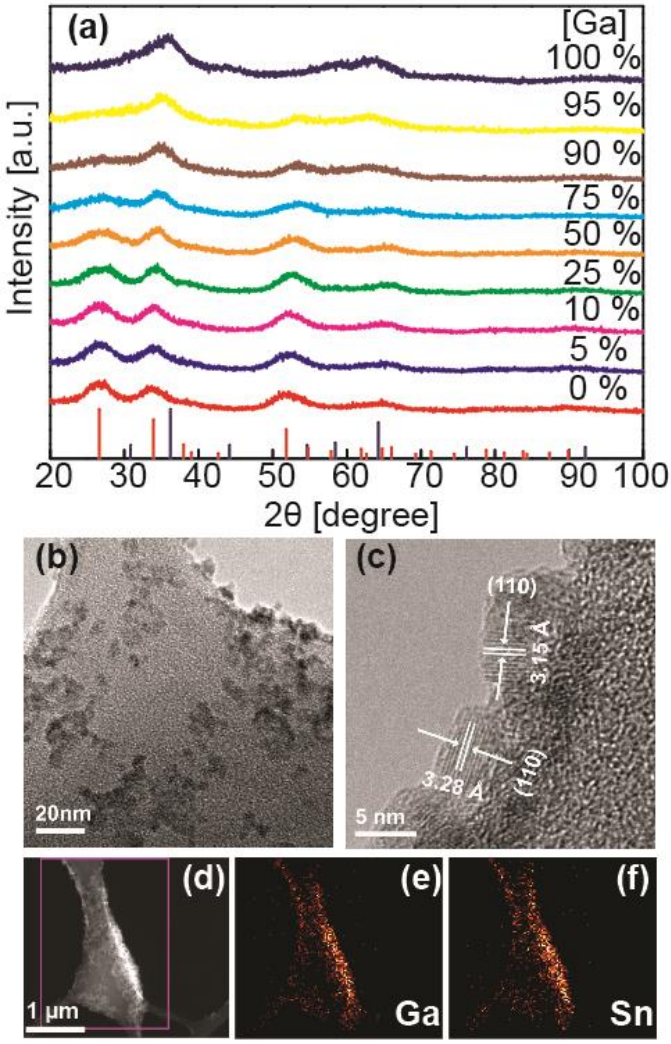

Figure 6.1. (a) XRD patterns of GTO NCs with different Ga contents as indicated in the graph. Red and blue sticks represent the patterns of bulk rutile SnO_2 and γ-Ga_2O_3, respectively. (b and c) TEM images of GTO NCs with nominal Ga contents 25%. The measured lattice fringes correspond to rutile SnO_2 in (c). (d-f) EDX elemental mapping of GTO NCs containing 75% Ga, as labeled in the panels.

6.2.2 Optical Study of GTO NCs

While the large band gap of γ-Ga_2O_3 (4.9 eV) supplies photogenerated carriers with oxidative and reductive power, low CBM of SnO_2 fails to the produce photocatalytically active electrons. However, doping SnO_2 with Ga^{3+} is a feasible method to design catalysts with the appropriate electronic

structure for photodegradation of pollutants, using photoactive electrons and holes. The widening of the band gap with increasing Ga content in GTO NCs is illustrated in Figure 6.2a, indicating composition-dependent electronic structure of the alloyed semiconductors. This provides an opportunity to promote the reductive strength of CBM of GTO NPs by upshifting it towards vacuum level. Inducing extrinsic defects in the nanoparticles' structure is an inevitable consequence of aliovalent doping.[43,85] Considering Ga^{3+} has less positive charge compared to Sn^{4+}, gallium cations act as acceptors in the tin oxide lattice, and form energy states above the VB. The complex of these acceptors with native defects (oxygen vacancies) generates donor-acceptor pairs, functioning as radiative recombination centers for photoexcited electron and holes. It was shown in Chapter 4 that photoluminescence of hydrothermally synthesized GTO can be tuned in the visible range by altering the composition and reaction conditions. The PLQY of the NCs is determined by competition between the rate of radiative and nonradiative recombination of the excited carriers, and is promoted with the addition of Ga by favoring the radiative pathway. The same trend in the emission tunability and PLQY of GTO NCs prepared by the sol-gel method is observed, as demonstrated in Figure 6.2b and 6.2d. As evident from Figure 6.2c and Table D.2 (Appendix D), the lifetimes of carriers in GTO NCs are on a microsecond scale and it increases with the addition of Ga, up to ca. 25% Ga. This occurs as it generates trap states in which the excited carriers decay slowly and, consequently, the lifetime lengthens. However, when the concentration of Ga passes beyond 25%, the increase in donor-acceptor pair concentrations causes a reduction in their average separation, resulting in a higher probability of recombination (Figure 6.2d). Short-lived excited carriers are harmful to the photocatalytic activity, in which quantum yield is determined by two rivaling steps. The first competition takes place between free charge carrier recombination and trapping on defect-induced energy states. Next, the trapped carriers recombination competes against interfacial charge transfer.[95,96,115] It is believed that the recombination rate is suppressed by the longer lifetime of the carriers in the trap states compared to free carriers, leading to higher photocatalytic efficiency.[105,172] It is assumed that nanostructuring and generation of more trap states by Ga doping lead to an increase in charge transfer to the surface and charge separation, respectively. These characteristics of GTO NCs could potentially challenge TiO_2 as a highly efficient photocatalyst.

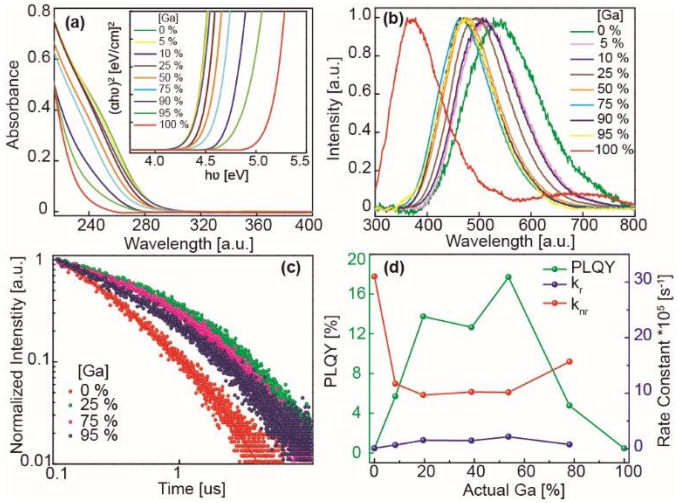

Figure 6.2. (a) Composition dependence of band edge absorption of GTO NCs with different Ga contents as indicated in the graph. (b) PL spectra of GTO NCs with different Ga concentrations as demonstrated in the graph. (c) Time-resolved PL decay of selected GTO NCs, as indicated in the graph, on microsecond time scale. The PL lifetime data of the rest of samples were left out for clarity. (d) Comparison between radiative and non-radiative rate constants of GTO NCs and their effect on PLQY.

6.2.3 Photocatalytic Evaluations of GTO NCs

The photodegradation of Rh-590 in the presence of GTO catalysts was achieved under the irradiation of 254nm UV light and the kinetic data was extracted using Langmuir–Hinshelwood model, expressed by the following equation.[123]

$$-\frac{dC}{dt} = \frac{k_r K_{ad} C}{1+K_{ad} C} \tag{6.1}$$

where (−dC/dt) and C are the photodegradation rate and the concentration of the dye, respectively, t is the reaction time, k_r is the reaction rate constant, and K_{ad} is the adsorption coefficient of the dye. When $K_{ad}C$ <<1 (low concentration of the dye), the kinetics model can be approximated as first-order kinetics.

$$ln\frac{C_0}{C} = k_r K_{ad} t = k_{app.} t \tag{6.2}$$

where C_0 is the initial concentration of the organic dye and $k_{app.}$ is the apparent rate constant. $k_{app.}$ can be withdrawn from a plot of $ln(C_0/C)$ against time and serves as the basic kinetic parameter to assess the photocatalytic activity of various catalysts.

A typical change in the absorption spectrum of Rh-590 in the presence of GTO NCs with 25% Ga content is presented in Figure D.2 (Appendix D). Two sets of control experiments were carried out to ensure the reduction in the absorption spectra is due to photodegradation (not shown). In the first experiment, the change in the absorption of Rh-590 was monitored under UV lamp in the absence of catalyst. A negligible change was observed, confirming the stability of Rh-590 under UV exposure. The examination of absorption in the presence of the catalyst in dark revealed that nearly 50% of the dye is adsorbed on the surface after 15 minutes of sonication and the absorption spectrum does not change afterward. The photocatalytic activity of GTO NCs was calculated by using Eq. 6.2 and the Langmuir-Hinshelwood plot of the representative catalyst is demonstrated in Figure 6.3a. As demonstrated, the photochemical conversion is enhanced with Ga doping and it reaches a maximum when the starting of Ga is 25%, after which the degradation rate deteriorates. Figure D.2b (Appendix D) shows the dependence of photodegradation and charge recombination kinetics on the composition. Although the lifetime in the microsecond regime simultaneously increases with photodegradation rate constant for GTO NCs containing up to 25% Ga, it fails to anticipate the activity throughout the full composition range. The dynamics of electron-hole generation and recombination, which was explored by comprehensive study performed by Rothenberger et. al,[146] were explained in Section 1.5.4 in Chapter 1 (Eqs. 1.9 to 1.13).[95,96,99]

Therefore, the time-resolved PL of GTO NCs on the nanosecond scale was acquired (Figure 6.3b and Table D.3 in Appendix D) and compared the obtained lifetime with the photochemical conversion rate (Figure 6.3c). The agreement between the apparent rate constant and the lifetime of photogenerated carriers in the nanosecond scale is distinctly improved compared to microsecond-range lifetime. At lower concentration of Ga ([Ga] $\leq$ 25%), where the number of acceptor levels (hole traps) is low, carriers are trapped in the corresponding donor and acceptor energy states (Eq. 1.13), retarding the charge recombination. However, a high concentration of donor-acceptor pairs ([Ga] $\leq$ 50%) facilitates the charge recombination due to the closer proximity of donor-acceptor pairs (Eq. 1.12), decreasing the photocatalytic activity.

The contribution of surface area enhancement in promoting the photocatalytic activity is irrefutable, although it is not always the sole determining factor for photodegradation rate. Other parameters such as light absorption, charge separation efficiency and the rate of charge transfer to the surface must be taken into account.[96] Here, I wish to discuss the impact of specific surface area (S_{BET}) on $k_{app.}$ in conjunction with lifetime (Table D.4 in Appendix D). There appears to be an increase in S_{BET} with growing Ga concentration in the entire composition range. As evident from Table D.4 (Appendix D) and Figure 6.3d, $k_{app.}$ does not follow the same trend. A 2.8-fold increase in S_{BET} upon increasing the Ga concentration from 0% to 25% coincides with a 3.5 -fold increase in $k_{app.}$, while the lifetime of photoexcited carriers experiences a 2-fold increase. As a result, it is justifiable to hold both large surface area and long-lived excited carrier responsible for photodegradation rate escalation in this range. There happens to be an opposite trend in S_{BET} and $k_{app.}$ with further increase in Ga content from 25% to 90%. Faster charge carrier recombination plays the key role in photoactivity of the catalysts in this range, while surface area remains increasing. The efficiency of the catalysts is a complex function of surface area and charge recombination rate and the control over these factors leads to the design of catalysts with optimal performance.

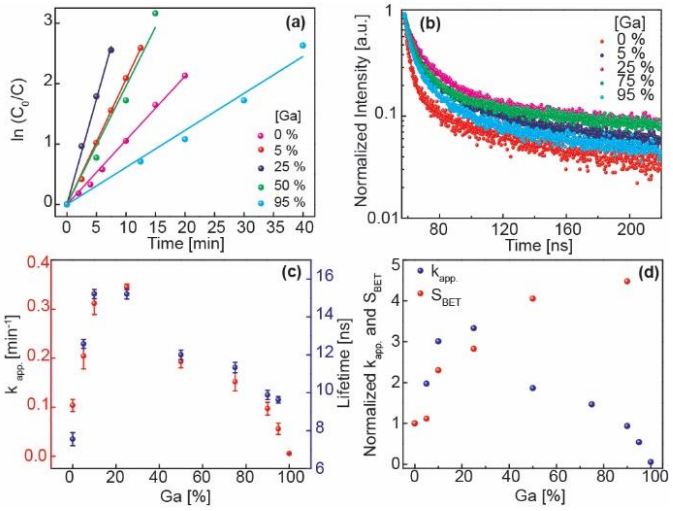

Figure 6.3. (a) Langmuir-Hinshelwood plot of selected GTO NCs photocatalytic activity for degradation of Rh-590. Straight lines are linear fits to the experimental data using Eq. 6.2. (b) Time-resolved PL decay of selected GTO NCs, as indicated in the graph, on nanosecond timescale. The data of the rest of samples were left out for clarity in (a) and (b). (c) Composition reliance of apparent rate constant and the lifetime of GTO NCs on the nanosecond timescale. (d) A comparison between

normalized apparent rate constant and specific surface area of GTO NCs. The $k_{app.}$ and S_{BET} of GTO NCs are divided by the corresponding value for pure SnO_2 in (d).

To further probe the impact of trap states on the rate of photodegradation, 10 % In-doped SnO_2 was prepared to compare its photocatalytic activity with that of undoped SnO_2 synthesized under identical conditions. The crystal structure of 10 % In-doped SnO_2 is identical to rutile SnO_2, as determined by XRD patterns in Figure D.3a (Appendix D). While the doped NCs possess similar band edge absorption as pure SnO_2, there appears to be a blue shift in its PL due to a higher density of DAPs (Figure D.3b in Appendix D). The emission lifetime of the NCs shows a significant increase from 7.5±0.3 ns to 13.0±0.2 ns upon doping (Figure D.3c in Appendix D). The lower probability of charge recombination in the nanosecond regime is caused by the presence of defect-induced trap states upon doping with In^{3+}. The apparent rate constants for photocatalytic degradation of Rh-590 by SnO_2 and 10 % In-doped SnO_2 were extracted from the Langmuir-Hinshelwood plot in Figure D.3d (Appendix D) and determined to be 0.10 min^{-1} and 0.26 min^{-1}, respectively. The higher rate of photodegradation of Rh-590 by 10 % In-doped SnO_2 is attributed to its prolonged DAP PL lifetime. This verifies the influence of extrinsically induced trap states on modulating the charge carrier dynamics leading to the design of highly-active photocatalysts.

6.2.4 Exploring the Influence of Preparation Method on Photocatalytic Activity

Our research group has conducted several studies on γ-Ga_2O_3 to investigate the correlation between interaction of native and extrinsic defects and their effect on photonic properties of this oxide.[1,57,173,174] Because the photoactivity of γ-Ga_2O_3 prepared by colloidal synthesis is explored in Chapter 5, under the same condition as the work reported here, it is relavant to examine the impact of preparation methods on the electronic structure and hence, the catalytic activity of γ-Ga_2O_3.[175] The estimated size of colloidally synthesized particles at 300 °C was ca. 6 nm [11] and their apparent rate constant was determined to be 0.088 min^{-1}.[175] The average size of NCs, obtained by deconvolution of XRD peaks and employing the Scherrer equation, is ca. 1.8 nm (Figure D.4a in Appendix D), three times smaller than the colloidal counterpart.[16,54] However, the apparent rate constant drops to 0.006 min^{-1} for γ-Ga_2O_3 synthesized by the sol-gel method (Figure 6.3c), indicating that the decrease in the activity of sol-gel γ-Ga_2O_3 does not stem from a smaller number of active sites but electronic structure alteration must be considered. As illustrated in Figure D.4b and Figure D.4d (Appendix D), the band gap absorption edge and the emission of the sol-gel sample shift to higher energies compared to

colloidal Ga_2O_3, possibly due to quantum confinement. This phenomenon was previously reported in ultrathin single layer γ-Ga_2O_3.[117] The photoluminescence emission of γ-Ga_2O_3 has been interpreted by the donor-acceptor pair model and the energy of DAP emission (E) can be described by Eq. 4.1 in section 4.2.2. Oxygen vacancies are considered donors and the complex of gallium and oxygen vacancies are considered acceptors. Given the smaller size of sol-gel particles, the density of defects increases in the structure, leading to a larger Coulomb interaction (third term) between donor-acceptor pairs and consequently a higher energy of the emission. This is also evident in excitation spectra presented in Figure D.4c (Appendix D). The higher density of defects favors the faster charge recombination, resulting in the low photocatalytic activity (Figure 6.3c). We do not overlook the role that lower absorption of UV light plays in decreasing the apparent rate constant, as the band gap widens, although band gap widening raises the redox potential, generating carriers with higher oxidative and reductive potential. Introduction of Sn^{4+} in γ-Ga_2O_3 lattice not only reduces the band gap, but also forms donor states whose energy is lower compared to intrinsic donors (oxygen vacancies). The presence of low-lying defect states is implied by the red shift in PL and excitation spectra, illustrated in Figure 6.1b and Figure D.5 (Appendix D), respectively. The ab initio theoretical calculations supported the existence of such Sn-based defect states within the band gap of β-Ga_2O_3 whose energy was determined to be located 0.2 E_g below the CB minimum.[43] The stability of trapped electrons in Sn-driven states harnesses the UV light energy to yield higher photodegradation (Figure 6.3c). This highlights the significance of synthetic conditions and dopants on controlling defect chemistry and tailoring the electronic structure of nanomaterials, which empower ones to exploit their functional properties.

6.2.5 A Comparison between the Activity of P25 and GTO Photocatalysts

To evaluate the efficiency of GTO photocatalysts versus an external reference, the recognized benchmark catalysts, P25, was chosen. The photodegradation measurement was performed under identical conditions as described earlier for GTO NCs. Figure 6.4a compares the photodegradation efficiency of P25 with two of GTO catalysts which demonstrated superior photodecomposition of Rh-590 in Figure 6.3c. Intriguingly, the apparent rate constant of both GTO catalysts surpasses that of P25, the $k_{app.}$ of 25GTO being two times higher than P25. To assess the reusability of 25GTO NCs the photodegradation reaction of Rh-590 was conducted in 5 consecutive cycles under identical conditions. As indicated in Figure 6.4b, GTO NCs possess high photocatalytic activity even after 5 cycles with the average degradation percentage of 92.3 ±3.5 % in 12 minutes. No meaningful change

in the concentrations of Ga or Sn was noticed by EDX (Table D.1 in Appendix D). The catalyst retained its structural and morphological properties (Figure D.6 in Appendix D) after 5 cycles, implying long-term stability and use of GTO photocatalysts in environmental remediation. The generality of higher photocatalytic activity of GTO NCs versus undoped SnO_2 was investigated further for degradation of a phenol solution with the concentration of 5 mg/L (Figure 6.4c and Figure D.7 in Appendix D). $k_{app.}$ of 10GTO is 50% higher than its undoped rival, validating the approach taken in this work. Altogether, this epitomizes the impact of rational doping in designing robust catalysts to degrade a variety of hazardous wastes, pushing the limits of photocatalysis by outperforming P25.

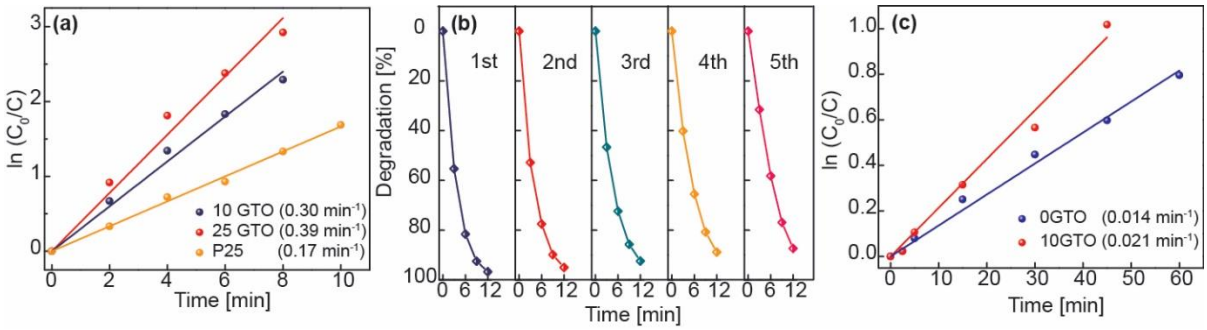

Figure 6.4. (a) Comparing the photocatalytic activity of selected GTO NCs for degradation of Rh-590 with that of P25 through Langmuir-Hinshelwood plot. (b) Monitoring the photocatalytic activity of GTO NCs with 25% Ga content for the degradation of Rh-590 over 5 cycles. (c) Comparison between the photocatalytic activity of undoped SnO_2 with GTO NCs containing 10 % Ga for the degradation of Rh-590. The apparent rate constants are given in the parenthesis in (a and c). Straight lines in (a and c) are linear fits to the experimental data using Eq. 6.2.

6.2.6 Probing the Impact of Composition on Band Alignment

Various scavengers were employed to explore the role of different redox species in the photocatalytic degradation of Rh-590 in presence of GTO NCs containing 0-25% Ga. Regardless of the size of SnO_2-based photocatalysts, the potential of VB of this oxide is more positive than the oxidation potential of water. In other words, the VB hole is an active oxidative species, capable of photodecomposition of the organic dye. The degradation percentage, as indicated in Figure 6.5a and 6.5b, declined in the presence of $NaHCO_3$ and methanol, independent from the composition of the catalyst. The exploited scavengers are known to react with hydroxyl radicals and holes, rendering the

VB photogenerated carrier inoperative. On the other hand, the photoactivity of CB carriers could be affected by the size of particles and doping, as CBM of bulk SnO_2 is less negative than the reduction potential of water and therefore, the CB photoexcited electrons are photocatalytically ineffectual. Quantum confinement and Ga doping may enlarge the band gap, opening doors to manipulate the two carriers to achieve high degradation efficiency. $FeCl_3$ and N_2 were exploited to scavenge electrons and superoxide radicals, respectively. $FeCl_3$ and N_2 did not cause a meaningful change in the degradation percentage of Rh-590 in the presence of SnO_2 photocatalyst, as illustrated in Figure 6.5c and 6.5d. This could infer that the negative shift in the potential of CB, due to quantum confinement, was not enough to activate the reductive power of electrons in CB. The other plausible reason might be that the energy level of trap state is located below the hydrogen reduction position and thus, unable to drive photodegradation. In contrast, the inhibition of Rh-590 degradation in presence of doped samples signifies the production of catalytically active electrons located in high-lying CBM of these oxides. All in all, it can be concluded that the role of VB in all selected catalysts is to produce holes and hydroxyl radicals, responsible for the oxidation of organic dyes, while CB of doped samples contributes in the redox reaction by delivering electrons and superoxide radicals. Strikingly, it has been illustrated that the charge recombination dynamics, surface area and the functionality of nanomaterials can be altered, through aliovalent doping and manipulation of defect chemistry. These principles can potentially play a significant role for environmental remediation.

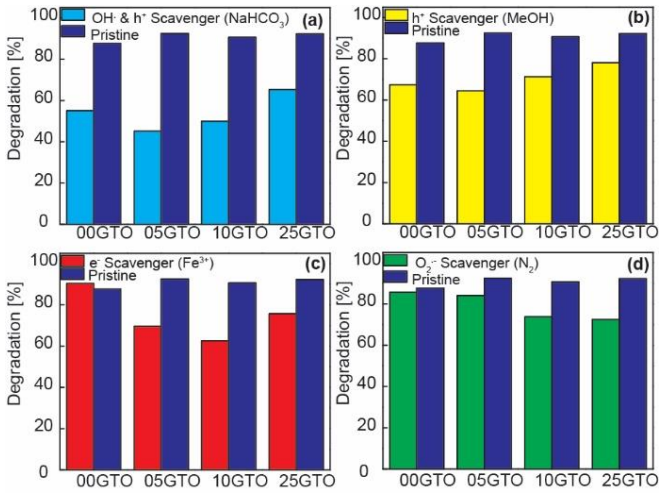

Figure 6.5. (a) Photodegradation percentage of Rh-590 by selected GTO catalysts and in presence of varied scavengers, as indicated in graphs: (a) $NaHCO_3$, (b) Methanol, (c) $FeCl_3$, (d) N_2. The photodegradation percentage of each pair (pristine catalyst and in presence of a scavenger) was

calculated after exposure to UV light for the same length of time. The waiting time for 00GTO, 05GTO, 10GTO, and 25GTO are 20 minutes, 12.5 minutes, 7.5 minutes and 7.5 minutes, respectively.

6.3 Conclusions

In summary, the synthesis of ternary gallium tin oxide was successfully achieved by sol-gel method. The size of these particles was determined to be sub-5 nm by TEM and X-ray diffraction. Such nanostructuring shortens the pathway for the photogenerated carriers to access the surface, reducing the possibility of charge recombination in the bulk as well as growing surface-to-volume ratio and therefore, creating more photocatalytically active sites. Moreover, band gap absorption showed that Ga doping widens the band gap, stimulating the reduction of the organic pollutants by the CB electrons which are idle in undoped SnO_2. More importantly, the charge recombination is hindered due to the presence of the electrons and holes trap states within the band gap, originated from oxygen vacancies and Ga^{3+} doping. This enables more efficient charge transfer to the surface and therefore boost the photodegradation rate. However, closer proximity of defects, induced by heavy doping (> 25%), quickens the charge recombination rate which is detrimental to catalytic activity. Comparing the degradation rate of Rh-590 in presence of P25 and GTO NCs reveals a remarkable performance of GTO photocatalysts, holding $k_{app.}$ of 0.39 min^{-1} versus 0.17 min^{-1} for P25. The catalyst maintains high photocatalytic activity even after 5 cycles and no notable change in the crystal structure, morphology and composition were observed, proposing GTO NCs as an efficient substitute for P25. The photodecomposition in presence of various scavengers showed that electrons, holes, hydroxyl, and superoxide radicals are four active species in the photodegradation of organic dyes. The outcome of this work enlightens how electronic structure of nanomaterials can be tailored to employ the full redox capability of oxides with low-lying CBM such as SnO_2. The underlying principle is applicable to other oxides such as WO_3 and TiO_2 (rutile phase). The approach taken in this work can be developed to other systems as understanding the nature and role of defects in stabilizing the excited carriers is pivotal for the design of enhanced photocatalytic activity.

Chapter 7
Conclusions and Prospective Research Directions

7.1 Conclusions

Generally, the obligation for enhancement of inherent properties of materials is indisputable to fulfil the ever-increasing ecological concerns and universal demand for energy. The improvement of functional properties of nanomaterials plays a prominent role to tackle such issues because their physical properties differ from those of their bulk counterparts owing to the influence of quantum confinement as well as increased surface-to-volume ratio. The latter highlights the impact of defects in reduced dimensions. Herein, the significance of defect chemistry to improve the operational properties of materials at the nanoscale was methodically investigated, emphasizing the enrichment of this field of research.

Briefly, the PL properties of Eu-doped In_2O_3 was investigated in the context of Eu oxidation states and the host lattice crystal structure. The interaction between the dopant and In_2O_3 native defects resulted in blue (Eu^{2+}) or red (Eu^{3+}) emission in both rhombohedral and body-centred cubic In_2O_3. The size and phase of the host lattice as well as dopant oxidation state were found to be invaluable tools for controlling intrinsic defects. Eu^{2+} incorporation stabilizes oxygen vacancies, which in turn sensitize Eu^{3+} emission, demonstrating the interdependence of defect formation, dopant incorporation and PL of colloidal NC constituents. The simultaneous control over the host lattice crystal structure, the lanthanide dopant oxidation states and defect concentration facilitates the modulation of emission properties and thereby generation of multifunctional TCOs.

The hydrothermal synthesis of new ternary gallium tin oxide NCs was reported. Composition dependence of PL color from blue to orange-red was also demonstrated. Substitutional incorporation of Ga into the SnO_2 lattice generated acceptor levels within the band gap, which is responsible for a simultaneous increase in intrinsic donors ($V_O^{\bullet}$) to compensate for charge imbalance. While SnO_2 NCs possess low PLQY due to non-radiative recombination of photogenerated carriers, the extrinsically induced DAPs establish a new radiative recombination pathway, leading to PLQY enhancement (> 40 %). Stronger Coulomb interaction between the donor-acceptor pairs and band gap widening simultaneously give rise to the blue shift of the DAP emission of GTO NCs with an increase in Ga^{3+} doping level. A faster PL decay rate originates from a smaller separation between electron and hole

trap states which itself is correlated with an increase in Ga content. Improving the long-range order of NCs by increased reaction duration and temperature is another means of lessening non-radiative recombination mechanisms. Wide range emission tunability, high efficiency as well as chemical stability and inertness are attractive features of these TCOs for illumination industries active in the production of light sources with ideal scotopic/photopic ratio and appreciable PLQY. Concurrent control of the composition and defect interactions enabled the conversion of non-luminescent TCO NCs into efficient and tunable phosphors. Well-chosen synthetic method as well as reaction conditions enable the generation of efficient emitters with distinctive features.

Colloidally-synthesized γ-Ga_2O_3 NCs were annealed at varied temperatures (400- 1025 °C) to study the impact of the phase of Ga_2O_3, native defect concentration and the role in charge trapping on photocatalytic activity. γ-Ga_2O_3 was obtained for low annealing temperature (≤ 550 °C). Evidence of β-Ga_2O_3 emerged at ca. 575 °C and NCs adopted β-phase at ca. 700 °C. It was shown that the higher activity of γ-phase could not be entirely attributed to a reduction in surface area upon annealing at elevated temperature. The larger number of native defects ($V_O^{\bullet}$) in γ-Ga_2O_3 compared to β-Ga_2O_3 was demonstrated, utilizing steady-state and time-resolved PL spectroscopy. Possessing a higher concentration of long-lived charge carrier traps in γ-Ga_2O_3 leads to an increase in charge recombination retardation and enhancement of charge transfer to the surface. More efficient photocatalytic activity of γ-Ga_2O_3 is also enabled by the closer proximity of defects to the surface of NCs. The key role of $OH^{\bullet}$ and $O_2^{\bullet-}$ in the mechanism of degradation of organic dyes by Ga_2O_3 was also disclosed by using appropriate scavengers. This work illustrated that the control of crystal phase and size allows for the manipulation of electronic structure of defects in TCOs, resulting in more efficient charge carrier separation and thus high photocatalytic performance, while preserving high surface area. A rich area for future research would be investigating the role of synthetic conditions, morphology, and composition on the defect structure and photocatalytic activity.

Sol-gel synthesis of ternary gallium tin oxide resulted in sub-5 nm nanostructures in which the possibility of charge recombination in the bulk is reduced due to the shortened pathway for the photogenerated carriers to reach the surface. In addition, band gap widens with increasing Ga content, leading to the photocatalytic degradation of organic pollutants by the photogenerated electrons in CB which are inactive in undoped SnO_2. More importantly, trapping electrons and holes in the sates originated from oxygen vacancies and Ga^{3+} doping, lessens the charge recombination rate. This results in more efficient interfacial charge transfer, and therefore, improving the photodegradation

rate. Heavy doping (> 25%) leads to a smaller average separation between donors and acceptors, inducing faster charge recombination, and hence, decreasing catalytic activity. The degradation rate of Rh-590 by GTO NCs is more than two times higher than that of P25. The high photocatalytic activity remains even after 5 cycles, without any meaningful change in the crystal structure, morphology and composition. Using various scavengers confirms that electrons, holes, hydroxyl, and superoxide radicals are four active species in the photodegradation process. The ability to modulate electronic structure of substances results in employing CB electrons as well as VB holes in nanomaterials with low-lying CBM such as SnO_2, which is furthermore applicable to other oxides such as WO_3 and TiO_2 (rutile phase). Understanding the role of defects in the dynamics of excited carriers is essential for enhancing the photocatalytic performance.

7.2 Outlook

The incorporation of multivalent rare-earth ions in the host lattice induces additional defects which may act as luminesce centers. Doping other rare-earth elements having multiple oxidation states, such as Sm and Ce, is an attractive research area as it provides the opportunity to simultaneously study the morphology, structure and optical properties of oxides. A systematic investigation of the influence of chemistry and charge of these lanthanides on PL properties of oxides provides further insight into lattice-dopant interaction and result in the enhancement of functionalities of complex TCOs. These defects may induce and enhance other functional properties of TCOs, such as conductivity. Consequently, the ability to control both structure and composition paves the way to engineer multifunctional nanomaterials. It must be stated that the relatively facile design of lanthanide-doped NCs allows an additional degree of freedom to obtain upconverting NCs with application in drug delivery and light stimulated therapies. In addition, rare-earth codoping is a feasible strategy to generate white light through the emission of complementary colors. The combination of multiple luminescence centers, such as blue (Ce^{3+}), green (Tb^{3+}) and red (Eu^{3+}) in a lattice poses many challenges. Therefore, a highly structured study must be conducted to control various participating variables. Nevertheless, this study would be particularly instructive and shed more light on the sequential energy transfer process between the constituent elements and their interactions with the host lattice.

Heterovalent doping has emerged as a viable method to enrich both electrical and optical properties of semiconductors. A controlled addition of n-type and p-type dopants incorporates negatively and

positively charged carriers, respectively. This enhances the electric conductivity and generates localized surface plasmon resonance in the host lattice.[84] Doping Nb in SnO_2 is of particular interest because it exists in Nb^{3+} and Nb^{5+} and as a result, it induces p-type and n-type conductivity, respectively. Controlling the ratio of the two oxidation states is feasible by employing oxidative or reducing environment and could lead to tuning plasmon resonance of the NCs in a wide range.

As shown in Chapter 5, heterovalent ions can also generate localized energy states within the band gap of NCs to trap electrons or holes which serve as radiative recombination centers. The activation energy of these states may vary, depending on the nature of the dopant. Therefore, the inclusion of multiple PL centers in SnO_2 might be achievable through addition of Ga^{3+} and Zn^{2+}. Transition metal doped TCOs has exhibited strong ferromagnetism.[176] Concurrent incorporation of Ga^{3+} and transition metals, such as manganese, in SnO_2 would be a beneficial study as it could lead to the generation of multifunctional GTO NCs.

It must be mentioned that an inherent limitation of nanostructure doping is the exclusion of the foreign ions from the host lattice. Thus, the influence of dopants on the electronic properties of NCs have not been entirely studied due to the lack of robust synthetic methods. More recently, incorporation of dopant pairs (such as two cations, two anions or a cation and an anion) appeared to be an effective strategy to alter electronic properties of the host because of the following reasons which lead to an improvement in doping efficiency.[60,177] The charge imbalance introduced by the primary dopant is balanced by the codopant. Moreover, if the codopant with an appropriate ionic radius is selected, it can suppress the disorder in host lattice induced by the primary impurity, resulting in a considerable improvement in PLQY. Rational execution of codoping would lead to tunability of electrical and optical properties of the nanostructure. Despite the complexity of such systems, these studies are motivated by technological applications.

It is anticipated that the annual consumption of energy on earth triples by 2100.[178] Therefore, the design of sustainable energy sources is a major concern for humanity. It is universally accepted that the sun is the most dependable source of energy because the energy delivered by the sun to the surface of the earth within 80 minutes, satisfies human's entire annual need. Accordingly, the attempts to design high-performing catalysts for water splitting and environmental remediation have been directed toward small band gap semiconductors to tune visible light harvesting. Calculations have demonstrated that informed choice of dopants may significantly alter the band gap. Despite

having a large band gap, density functional theory calculations demonstrated that the electronic structure of Ga_2O_3 can be notably modified by non-metal doping.[45] It was illustrated that I-doped and Se-doped β-Ga_2O_3 can shrink the band gap of Ga_2O_3 to 2.64 and 2.8 eV, respectively; nevertheless they deliver doubly active photogenerated carriers for photocatalysis in water.

Although very promising advances have been made in the field of photocatalysis, the performance of the present photocatalysts is not yet satisfactory. Overcoming the limitations of single component catalysts is enabled by integrating multiple components which lead to taking advantage of the functionality of individual components. To date, charge recombination is a major drawback. Due to the smaller band gap of sulfide-based semiconductors, forming a heterojunction between oxides and sulfides may give rise to the charge cascading processes if appropriate band alignment is chosen. Varying the size of the component which is subject to quantum confinement effect, influences the kinetics of charge separation significantly and thus, is an intriguing subject to study. As mentioned earlier, a major limiting factor in scalable photon-assisted degradation of hazardous wastes is the low absorption of the solar spectrum. Integration of transition metal oxides with large band gap semiconductors combines the aforementioned effect with visible light absorption. Plasmon-mediated solar-to-chemical energy conversion, which allows for the utilization of the solar energy in the NIR range, is under extensive research in various fields, from photocatalysis to solar cells.[179,180]

7.3 Closing Remarks

The inherent properties of chemicals indisputably need improvement to satisfy the technological requirements in the modern era. The synthetic chemistry of nanomaterials has created a diverse class of substances with a wide range of applications. Yet, significant technical challenges remain for chemists to optimize the conditions for the incorporation of different properties in a compound to induce multifunctionality. The central task to exploit such operational properties is unravelling the mechanism deriving them. A fundamental understanding of the driving forces enables the control of the electronic structure, morphology and structure of nanomaterials, resulting in an improved efficiency and features for various applications.

Further advances will largely depend on the development and effective utilization of advanced techniques. Spectroscopic measurements which uncover the dynamics of light-driven phenomena, are widely employed techniques. Ultrafast spectroscopic measurements provide deeper mechanistic insight into multi-competing processes such as electron-hole generation, charge trapping and charge

transport. Invaluable information gained from these techniques helps the rational design of the systems and leads to the enhancement of the efficiency of light-stimulated functionalities.

Ultimately, it is sensible that a further understanding of crystal growth and doping mechanisms as well as developing more advanced characterization tools will lead to the controlled incorporation of impurities in NCs in the future. Well-designed synthetic methods synchronized with characterization technique improvements will allow for the predetermined occupation of the NC lattice by the constituent atoms and/or dopants, leading to the rational engineering of defect-induced properties.

Letter of Copyright Permission

Title: Anomalous Photocatalytic Activity of Nanocrystalline γ-Phase Ga2O3 Enabled by Long-Lived Defect Trap States

Author: Vahid Ghodsi, Susi Jin, Joshua C. Byers, et al

Publication: The Journal of Physical Chemistry C

Publisher: American Chemical Society

Date: May 1, 2017

Logged in as:
Vahid Ghodsi
Account #:

LOGOUT

PERMISSION/LICENSE IS GRANTED FOR YOUR ORDER AT NO CHARGE

This type of permission/license, instead of the standard Terms & Conditions, is sent to you because no fee is being charged for your order. Please note the following:

- Permission is granted for your request in both print and electronic formats, and translations.
- If figures and/or tables were requested, they may be adapted or used in part.
- Please print this page for your records and send a copy of it to your publisher/graduate school.
- Appropriate credit for the requested material should be given as follows: "Reprinted (adapted) with permission from (COMPLETE REFERENCE CITATION). Copyright (YEAR) American Chemical Society." Insert appropriate information in place of the capitalized words.
- One-time permission is granted only for the use specified in your request. No additional uses are granted (such as derivative works or other editions). For any other uses, please submit a new request.

BACK CLOSE WINDOW

Bibliography

1 S. S. Farvid, T. Wang and P. V. Radovanovic, *J. Am. Chem. Soc.*, 2011, **133**, 6711–6719.

2 Q. Dai, M. E. Foley, C. J. Breshike, A. Lita and G. F. Strouse, *J Am Chem Soc*, 2011, **133**, 15475–15486.

3 M. K. Gish, A. M. Lapides, M. K. Brennaman, J. L. Templeton, T. J. Meyer and J. M. Papanikolas, *J. Phys. Chem. Lett.*, 2016, **7**, 5297–5301.

4 M. Alonso-Orts, A. M. Sánchez, S. A. Hindmarsh, I. López, E. Nogales, J. Piqueras and B. Méndez, *Nano Lett.*, 2017, **17**, 515–522.

5 X. Zhao, Z. Wu, W. Cui, Y. Zhi, D. Guo, L. Li and W. Tang, *ACS Appl. Mater. Interfaces*, 2017, **9**, 983–988.

6 C. Yu, G. Li, S. Kumar, K. Yang and R. Jin, *Adv. Mater.*, 2014, **26**, 892–898.

7 L. N. Hutfluss and P. V. Radovanovic, *J. Am. Chem. Soc.*, 2015, **137**, 1101–1108.

8 S. S. Farvid and P. V Radovanovic, *J. Am. Chem. Soc.*, 2012, **134**, 7015–7024.

9 H. Zhang and J. F. Banfield, *J. Phys. Chem. B*, 2000, **104**, 3481–3487.

10 T. Wang and P. V. Radovanovic, *J. Phys. Chem. C*, 2011, **115**, 18473–18478.

11 T. Wang, S. S. Farvid, M. Abulikemu and P. V Radovanovic, *J. Am. Chem. Soc.*, 2010, **132**, 9250–9252.

12 S. S. Farvid, N. Dave, T. Wang and P. V. Radovanovic, *J. Phys. Chem. C*, 2009, **113**, 15928–15933.

13 K. L. Chopra, S. Major and D. K. Pandya, *Thin Solid Films*, 1983, **102**, 1–46.

14 D. S. Ginley, H. Hosono and D. C. Paine, Eds., *Handbook of Transparent Conductors*, Springer, New York, 2011.

15 A. Klein, *J. Am. Ceram. Soc.*, 2013, **96**, 331–345.

16 T. Wang and P. V Radovanovic, *J. Phys. Chem. C*, 2011, **115**, 406–413.

17 Z. Zhuang, Q. Peng, J. Liu, X. Wang and Y. Li, *Inorg. Chem.*, 2007, **46**, 5179–5187.

18 J. Philip, A. Punnoose, B. I. Kim, K. M. Reddy, S. Layne, J. O. Holmes, B. Satpati, P. R. LeClair, T. S. Santos and J. S. Moodera, *Nat. Mater.*, 2006, **5**, 298–304.

19 S. S. Farvid, N. Dave and P. V. Radovanovic, *Chem. Mater.*, 2010, **22**, 9–11.

20 R. D. Shannon, *Solid State Commun.*, 1966, **4**, 629–630.

21 A. Solieman, M. K. Zayed, S. N. Alamri, N. Al-Dahoudi and M. A. Aegerter, *Mater. Chem. Phys.*, 2012, **134**, 127–132.

22 M. Epifani, P. Siciliano, A. Gurlo, N. Barsan and U. Weimar, *J. Am. Chem. Soc.*, 2004, **126**, 4078–4079.

23 C. H. Lee, M. Kim, T. Kim, A. Kim, J. Paek, J. W. Lee, S. Y. Choi, K. Kim, J. B. Park and K. Lee, *J. Am. Chem. Soc.*, 2006, **128**, 9326–9327.

24 Q. Liu, W. Lu, A. Ma, J. Tang, J. Lin and J. Fang, *J. Am. Chem. Soc.*, 2005, **127**, 5276–5277.

25 C. H. Liang, G. Meng, Y. Lei, F. Phillipp and L. Zhang, *Adv. Mater.*, 2001, **13**, 1330–1333.

26 T. Sabergharesou, T. Wang, L. Ju and P. V. Radovanovic, *Appl. Phys. Lett.*, 2013, **103**, 12401.

27 X. Xu, J. Zhuang and X. Wang, *J. Am. Chem. Soc.*, 2008, **130**, 12527–12535.

28 H. J. Snaith and C. Ducati, *Nano Lett.*, 2010, **10**, 1259–1265.

29 M. S. Park, G. X. Wang, Y. M. Kang, D. Wexler, S. X. Dou and H. K. Liu, *Angew. Chem. Int. Ed.*, 2007, **46**, 750–753.

30 K. Suito, N. Kawai and Y. Masuda, *Mater. Res. Bull.*, 1975, **10**, 677–680.

31 M. Batzill and U. Diebold, *Prog. Surf. Sci.*, 2005, **79**, 47–154.

32 A. A. Bolzan, C. Fong, B. J. Kennedy and C. J. Howard, *Acta Crystallogr. Sect. B Struct. Sci.*, 1997, **53**, 373–380.

33 D. Maestro, A. Cremades and J. Piqueras, *J. Appl. Phys.*, 2004, **95**, 3027–3030.

34 X. T. Zhou, F. Heigl, M. W. Murphy, T. K. Sham, T. Regier, I. Coulthard and R. I. R. Blyth, *Appl. Phys. Lett.*, 2006, **89**, 213109.

35 B. Liu, C. W. Cheng, R. Chen, Z. X. Shen, H. J. Fan and H. D. Sun, *J. Phys. Chem. C*, 2010, **114**, 3407–3410.

36 K. G. Godinho, A. Walsh and G. W. Watson, *J. Phys. Chem. C*, 2009, **113**, 439–448.

37 M. De Murcia, M. Egge and J. P. Fillard, *J. Phys. Chem. Solids*, 1978, **39**, 629–635.

38 H. Zhou, R. Deng, Y. F. Li, B. Yao, Z. H. Ding, Q. X. Wang, Y. Han, T. Wu and L. Liu, *J. Phys. Chem. C*, 2014, **118**, 6365–6371.

39 B. Zheng, W. Hua, Y. Yue and Z. Gao, *J. Catal.*, 2005, **232**, 143–151.

40 W. Zhang, B. S. Naidu, J. Z. Ou, A. P. O'Mullane, A. F. Chrimes, B. J. Carey, Y. Wang, S. Y. Tang, V. Sivan, A. Mitchell, S. K. Bhargava and K. Kalantar-Zadeh, *ACS Appl. Mater. Interfaces*, 2015, **7**, 1943–1948.

41 M. Muruganandham, R. Amutha, M. S. M. A. Wahed, B. Ahmmad, Y. Kuroda, R. P. S. Suri, J. J. Wu and M. E. T. Sillanpää, *J. Phys. Chem. C*, 2012, **116**, 44–53.

42 T. Wang, V. Chirmanov, W. H. M. Chiu and P. V. Radovanovic, *J. Am. Chem. Soc.*, 2013, **135**, 14520–14523.

43 S. I. Maximenko, L. Mazeina, Y. N. Picard, J. A. Freitas, V. M. Bermudez Jr. and S. M. Prokes, *Nano Lett.*, 2009, **9**, 3245–3251.

44 W.-Z. Xiao, L.-L. Wang, L. Xu, Q. Wan and A.-L. Pan, *Solid State Commun.*, 2010, **150**, 852–856.

45 W. Guo, Y. Guo, H. Dong and X. Zhou, *Phys. Chem. Chem. Phys.*, 2015, **17**, 5817–5825.

46 M. Martin, R. Dronskowski, J. Janek, K. D. Becker, D. Roehrens, J. Brendt, M. W. Lumey, L. Nagarajan, I. Valov and A. Börger, *Prog. Solid State Chem.*, 2009, **37**, 132–152.

47 K. Nishi, K. Shimizu, M. Takamatsu, H. Yoshida, A. Satsuma, T. Tanaka, S. Yoshida and T. Hattori, *J. Phys. Chem. B*, 1998, **102**, 10190–10195.

48 H. Y. Playford, A. C. Hannon, M. G. Tucker, D. M. Dawson, S. E. Ashbrook, R. J. Kastiban, J. Sloan and R. I. Walton, *J. Phys. Chem. C*, 2014, **118**, 16188–16198.

49 S. E. Collins, M. A. Baltanás and A. L. Bonivardi, *Langmuir*, 2005, **21**, 962–970.

50 T. Harwig, F. Kellendonk and S. Slappendel, *J. Phys. Chem. Solids*, 1978, **39**, 675–680.

51 L. Binet and D. Gourier, *J. Phys. Chem. Solids*, 1998, **59**, 1241–1249.

52 W. Shockley and W. T. Read Jr., *Phys. Rev.*, 1952, **87**, 835–842.

53 G. Blasse and A. Brill, *J. Phys. Chem. Solids*, 1970, **3**, 707–711.

54 M. Hegde, T. Wang, Z. L. Miskovic and P. V. Radovanovic, *Appl. Phys. Lett.*, 2012, **100**, 141903.

55 T. Wang and P. V. Radovanovic, *Chem. Commun.*, 2011, **47**, 7161–7163.

56 T. Wang, A. Layek, I. D. Hosein, V. Chirmanov and P. V. Radovanovic, *J. Mater. Chem. C*, 2014, **2**, 3212–3222.

57 A. Layek, B. Yildirim, V. Ghodsi, L. N. Hutfluss, M. Hegde, T. Wang and P. V. Radovanovic, *Chem. Mater.*, 2015, **27**, 6030–6037.

58 V. Ghodsi, A. Layek, M. Hegde, B. Yildirim and P. Radovanovic, *Chem. Commun.*, 2016, **52**, 4353–4356.

59 S. S. Farvid, M. Hegde and P. V Radovanovic, *Chem. Mater.*, 2013, **25**, 233–244.

60 J. Z. Zhang, J. K. Cooper and S. Gul, *J. Phys. Chem. Lett.*, 2014, **5**, 3694–3700.

61 G. Zhang, C. Xie, S. Zhang, S. Zhang and Y. Xiong, *J. Phys. Chem. C*, 2014, **118**, 18097–18109.

62 J. J. Teh, S. L. Ting, K. C. Leong, J. Li and P. Chen, *ACS Appl. Mater. Interfaces*, 2013, **5**, 11377–11382.

63 M. D. Regulacio and M. Y. Han, *Acc. Chem. Res.*, 2010, **43**, 621–630.

64 D. Turnbull, *J. Appl. Phys.*, 1950, **21**, 1022–1028.

65 D. Chen, R. Viswanatha, G. L. Ong, R. Xie, M. Balasubramaninan and X. Peng, *J. Am. Chem. Soc.*, 2009, **131**, 9333–9338.

66 G. M. Dalpian and J. R. Chelikowsky, *Phys. Rev. Lett.*, 2006, **96**, 1–4.

67 D. J. Norris, A. L. Efros and S. C. Erwin, *Science (80-.).*, 2008, **319**, 1776–1779.

68 S. C. Erwin, L. Zu, M. I. Haftel, A. L. Efros, T. A. Kennedy and D. J. Norris, *Nature*, 2005, **436**, 91–94.

69 R. Buonsanti and D. J. Milliron, *Chem. Mater.*, 2013, **25**, 1305–1317.

70 X. Pan and Y. Xu, *J. Phys. Chem. C*, 2013, **117**, 17996–18005.

71 S. V. Eliseeva and J.-C. G. Bünzli, *Chem. Soc. Rev.*, 2010, **39**, 189–227.

72 A. Chakraborty, G. H. Debnath, N. R. Saha, D. Chattopadhyay, D. H. Waldeck and P. Mukherjee, *J. Phys. Chem. C*, 2016, **120**, 23870–23882.

73 P. Manna, A. Chakraborty, G. H. Debnath and P. Mukherjee, *J. Phys. Chem. Lett.*, 2017, **8**, 2794–2798.

74 R. Arppe, I. Hyppänen, N. Perälä, R. Peltomaa, M. Kaiser, C. Würth, S. Christ, U. Resch-Genger, M. Schäferling and T. Soukka, *Nanoscale*, 2015, **7**, 11746–11757.

75 P. Głuchowski, W. Stręk, M. Lastusaari and J. Hölsä, *Phys. Chem. Chem. Phys.*, 2015, **17**, 17246–17252.

76 K. Li, M. Shang, Y. Zhang, J. Fan, H. Lian and J. Lin, *J. Mater. Chem. C*, 2015, **3**, 7096–7104.

77 M. Xin, D. Tu, H. Zhu, W. Luo, Z. Liu, P. Huang, R. Li, Y. Cao and X. Chen, *J. Mater. Chem. C*, 2015, **3**, 7286–7293.

78 Z. Xia, S. Miao, M. Chen, M. S. Molokeev and Q. Liu, *Inorg. Chem.*, 2015, **54**, 7684–7691.

79 L. Prodi, E. Rampazzo, F. Rastrelli, A. Speghini and N. Zaccheroni, *Chem. Soc. Rev.*, 2015, **44**, 4922–4952.

80 N. Riesen, A. François, K. Badek, T. M. Monro and H. Riesen, *J. Phys. Chem. A*, 2015, **119**, 6252–6256.

81 T. Tachikawa, T. Ishigaki, J. G. Li, M. Fujitsuka and T. Majima, *Angew. Chemie - Int. Ed.*, 2008, **47**, 5348–5352.

82 J. K. Cooper, S. Gul, S. a Lindley, J. Yano and J. Z. Zhang, *ACS Appl. Mater. Interfaces*, 2015, **7**, 10055–10066.

83 J. Liu, Q. Zhao, J. L. Liu, Y. S. Wu, Y. Cheng, M. W. Ji, H. M. Qian, W. C. Hao, L. J. Zhang, X. J. Wei, S. G. Wang, J. T. Zhang, Y. Du, S. X. Dou and H. S. Zhu, *Adv. Mater.*, 2015, **27**, 2753–2761.

84 J. Zhang, Q. Di, J. Liu, B. Bai, J. Liu, M. Xu and J. Liu, *J. Phys. Chem. Lett.*, 2017, **8**, 4943–

4953.

85 C.-L. Hsu and Y.-C. Lu, *Nanoscale*, 2012, **4**, 5710–5717.

86 Q. Mao, Z. Ji and L. Zhao, *Phys. Status Solidi*, 2010, **247**, 299–302.

87 L. Mazeina, Y. N. Picard, S. I. Maximenko, F. K. Perkins, E. R. Glaser, M. E. Twigg, J. a. Freitas and S. M. Prokes, *Cryst. Growth Des.*, 2009, **9**, 4471–4479.

88 A. Mishra and J. H. Clark, in *Green Materials for Sustainable Water Remediation and Treatment*, eds. A. Mishra and J. H. Clark, The Royal Society of Chemistry, 2013, pp. 1–10.

89 M. A. Shannon, P. W. Bohn, M. Elimelech, J. G. Georgiadis, B. J. Mariñas and A. M. Mayes, *Nature*, 2008, **452**, 301–310.

90 H. Zollinger, *Color Chemistry. Synthesis, Properties and Applications of Organic Dyes and Pigments.*, Third, revised ed.; Verlag Helvetica Chimica Acta AG: Zurich, Switzerland, 2003.

91 I. K. Konstantinou and T. A. Albanis, *Appl. Catal. B Environ.*, 2004, **49**, 1–14.

92 A. Houas, H. Lachheb, M. Ksibi, E. Elaloui, C. Guillard and J. M. Herrmann, *Appl. Catal. B Environ.*, 2001, **31**, 145–157.

93 A. Fujishima and K. Honda, *Nature*, 1972, **238**, 37–38.

94 M. D. Hernández-Alonso, F. Fresno, S. Suárez and J. M. Coronado, *Energy Environ. Sci.*, 2009, **2**, 1231–1257.

95 A. L. Linsebigler, G. Lu and J. T. Yates Jr, *Chem. Rev.*, 1995, **95**, 735–758.

96 M. R. Hoffmann, S. T. Martin, W. Choi and D. W. Bahnemannt, *Chem. Rev.*, 1995, **95**, 69–96.

97 C. Gao, J. Wang, H. Xu and Y. Xiong, *Chem. Soc. Rev.*, 2017, **46**, 2799–2823.

98 A. Kudo and Y. Miseki, *Chem. Soc. Rev.*, 2009, **38**, 253–278.

99 A. Mills and S. Le Hunte, *J. Photochem. Photobiol. A Chem.*, 1997, **108**, 1–35.

100 Y. Qu and X. Duan, *Chem. Soc. Rev.*, 2013, **42**, 2568–2580.

101 H. Wang, L. Zhang, Z. Chen, J. Hu, S. Li, Z. Wang, J. Liu and X. Wang, *Chem. Soc. Rev.*, 2014, **43**, 5234–5244.

102 J. Yan, G. Wu, N. Guan, L. Li, Z. Li and X. Cao, *Phys. Chem. Chem. Phys.*, 2013, **15**, 10978–

10988.

103 A. Sclafani and J. M. Herrmann, *J. Phys. Chem.*, 1996, **100**, 13655–13661.

104 D. A. H. Hanaor and C. C. Sorrell, *J. Mater. Sci.*, 2011, **46**, 855–874.

105 M. Sachs, E. Pastor, A. Kafizas and J. R. Durrant, *J. Phys. Chem. Lett.*, 2016, **7**, 3742–3746.

106 M. A. Fox and M. T. Dulay, *Chem. Rev.*, 1993, **93**, 341–357.

107 Y. Gai, J. Li, S. S. Li, J. B. Xia and S. H. Wei, *Phys. Rev. Lett.*, 2009, **102**, 36402.

108 H. Kato and A. Kudo, *J. Phys. Chem. B*, 2002, **106**, 5029–5034.

109 R. Niishiro, R. Konta, H. Kato, W. J. Chun, K. Asakura and A. Kudo, *J. Phys. Chem. C*, 2007, **111**, 17420–17426.

110 R. Niishiro, H. Kato and A. Kudo, *Phys. Chem. Chem. Phys.*, 2005, **7**, 2241–2245.

111 M. Marelli, C. Evangelisti, M. V. Diamanti, V. Dal Santo, M. P. Pedeferri, C. L. Bianchi, L. Schiavi and A. Strini, *ACS Appl. Mater. Interfaces*, 2016, **8**, 31051–31058.

112 X. Y. Liu, H. Chen, R. Wang, Y. Shang, Q. Zhang, W. Li, G. Zhang, J. Su, C. T. Dinh, F. P. G. de Arquer, J. Li, J. Jiang, Q. Mi, R. Si, X. Li, Y. Sun, Y. T. Long, H. Tian, E. H. Sargent and Z. Ning, *Adv. Mater.*, 2017, **29**, 1–8.

113 M. Kong, Y. Li, X. Chen, T. Tian, P. Fang, F. Zheng and X. Zhao, *J. Am. Chem. Soc.*, 2011, **133**, 16414–16417.

114 K. Zhang and J. H. Park, *J. Phys. Chem. Lett.*, 2017, **8**, 199–207.

115 J. Zhuang, W. Dai, Q. Tian, Z. Li, L. Xie, J. Wang, P. Liu, X. Shi and D. Wang, *Langmuir*, 2010, **26**, 9686–9694.

116 Y. Hou, L. Wu, X. Wang, Z. Ding, Z. Li and X. Fu, *J. Catal.*, 2007, **250**, 12–18.

117 X. Zhang, Z. Zhang, J. Liang, Y. Zhou, Y. Tong, Y. Wang and X. Wang, *J. Mater. Chem. A*, 2017, **5**, 9702–9708.

118 J. Zhang, Z. Xiong and X. S. Zhao, *J. Mater. Chem.*, 2011, **21**, 3634–3640.

119 S. Zhuang, X. Xu, B. Feng, J. Hu, Y. Pang, G. Zhou, L. Tong and Y. Zhou, *ACS Appl. Mater. Interfaces*, 2014, **6**, 613–621.

120 Ç. Kılıç and A. Zunger, *Phys. Rev. Lett.*, 2002, **88**, 95501.

121 E. J. Yeom, S. S. Shin, W. S. Yang, S. J. Lee, W. Yin, D. Kim, J. H. Noh, T. K. Ahn and S. Il Seok, *J. Mater. Chem. A*, 2017, **5**, 79–86.

122 W. Zhao, M. Zhang, Z. Ai, Y. Yang, H. Xi, Q. Shi, X. Xu and H. Shi, *J. Phys. Chem. C*, 2014, **118**, 23117–23125.

123 M. T. Uddin, Y. Nicolas, C. Olivier, T. Toupance, L. Servant, M. M. Müller, H. J. Kleebe, J. Ziegler and W. Jaegermann, *Inorg. Chem.*, 2012, **51**, 7764–7773.

124 S. Joshi, S. J. Ippolito and M. V. Sunkara, *RSC Adv.*, 2016, **6**, 43672–43684.

125 P. Li, Y. Lan, Q. Zhang, Z. Zhao, T. Pullerits, K. Zheng and Y. Zhou, *J. Phys. Chem. C*, 2016, **120**, 9253–9262.

126 M.-G. Ju, X. Wang, W. Liang, Y. Zhao and C. Li, *J. Mater. Chem. A*, 2014, **2**, 17005–17014.

127 S. Jin, X. Wang, X. Wang, M. Ju, S. Shen, W. Liang, Y. Zhao, Z. Feng, H. Y. Playford, R. I. Walton and C. Li, *J. Phys. Chem. C*, 2015, **119**, 18221–18228.

128 X. Wang, Q. Xu, M. Li, S. Shen, X. Wang, Y. Wang, Z. Feng, J. Shi, H. Han and C. Li, *Angew. Chemie - Int. Ed.*, 2012, **51**, 13089–13092.

129 J. Zhang, Q. Xu, Z. Feng, M. Li and C. Li, *Angew. Chemie - Int. Ed.*, 2008, **47**, 1766–1769.

130 Y.-S. Xu and W.-D. Zhang, *Appl. Catal. B Environ.*, 2013, **140**–**141**, 306–316.

131 S. S. Shinde, C. H. Bhosale and K. Y. Rajpure, *J. Photochem. Photobiol. B Biol.*, 2012, **116**, 66–74.

132 R. Andreozzi, V. Caprio, A. Insola and R. Marotta, *Catal. Today*, 1999, **53**, 51–59.

133 S. Chakrabarti and B. K. Dutta, *J. Hazard. Mater.*, 2004, **B112**, 269–278.

134 S. P. Kim, M. Y. Choi and H. C. Choi, *Mater. Res. Bull.*, 2016, **74**, 85–89.

135 A. Mills and J. Wang, *J. Photochem. Photobiol. A Chem.*, 1999, **127**, 123–134.

136 M. Mishra and D.-M. Chun, *Appl. Catal. A Gen.*, 2015, **498**, 126–141.

137 X. J. Wang, X. N. Xu, Y. J. Han and X. N. Chen, *Cryst. Res. Technol.*, 2015, **50**, 405–412.

138 Z. Zou, J. Ye, K. Sayama and H. Arakawa, *Nature*, 2001, **414**, 625–627.

139 C. A. Walenta, S. L. Kollmannsberger, J. Kiermaier, A. Winbauer, M. Tschurl and U. Heiz, *Phys. Chem. Chem. Phys.*, 2015, **17**, 22809–22814.

140 X. Pan, M.-Q. Yang, X. Fu, N. Zhang and Y.-J. Xu, *Nanoscale*, 2013, **5**, 3601–3614.

141 A. Mclaren, T. Valdes-Solis, G. Li and S. C. Tsang, *J. Am. Chem. Soc.*, 2009, **131**, 12540–12541.

142 H. Liu, H. . Ma, X. . Li, W. . Li, M. Wu and X. . Bao, *Chemosphere*, 2003, **50**, 39–46.

143 A. Kar, S. Sain, S. Kundu, A. Bhattacharyya, S. Kumar Pradhan and A. Patra, *ChemPhysChem*, 2015, **16**, 1017–1025.

144 L. MacHala, J. Tuček and R. Zbořil, *Chem. Mater.*, 2011, **23**, 3255–3272.

145 S. Z. Karazhanov, P. Ravindran, P. Vajeeston, A. Ulyashin, T. G. Finstad and H. Fjellvåg, *Phys. Rev. B*, 2007, **76**, 75129.

146 G. Rothenberger, J. Moser, M. Gratzel, N. Serpone and D. K. Sharma, *J. Am. Chem. Soc.*, 1985, **107**, 8054–8059.

147 N. Dave, B. G. Pautler, S. S. Farvid and P. V. Radovanovic, *Nanotechnology*, 2010, **21**, 134023.

148 E. Stavitski and F. M. F. de Groot, *Micron*, 2010, **41**, 687–694.

149 B. T. Thole, G. van der Laan, J. C. Fuggle, G. A. Sawatzky, R. C. Karnatak and J.-M. Esteva, *Phys. Rev. B*, 1985, **32**, 5107–5118.

150 I. Hamberg and C. G. Granqvist, *J. Appl. Phys.*, 1986, **60**, R123.

151 E. Fortunato, D. Ginley, H. Hosono and D. C. Paine, *MRS Bull.*, 2007, **32**, 242–247.

152 P. D. C. King, T. D. Veal, F. Fuchs, C. Y. Wang, D. J. Payne, A. Bourlange, H. Zhang, G. R. Bell, V. Cimalla, O. Ambacher, R. G. Egdell, F. Bechstedt and C. F. McConville, *Phys. Rev. B*, 2009, **79**, 205211.

153 H. Riesen and W. A. Kaczmarek, *Inorg. Chem.*, 2007, **46**, 7235–7237.

154 X. Wang, Z. Liu, M. A. Stevens-Kalceff and H. Riesen, *Mater. Res. Bull.*, 2013, **48**, 3691–3694.

155 W. Jiang, Z. Bian, C. Hong and C. Huang, *Inorg. Chem.*, 2011, **50**, 6862–6864.

156 S. Zhang, Y. Hu, L. Chen, X. Wang, G. Ju and Z. Wang, *Appl. Phys. A Mater. Sci. Process.*, 2014, **116**, 1985–1992.

157 A. Walsh, *Appl. Phys. Lett.*, 2011, **98**, 261910.

158 F. Claubau, X. Rocquefelte, T. Le Mercier, P. Deniard, S. Jobic and M.-H. Whangbo, *Chem. Mater.*, 2006, **18**, 3212–3220.

159 Y. Yu, D. Chen, Y. Wang, P. Huang, F. Weng and M. Niu, *Phys. Chem. Chem. Phys.*, 2009, **11**, 8774–8778.

160 J. Vela, B. S. Prall, P. Rastogi, D. J. Werder, J. L. Casson, D. J. Williams, V. I. Klimov and J. A. Hollingsworth, *J. Phys. Chem. C*, 2008, **112**, 20246–20250.

161 C. R. Stanek, K. J. McClellan, B. P. Uberuaga, K. E. Sickafus, M. R. Levy and R. W. Grimes, *Phys. Rev. B*, 2007, **75**, 134101.

162 Y. Li, R. Deng, Y. Tian, B. Yao and T. Wu, *Appl. Phys. Lett.*, 2012, **100**, 172402.

163 A. K. Singh, A. Janotti, M. Scheffler and C. G. Van De Walle, *Phys. Rev. Lett.*, 2008, **101**, 55502.

164 B. Fernandes, M. Hegde, P. C. Stanish, Z. L. Mišković and P. V. Radovanovic, *Chem. Phys. Lett.*, 2017, **684**, 135–140.

165 A. Lita, A. L. Washington, L. Van De Burgt, G. F. Strouse and A. E. Stiegman, *Adv. Mater.*, 2010, **22**, 3987–3991.

166 S. M. Berman, *J. Illum. Eng. Soc.*, 1992, **21**, 3–14.

167 A. Layek, P. C. Stanish, V. Chirmanov and P. V. Radovanovic, *Chem. Mater.*, 2015, **27**, 1021–1030.

168 L. M. Peter, *Chem. Rev.*, 1990, **90**, 753–769.

169 S. Yoshioka, H. Hayashi, A. Kuwabara, F. Oba, K. Matsunaga and I. Tanaka, *J. Phys. Condens. Matter*, 2007, **19**, 346211.

170 S. Zheng, Y. Cai and K. E. O'Shea, *J. Photochem. Photobiol. A Chem.*, 2010, **210**, 61–68.

171 C. Yu, W. Zhou, L. Zhu, G. Li, K. Yang and R. Jin, *Appl. Catal. B Environ.*, 2016, **184**, 1–11.

172 T. L. Thompson and J. T. Yates Jr, *Chem. Rev.*, 2006, **106**, 4428–4453.

173 T. Wang and P. V Radovanovic, *Chem. Commun. (Camb).*, 2011, **47**, 7161–7163.

174 T. Wang, a Layek, I. D. Hosein, V. Chirmanov and P. V Radovanovic, *J. Mater. Chem. C*, 2014, **2**, 3212–3222.

175 V. Ghodsi, S. Jin, J. C. Byers, Y. Pan and P. V. Radovanovic, *J. Phys. Chem. C*, 2017, **121**, 9433–9441.

176 S. S. Farvid, T. Sabergharesou, L. N. Hutfluss, M. Hegde, E. Prouzet and P. V. Radovanovic, *J. Am. Chem. Soc.*, 2014, **136**, 7669–7679.

177 M. Kuno, *J. Phys. Chem. Lett.*, 2014, **5**, 3817–3818.

178 B. M. Hunter, H. B. Gray and A. M. Müller, *Chem. Rev.*, 2016, **116**, 14120–14136.

179 Y. H. Jang, Y. J. Jang, S. Kim, L. N. Quan, K. Chung and D. H. Kim, *Chem. Rev.*, 2016, **116**, 14982–15034.

180 X. Meng, L. Liu, S. Ouyang, H. Xu, D. Wang, N. Zhao and J. Ye, *Adv. Mater.*, 2016, **28**, 6781–6803.

Appendix A

The figures presented in Appendix A are supplementary information for Chapter 3.

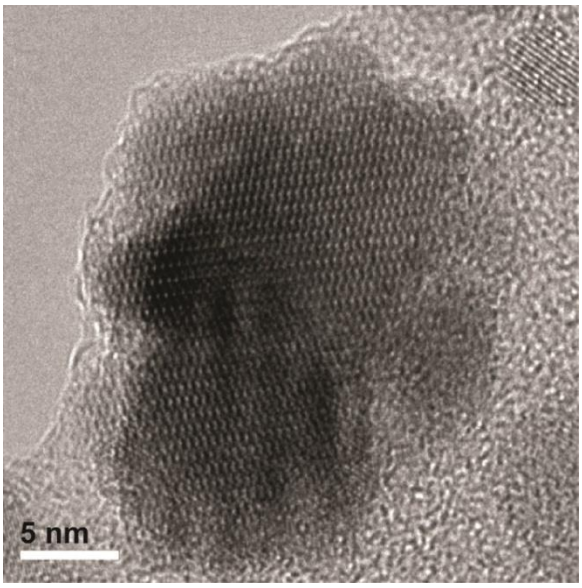

Figure A.1. Lattice-resolved TEM image of a single Eu-doped *bcc*-In_2O_3 nanoflower from the sample prepared at 300 °C with 15 % starting concentration of $EuCl_3$. Continuous lattice fringes indicate that the flower-like nanostructures were formed by the oriented attachment of colloidal NCs.

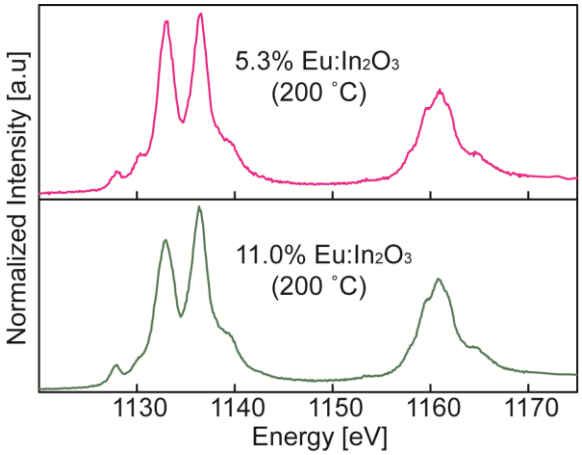

Figure A.2. Eu M-edge X-ray absorption spectra of 5.3 % (top) and 11.5 % (bottom) Eu-doped In_2O_3 NCs synthesized at 200 °C.

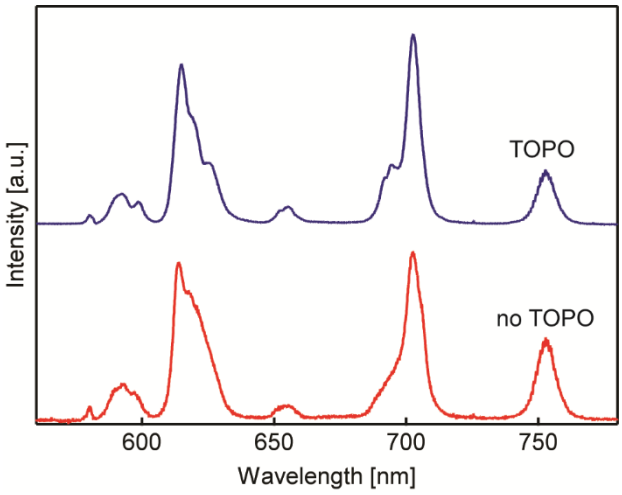

Figure A.3. High-resolution Eu^{3+} PL spectra of Eu-doped *rh*-In_2O_3 NCs synthesized at 200 °C before (bottom) and after (top) treatment with TOPO. Upon TOPO treatment the spectra become better resolved.

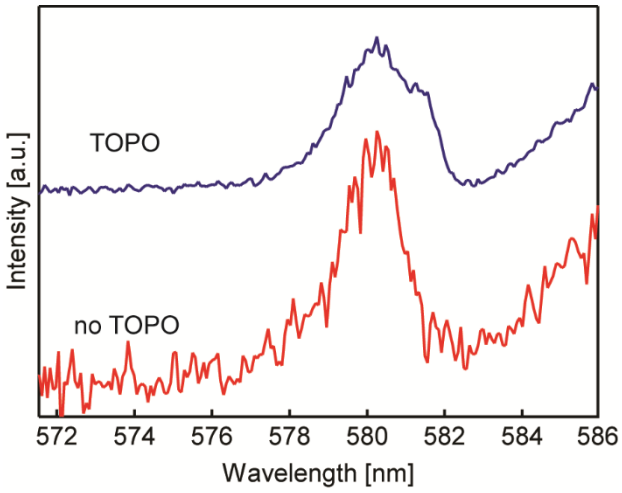

Figure A.4. High-resolution Eu^{3+} ($^5D_0 \rightarrow {}^7F_0$) PL spectra of samples in Figure A.3 before (bottom) and after (top) TOPO treatment. Without TOPO treatment only one broad structureless peak with the maximum at ca. 580.3 nm is observed, indicating a significant presence of Eu^{3+} in the NC surface region. Upon TOPO treatment this peak decreases in intensity revealing a narrow peak at ca. 581.5 nm, which is suggested to be due to internally incorporated Eu^{3+} (see text for more details).

Appendix B

The figures and tables demonstrated in Appendix B, serve as supplementary information for Chapter 4.

Table B.1. Average Size and Crystallite Size of Selected GTO NCs Obtained from HRTEM Images and XRD Patterns, Respectively. The Peak at ca. 35° Was Deconvoluted to Estimate the Crystallite Size.

Sample ID	Ave. Size [nm]	Crystallite size [nm]
10GTO-8h-MeOH	5.7±1.0	5.2
25GTO -8h-MeOH	4.4±1.0	4.0
50GTO -8h-MeOH	4.1±0.6	3.5
75GTO -8h-MeOH	3.5±0.6	3.5
90GTO -8h-MeOH	3.9±0.5	3.5
50GTO-8h-EtOH_1-190 °C [a)]	4.8±1.0	4.6

All syntheses were performed at 190 °C. Samples were named in the following way: the first part indicates the concentration of Ga in GTO NCs-the second part indicates the synthesis duration in hours-the third part specifies the solvent used-the fourth part signifies the synthesis temperature.

[a)] Only 1 mL of ethanol was used in the synthesis of this sample, while keeping the total volume of the solvents (31 mL) and the ratio of oleic acid to oleylamine the same as for other samples (5:1). The amount of both precursors (Ga and Sn) was halved, compared to other samples.

Table B.2. Summary of the Synthetic Conditions and Elemental Analysis Obtained from EDX. Note that the Syntheses Were Done at 190 ºC Unless Otherwise Specified.

Sample ID	Nominal Ga [%]	Actual Ga [%]	Nominal Sn [%]	Actual Sn [%]
10GTO-8h-MeOH	10	10.82 ± 3.7	90	89.18 ± 3.7
25GTO -8h-MeOH	25	23.80 ± 6.3	75	76.02 ± 6.6
50GTO -8h-MeOH	50	41.00 ± 6.3	50	59.00 ± 6.3
75GTO -8h-MeOH	75	61.87 ± 6.9	25	38.13 ± 6.9
90GTO -8h-MeOH	90	85.47 ± 0.01	10	14.56 ± 0.01
50GTO -4h-MeOH	50	39.73 ± 1.9	50	60.27 ± 1.9
50GTO -8h-MeOH	50	41.00 ± 6.3	50	59.00 ± 6.3
50GTO -32h-MeOH	50	44.35 ± 6.2	50	55.65 ± 6.2
50GTO -8h-EtOH-140 ºC	50	43.19 ± 6.3	50	56.81 ± 6.3
50GTO -8h-EtOH-190 ºC	50	33.74 ± 1.8	50	66.26 ± 1.8
50GTO -8h-EtOH-220 ºC	50	28.86 ± 6.3	50	71.14 ± 6.3
50GTO-8h-EtOH_1-190 ºC [a)]	50	34.15 ± 8.9	50	65.85 ± 8.9

Table B.3. PL Lifetime Parameters Obtained from Biexponential Fitting of the PL Time Decay Data for GTO NCs Prepared under Designated Conditions.

Samples ID	A_1 [%]	τ_1 [μs]	A_2 [%]	τ_2 [μs]	<τ> [μs]
10GTO-8h-MeOH	69.4±1.0	0.64±0.03	30.6±0.4	2.66±0.06	1.26±0.06
25GTO -8h-MeOH	59.7±1.0	0.76±0.001	40.3±0.5	2.43±0.06	1.43±0.03
50GTO -8h-MeOH	63.9±0.7	0.76±0.001	36.1±0.3	2.01±0.02	1.21±0.01
75GTO -8h-MeOH	70.2±0.7	0.69±0.02	29.8±0.3	1.78±0.02	1.01±0.02
90GTO -8h-MeOH	61.4±0.8	0.53±0.02	38.6±0.3	1.75±0.02	1.00±0.02
100GTO -8h-MeOH	75.2±2.0	0.15±0.01	24.8±0.3	1.14±0.03	0.40±0.03
50GTO -4h-MeOH	57.7±0.8	0.59±0.03	42.3±0.4	1.38±0.02	0.92±0.03
50GTO -8h-MeOH	63.9±0.7	0.76±0.001	36.1±0.3	2.01±0.02	1.21±0.01
50GTO -16h-MeOH	59.6±0.7	0.79±0.001	40.4±0.3	2.00±0.02	1.28±0.01
50GTO -32h-MeOH	65.4±0.6	0.94±0.03	34.6±0.3	2.52±0.03	1.49±0.03
50GTO -8h-EtOH-140 ºC	49.8±1.0	0.50±0.04	50.2±0.5	1.20±0.02	0.86±0.05
50GTO -8h-EtOH-160 ºC	71.4±0.6	0.93±0.03	28.6±0.2	2.35±0.03	1.34±0.03
50GTO -8h-EtOH-190 ºC	63.0±0.7	0.98±0.05	37.0±0.3	2.68±0.03	1.61±0.04
50GTO -8h-EtOH-220 ºC	56.9±1.0	0.75±0.05	43.1±0.4	2.90±0.04	1.68±0.09

Table B.4. Scotopic to Photopic Ratio and PLQY of the Samples Prepared under Different Conditions.

Sample ID	Nominal Ga	Nominal Sn	Reaction Length	Alcohol-Volume	S/P	PLQY [%]
Sample 1	20%	80%	10 h	MeOH- 7 mL	2.58	15.7 ± 0.6
Sample 2	25%	75%	16 h	MeOH- 7 mL	2.54	14.7 ± 0.5
Sample 3	25%	75%	32 h	MeOH- 7 mL	2.57	18.1 ± 0.7
Sample 4	30%	70%	30 h	EtOH- 7 mL	2.47	19.1 ± 0.7
Sample 5	50%	50%	8 h	EtOH- 1 mL	2.63	29.5 ± 1.1
Sample 6[a)]	50%	50%	12 h	EtOH- 1 mL	2.60	33.3 ± 1.2

[a)] Only 1 mL of ethanol was used in the synthesis of this sample, while keeping the total volume of the solvents (31 mL) and the ratio of oleic acid to oleylamine the same as for other samples (5:1). The amount of both precursors (Ga and Sn) was halved, compared to other samples.

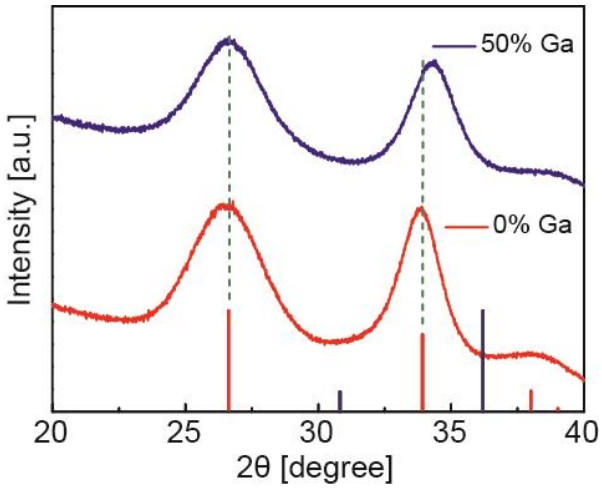

Figure B.1. XRD patterns of GTO NCs with different Ga content (atom %), as indicated in the graph. Red and blue sticks represent the patterns of bulk rutile SnO_2 and γ-Ga_2O_3, respectively.

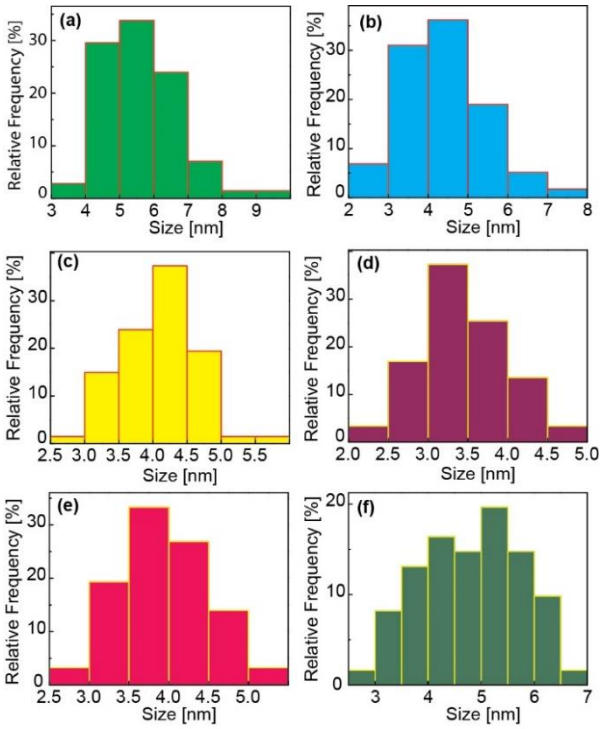

Figure B.2. Size distribution histograms of selected GTO NCs synthesized with different ratio of gallium and tin precursor concentrations: (a) 10 % Ga, (b) 25 % Ga, (c) 50 % Ga, (d) 75 % Ga, (e) 90 % Ga, and (f) 50 % Ga. The synthetic conditions are provided in the caption of Table B.1.

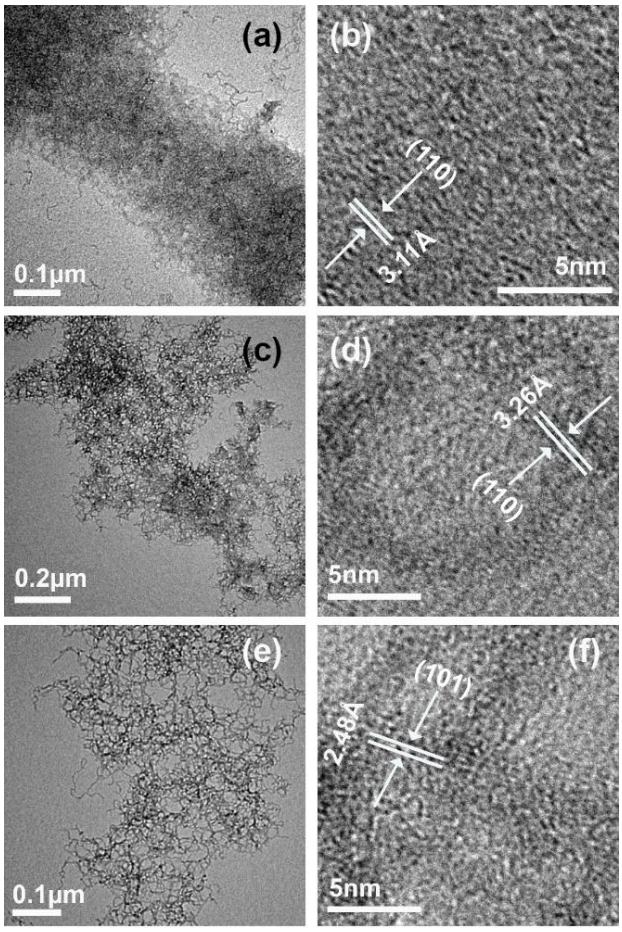

Figure B.3. TEM images of GTO NCs with 50% Ga contents with varying the reaction duration. (a and b) 4h, (c and d) 8h, and (e and f) 32h. Elemental mapping of the 32h sample is shown in Figure 4.2 (e-g).

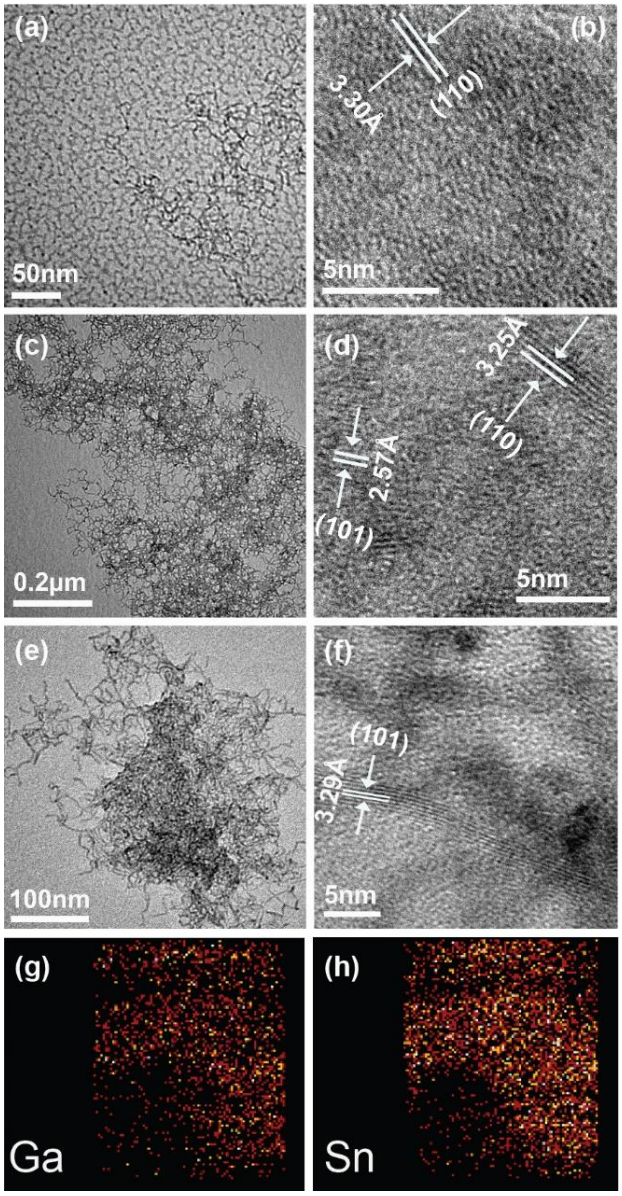

Figure B.4. TEM images of GTO NCs with 50% Ga contents with varying the reaction temperature. (a and b) 140 ºC, (c and d) 190 ºC, and (e and f) 220 ºC. (g and h) Elemental mapping of the sample synthesized at 190 ºC.

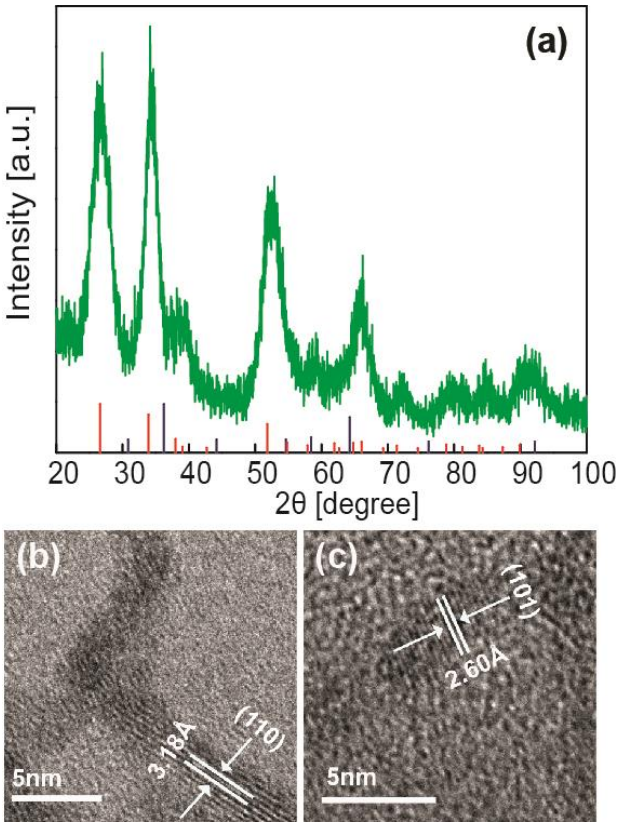

Figure B.5. The structural characterization of GTO NCs with ideal S/P ratio and PLQY of 34%. (a) XRD pattern confirming its tin oxide- based structure, (b and c) HRTEM images of the sample in (a).

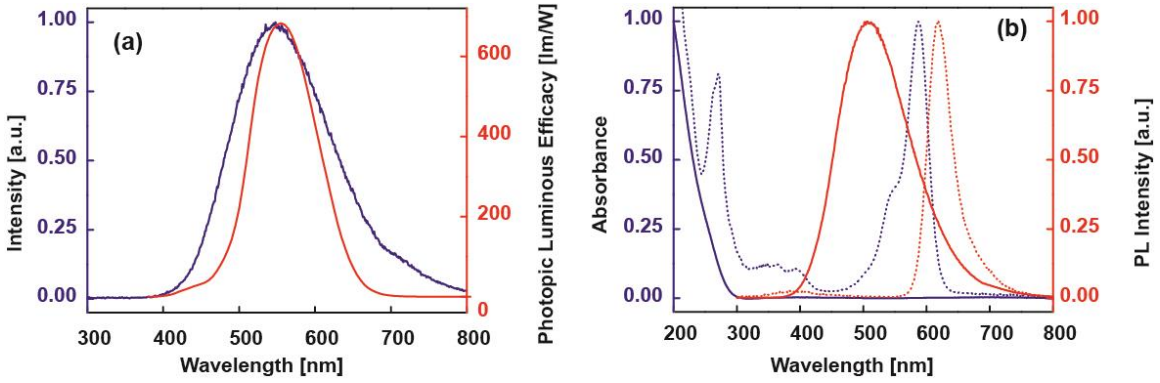

Figure B.6. (a) PL of GTO NCs (containing 10% Ga and synthesized for 10h) covering the photopic vision. (b) PL and absorbance of GTO NCs in Figure 4.7a and Atto-590. The absorbance and PL of Atto-590 are illustrated with dotted lines.

Appendix C

The table and figures illustrated in Appendix C act as supplementary information for Chapter 5.

Table C.1. Rate of Photocatalytic Degradation of Rh-590 and Apparent Quantum Efficiency (AQE) for Photocatalysts Prepared by Annealing γ-Ga_2O_3 Nanocrystals at Different Temperatures.

Annealing T (°C)	d[X]/d*t* [mol/sL]	AQE [%]
400 ºC	$(5.6\pm0.1)\cdot10^{-9}$	0.142±0.001
600 ºC	$(4.9\pm0.1)\cdot10^{-9}$	0.124±0.001
650 ºC	$(6.3\pm0.3)\cdot10^{-9}$	0.160±0.020
800 ºC	$(1.9\pm0.3)\cdot10^{-9}$	0.049±0.010

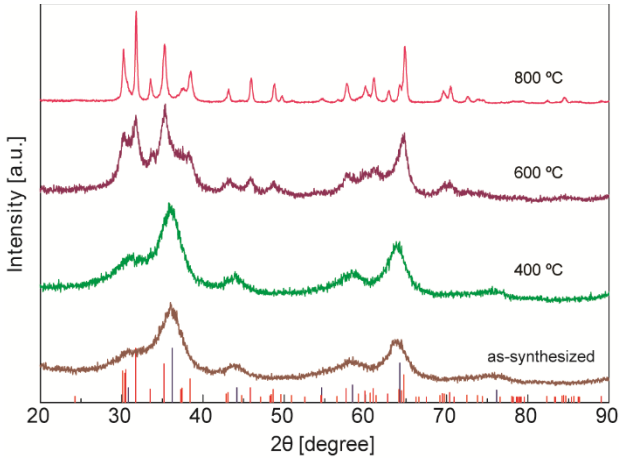

Figure C.1. XRD patterns of Ga_2O_3 NCs synthesized at 300 ºC and annealed at different temperatures as indicated in the graph. Blue and red sticks represent the patterns of bulk γ-Ga_2O_3 and β-Ga_2O_3, respectively.

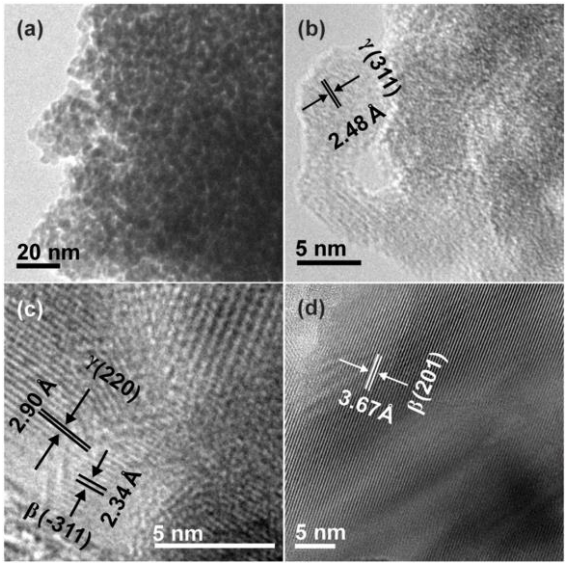

Figure C.2. TEM images of Ga_2O_3 NCs synthesized at 300 ºC and annealed at (a, b) 400 ºC, (c) 600 ºC, and (d) 800 ºC.

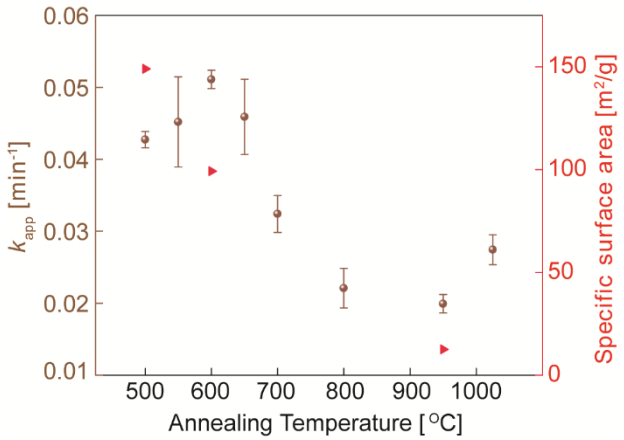

Figure C.3. Ga_2O_3 NC annealing temperature dependence of the apparent rate constant of Rh-590 degradation (brown spheres) and the specific surface area of the photocatalyst (red triangles) for the NCs synthesized at 300 ºC. The measurements were performed in the annealing temperature range corresponding to the mixed γ-Ga_2O_3 and β-Ga_2O_3 phases.

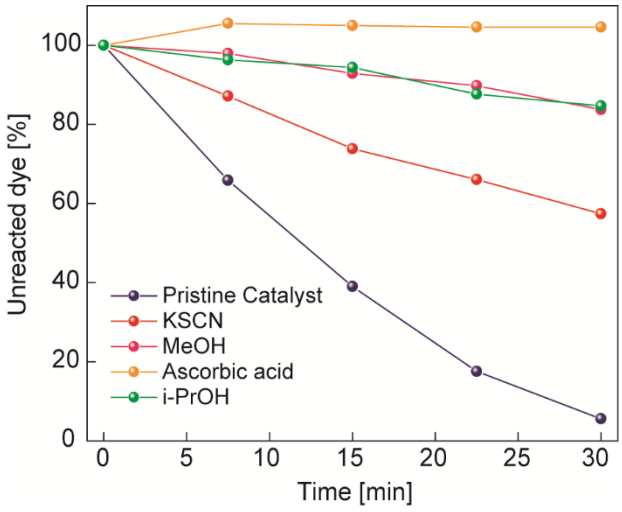

Figure C.4. Photocatalytic degradation of Rh-590 by γ-Ga_2O_3 in the presence of different scavengers. The photocatalyst was prepared by annealing Ga_2O_3 NCs at 400 ºC.

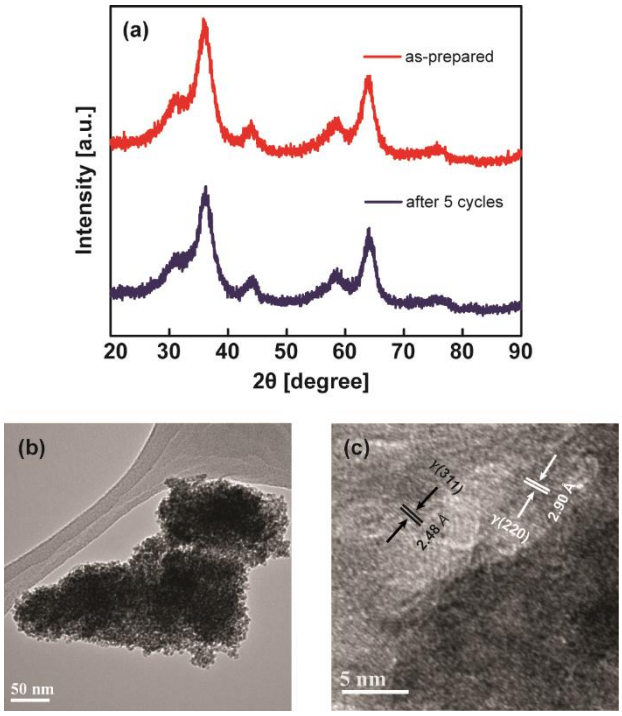

Figure C.5. (a) XRD patterns of γ-Ga_2O_3 photocatalyst as-prepared (upon annealing at 400 °C) and after 5 photocatalytic cycles. (b) Overview TEM image of γ-Ga_2O_3 photocatalyst after 5 cycles. (c) High-resolution TEM image of the sample in (b). The XRD and TEM data indicate no change in the structure and morphology of the photocatalyst after multiple photocatalytic cycles.

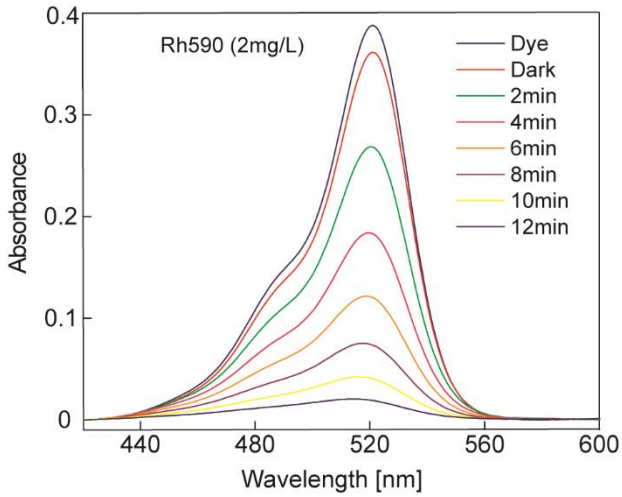

Figure C.6. Absorption spectra of Rh-590 solution (2 mg/L) monitored over time in the presence of γ-Ga_2O_3 photocatalyst under UV excitation. The photocatalyst was prepared by annealing as-synthesized NCs at 400 ºC.

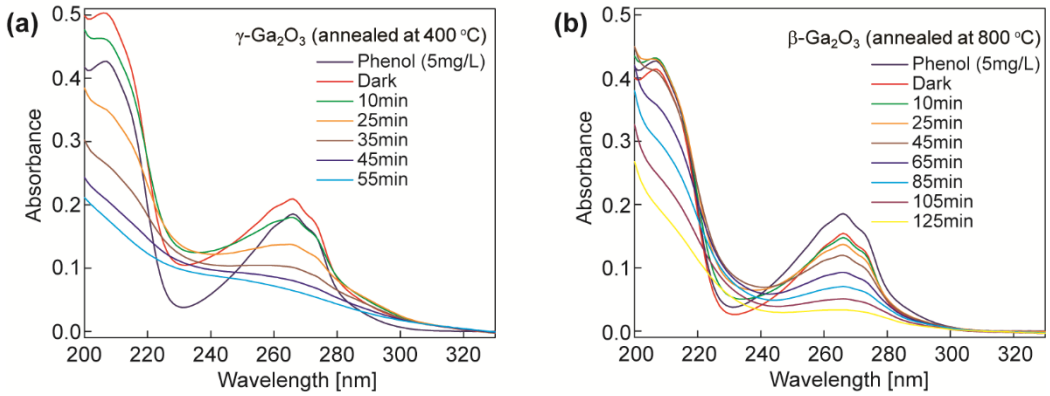

Figure C.7. Absorption spectra of phenol solutions (5 mg/L) monitored over time in the presence of Ga_2O_3 nanocrystalline photocatalysts under UV excitation: (a) γ-Ga_2O_3 prepared by annealing as-synthesized NCs at 400 ºC, and (b) β-Ga_2O_3 prepared by annealing as-synthesized NCs at 800 ºC. Exposure times corresponding to different spectra are indicated in the graphs. The degradation of phenol is significantly faster in (a), confirming anomalous photocatalytic activity of γ-phase Ga_2O_3.

Appendix D

The figures and tables exhibited in Appendix D, are designated as the supplementary information for Chapter 6.

Table D.1. Summary of Elemental Analysis Obtained from EDX.

Sample ID	Nominal Ga	Actual Ga	Nominal Sn	Actual Sn
10GTO	10 %	8.36 %	90 %	91.64 %
25GTO	25 %	19.55±2.5 %	75 %	80.45±2.5 %
50GTO	50 %	38.86 %	50 %	61.14 %
75GTO	75 %	53.72 %	25 %	46.28 %
90GTO	90 %	78.12 %	10 %	21.88 %
25GTO- after 5 cycles	25 %	18.05±0.94 %	75 %	81.95±0.94 %

Table D.2. PL Lifetime Parameters Obtained from Biexponential Fitting of the PL Time Decay Data for GTO NCs in Microsecond Range.

Sample ID	A_1 [%]	τ_1 [µs]	A_2 [%]	τ_2 [µs]	$<\tau>$ [µs]
0GTO	70.3±0.8	0.16±0.005	29.7±0.2	0.69±0.009	0.32±0.01
5GTO	66.9±0.4	0.32±0.006	33.1±0.1	1.33±0.008	0.66±0.001
10GTO	56.7±0.5	0.32±0.009	43.3±0.2	1.45±0.009	0.81±0.01
25GTO	54.8±0.6	0.36±0.01	45.2±0.2	1.53±0.01	0.89±0.01
50GTO	54.0±0.6	0.37±0.01	46.0±0.2	1.43±0.01	0.85±0.01
75GTO	56.6±0.5	0.36±0.01	43.4±0.2	1.39±0.009	0.81±0.01
90GTO	58.2±0.7	0.25±0.01	41.8±0.2	1.10±0.01	0.61±0.01
95GTO	61.9±0.7	0.20±0.007	38.1±0.2	1.08±0.01	0.53±0.01

Table D.3. PL Lifetime Parameters Obtained from Biexponential Fitting of the PL Time Decay Data for GTO NCs in Nanosecond Time Domain.

Sample ID	A_1 [%]	τ_1 [ns]	A_2 [%]	τ_2 [ns]	$\langle\tau\rangle$ [ns]
0GTO	88.5±1.1	2.99±0.09	11.5±0.2	42.47±1.6	7.5±0.3
5GTO	75.7±0.6	5.17±0.1	24.3±0.2	35.65±1.0	12.6±0.2
10GTO	68.5±0.6	5.98±0.2	31.5±0.2	35.24±0.6	15.2±0.2
25GTO	69.1±0.6	6.35±0.2	30.9±0.2	35.00±0.6	15.2±0.3
50GTO	76.5±0.7	5.50±0.2	23.5±0.2	33.08±0.7	12.0±0.2
75GTO	82.2±0.7	5.40±0.09	17.8±0.2	38.72±1.4	11.3±0.3
90GTO	84.3±0.7	4.99±0.08	15.7±0.1	36.06±1.5	9.9±0.2
95GTO	81.7±0.7	4.50±0.08	18.3±0.1	32.55±0.9	9.6±0.2

Table D.4. Specific Surface Area (S_{BET}), Apparent Rate Constant and PL Lifetime for GTO NCs with Different Ga Contents.

Nominal Ga	S_{BET} [m^2/g]	$k_{app.}$ [min^{-1}]	$\langle\tau\rangle$ [ns]
0% Ga	75.0	0.10±0.01	7.5±0.3
5% Ga	83.8	0.20±0.03	12.6±0.2
10% Ga	172.4	0.31±0.02	15.2±0.2
25% Ga	211.7	0.35±0.01	15.2±0.3
50% Ga	303.8	0.19±0.01	12.0±0.2
90% Ga	335.5	0.10±0.01	9.9±0.2

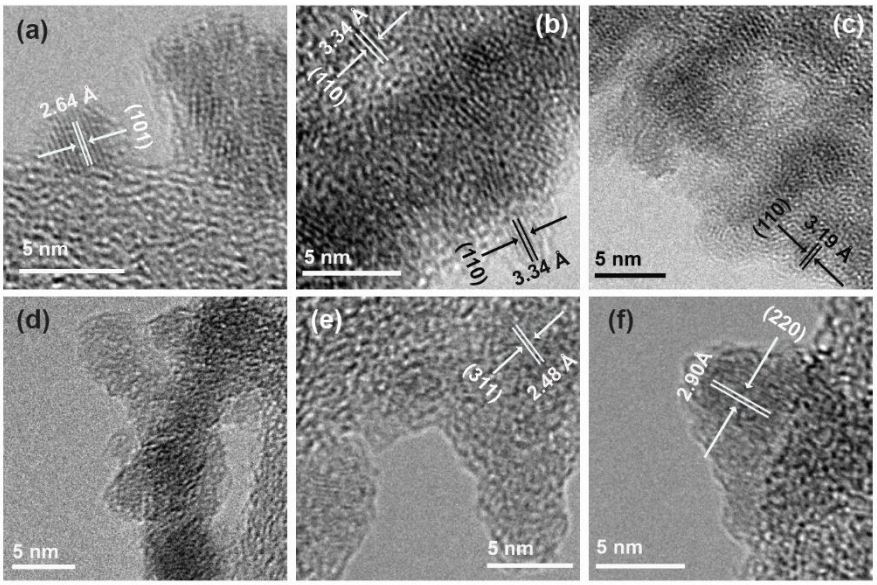

Figure D.1. TEM images of GTO NCs with different starting concentrations of Ga. (a) 5% Ga, (b) 10%, (c) 50%, Ga, (d) 75% Ga, (e) 90% Ga, and (f) 100% Ga. The measured lattice fringes correspond to rutile SnO_2 and γ-Ga_2O_3 in (a-c) and (e-f), respectively. Despite of showing some degree of crystallinity in XRD and HRTEM, the lattice fringes of GTO NCs containing 50% Ga in (d), could not be measured with high degree of certainty.

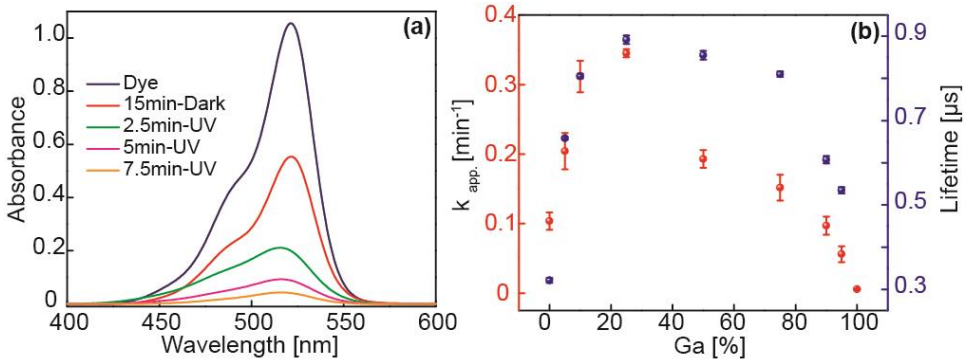

Figure D.2. (a) Absorption spectra of Rh-590 collected against time in the presence of GTO photocatalyst containing 25% Ga exposed to UV light. Dark blue trace is the absorption spectrum of Rh-590 solution in the absence of the catalyst, and red trace is the absorption spectrum of Rh-590 sonicated in the dark for 15 min in the presence of the catalyst. (b) Apparent rate constant and lifetime of GTO NCs as a function of Ga starting concentration.

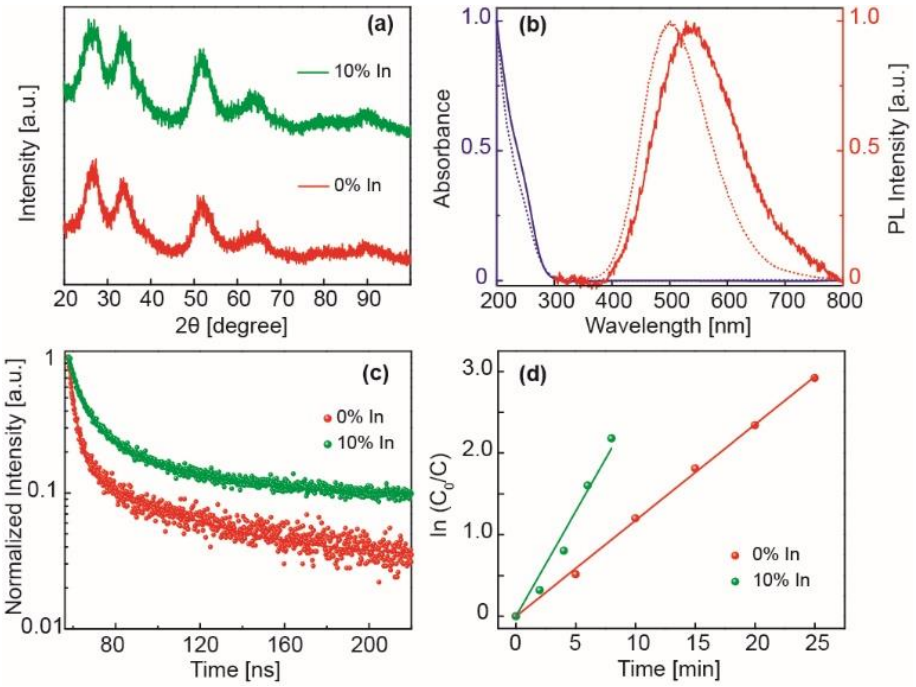

Figure D.3. Comparison between structural properties, spectroscopic properties and photocatalytic performance of pure SnO_2 and 10 % In-doped SnO_2. (a) XRD patterns, (b) PL and absorption spectra. The PL and absorption spectra of 10 % In-doped SnO_2 are illustrated with dotted lines. (c) Time - resolved PL decay. (d) Langmuir-Hinshelwood plot for photodegradation of Rh-590. Straight lines are linear fits to the experimental data using Eq. 6.2.

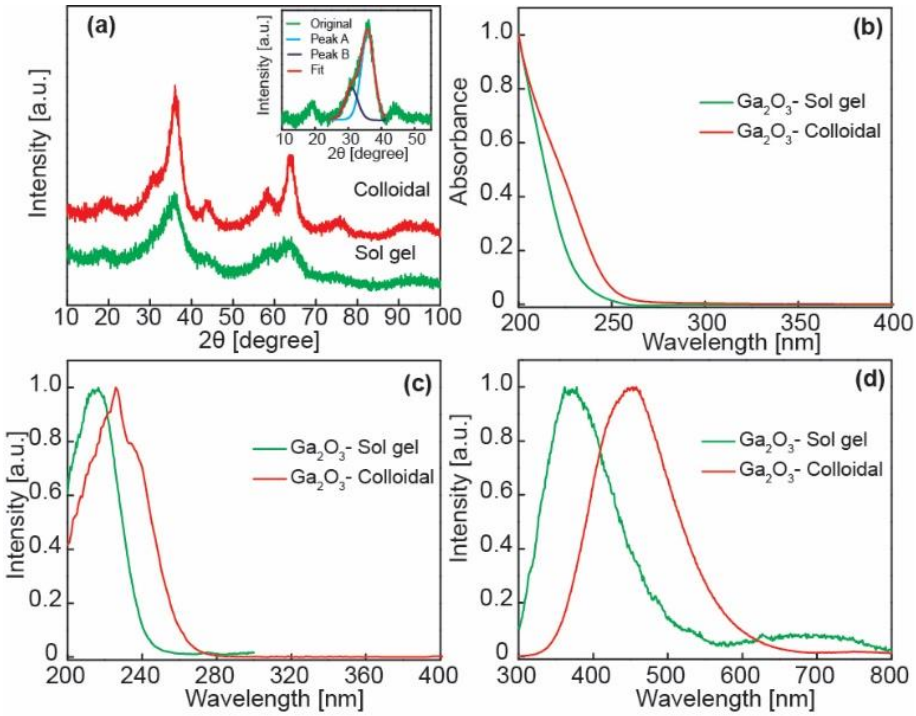

Figure D.4. Comparison between structural and spectroscopic properties of γ-Ga_2O_3 prepared by colloidal synthesis and sol gel method. (a) XRD patterns, (b) absorption spectra, (c) excitation spectra, (d) photoluminescence spectra. XRD peaks of γ-Ga_2O_3 NCs synthesized by sol gel method were deconvoluted to estimate the size of the particles by Scherrer equation and illustrated in the inset of panel (d).

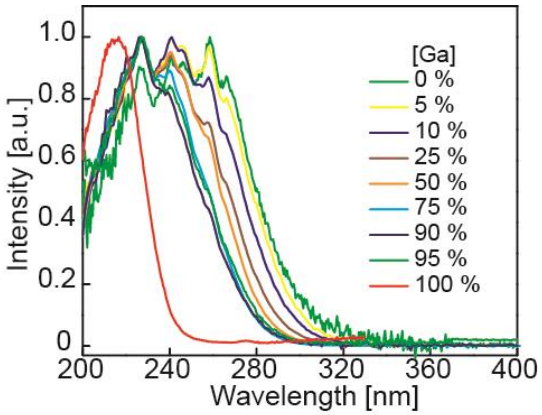

Figure D.5. Excitation spectra of GTO NCs. Incorporation Sn^{4+} of in γ-Ga_2O_3 creates defect states whose energy are deeper in the band gap, compared to native defects.

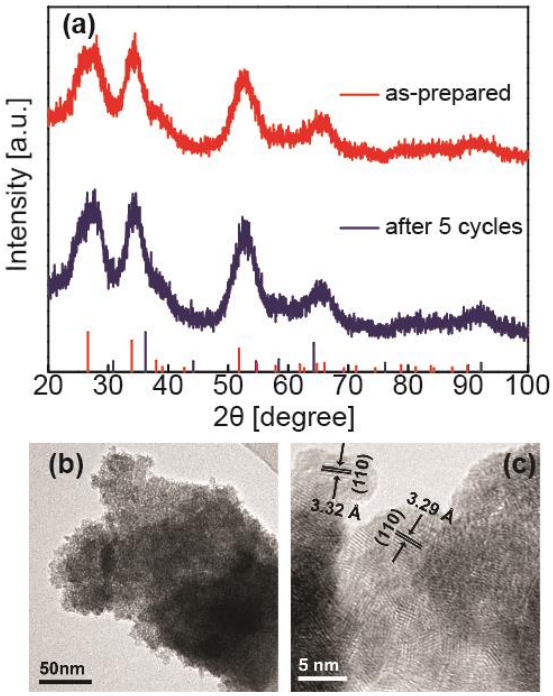

Figure D.6. (a) Comparison between XRD patterns of as-prepared GTO NCs containing 25% Ga with the same NCs after 5 cycles. (b) Overview TEM image of GTO NCs containing 25% Ga after 5 cycles. (c) High resolution TEM images of the NPs in (c). No structural and morphological change was observed after running 5 recycling tests.

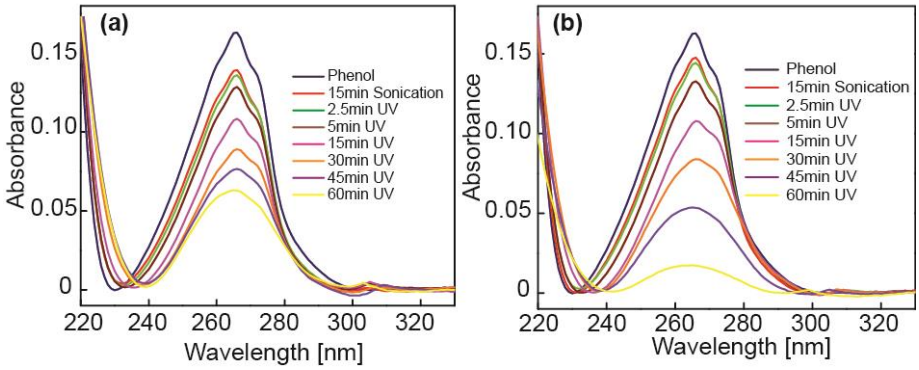

Figure D.7. Monitoring the absorption spectra of phenol solutions (5 mg/L) under different time exposure to UV light in the presence of photocatalysts: (a) SnO_2, and (b) GTO NCs containing 10% Ga. GTO NCs shows faster degradation rate under the same length of time, compared to undoped SnO_2.